12-2016

Carbon nanotube thermal interfaces and related applications

Stephen L. Hodson
Purdue Univesity

PURDUE UNIVERSITY
GRADUATE SCHOOL
Thesis/Dissertation Acceptance

This is to certify that the thesis/dissertation prepared

By Stephen Lallana Hodson

Entitled

CARBON NANOTUBE THERMAL INTERFACES AND RELATED APPLICATIONS

For the degree of Doctor of Philosophy

Is approved by the final examining committee:

Timothy S. Fisher
Chair

David F. Bahr

Xianfan Xu

Baratunde A. Cola

To the best of my knowledge and as understood by the student in the Thesis/Dissertation Agreement, Publication Delay, and Certification Disclaimer (Graduate School Form 32), this thesis/dissertation adheres to the provisions of Purdue University's "Policy of Integrity in Research" and the use of copyright material.

Approved by Major Professor(s): Timothy S. Fisher

Approved by: Jay P. Gore 11/21/2016

Head of the Departmental Graduate Program Date

CARBON NANOTUBE THERMAL INTERFACES AND RELATED APPLICATIONS

A Dissertation

Submitted to the Faculty

of

Purdue University

by

Stephen L. Hodson

In Partial Fulfillment of the

Requirements for the Degree

of

Doctor of Philosophy

December 2016

Purdue University

West Lafayette, Indiana

To my family and friends for their love and support

ACKNOWLEDGEMENTS

First and foremost, I thank everyone who I have had the pleasure to meet throughout my graduate career. The friendships that were personally and professionally formed were wholeheartedly valuable and will carry me through the rest of life. I thank my committee members for their distinguishing support of my graduate work and aspirations. My longtime advisor and friend, Dr. Timothy S. Fisher for his unwavering encouragement and support of my professional and personal aspirations. Dr. Baratunde A. Cola for his personal and technical words of inspiration and wisdom. Dr. Xianfan Xu for his technical support on the Raytheon nTIM project as well as his candid and kind nature. Dr. David F. Bahr for providing me with an alternative perspective of CNT turfs and allowing me to use his nanoindentation equipment. I also thank Dr. Amy Marconnet for allowing me to use her infrared microthermography equipment and Dr. Matthew R. Maschmann for performing nanoindentation experiments on my samples.

I thank current group members, Ishan Srivistava and Sridhar Sadivisvam, for their technical expertise, candidness, and humorous conversations that we have shared together. I thank the current and former staff members of the Birck Nanotechnology Center (Dave Lubelski, Kenny Schwartz, John Coy, Steve Jurss, Dan Hosler, Tim Miller, Aamer

Mahmood, Geoff Gardner, and Nancy Black) for their unwavering support, invaluable expertise, and enriching daily interactions.

Lastly, I thank my longtime colleague, former group member, and lifelong friend, Robert A. Sayer, for presenting me with the opportunity to return to the Land of Enchantment and conduct research at Sandia National Laboratories in Albuquerque, NM. Throughout my time at Sandia National Laboratories, I have had the pleasure of working with Thomas Grasser and Paul Farias, both of whom have supported my work with extreme quality, and Tracie Durbin, my manager, who has supported my career aspirations. Sandia National Laboratories is a multi-program laboratory managed and operated by Sandia Corporation, a wholly owned subsidiary of Lockheed Martin Corporation, for the U.S. Department of Energy's National Nuclear Security Administration under Contract DE-AC04-94AL85000.

TABLE OF CONTENTS

Page

Page

Page

LIST OF TABLES

LIST OF FIGURES

Figure Page

Figure Page

Figure Page

Figure Page

ABSTRACT

Stephen Lallana Hodson, PhD, Purdue University, December 2016. Carbon Nanotube Thermal Interfaces and Related Applications. Major Professor: Timothy S. Fisher, School of Mechanical Engineering.

The development of thermal interface materials (TIMs) is necessitated by the temperature drop across interfacing materials arising from macro and microscopic irregularities of their surfaces that constricts heat through small contact regions as well as mismatches in their thermal properties. Similar to other types of TIMs, CNT TIMs alleviate the thermal resistance across the interface by thermally bridging two materials together with cylindrical, high-aspect ratio, and nominally vertical conducting elements. Within the community of TIM engineers, the vision driving the development of CNT TIMs was born from measurements that revealed impressively high thermal conductivities of individual CNTs. This vision was then projected to efforts focused on packing many individual CNTs on a single substrate that efficiently conduct heat in parallel and ultimately through many contact regions at CNT-to-substrate contacts.

This thesis encompasses a comprehensive investigation of the viability of carbon nanotube based thermal interface materials (CNT TIMs) to efficiently conduct heat across two contacting materials. The efforts in this work were initially devoted to engaging CNT TIMs with an opposing substrate using two bonding techniques. Using palladium hexadecanethiolate, $Pd(SC_{16}H_{35})_2$ the CNT ends were bonded to an opposing substrate (one-sided interface) or opposing CNT array (two-sided interface) to enhance

contact conductance while maintaining a compliant joint. The palladium weld is particularly attractive for its mechanical stability at high temperatures. The engagement of CNT TIMs with an opposing substrate was also achieved by inserting a solder foil between the CNT TIM and opposing substrate and subsequently raising the temperature of the interface above the eutectic point of the solder foil. This bonding technique creates a strong weld that not only reduces the thermal resistance significantly but also minimizes the change in thermal resistance with an applied compressive load. The thermal performance was further improved by infiltrating the CNT TIM with paraffin wax, which serves as an alternate pathway for heat conduction across the interface that ultimately reduces the bulk thermal resistance of the CNT TIM.

For CNT TIMs synthesized at the Birck Nanotechnology Center at Purdue University, the thermal resistance was shown to scale linearly with their aggregate, as-grown height. Thus, the bulk thermal resistance can alternatively be tuned by adjusting the as-grown height. The linear relationship between thermal resistance and CNT TIM height provides a simple and efficient methodology to estimate the contact resistance and effective thermal conductivity of CNT TIMs. In this work, the contact resistance and effective thermal conductivity were estimated using two measurement techniques: (i) one-dimensional, steady-state reference bar and (ii) photoacoustic technique. A discrepancy in the estimated contact resistance exists between the two measurement techniques, which is due to the difficulty in measuring the true contact area. In contrast, the effective thermal conductivities estimated from both measurement techniques moderately agreed and were estimated to be on the order of O(1 W/mK).

In Chapter 7, the thermomechanical behavior of CNT TIMs was investigated to assess their thermal performance under compression. Companion CNT TIMs were compressed by a flat-punch nanoindenter to assess mechanical properties. Photoacoustic measurements of CNT TIMs with as-grown heights ranging from 3 to 50 μm indicated that shorter CNTs exhibit lower thermal resistance than their taller counterparts. In addition to the contact resistance, the effective thermal conductivity was found to depend on compressive stress. Clear buckling shoulders are observed in the nanoindentation measurements within the compressive stress ranges corresponding to changes in thermal resistance, indicating that the thermal performance is coupled to the mechanical response. We postulate that the observed change in effective thermal conductivity of the CNT TIM with compressive stress counteracts the change in contact area of the CNT TIM with the opposing substrate. Additionally, the roles of defects and CNT-to-CNT contacts were qualitatively considered in an underlying microstructural framework that dictates the thermomechanical behavior of CNT TIMs.

In collaboration with Sandia National Laboratories, this thesis also includes auxiliary chapters that investigate the thermal performance of CNT TIMs in abnormal environments such as those in space applications in which components are subjected to gamma-ray irradiation as well those in thermoelectric generators that operate at elevated temperatures. The former investigation included subjecting CNT TIMs to gamma irradiation doses of 50 and 100 Mrad. The latter investigation included mechanical and thermal cycling of the CNT TIMs at interface temperatures up to 450°C. For each application, the thermal performance of CNT TIMs was determined to be stable in the abnormal environments

The final chapter is in collaboration with Sandia National Laboratories and focuses on the development of an apparatus to measure the thermal conductivity of insulation materials critical for the operation of molten salt batteries. Molten salt batteries are particularly useful power sources for radar and guidance systems in military applications such as guided missiles, ordinance, and other weapons. Molten salt batteries are activated by raising the temperature of the electrolyte above its melting temperature using pyrotechnic heat pellets. The battery will remain active as long as the electrolyte is molten. As a result, the thermal processes within the components and interactions between them are critical to the overall performance of molten salt batteries. A molten salt battery is typically thermally insulated using wrappable and board-like insulation materials such as Fiberfrax wrap, Fiberfrax board, and Min-K insulation. The Fiberfrax board and Min-K insulation are composites of alumino-silicate and fumed silica-titania, respectively. In Chapter 9, the thermal conductivities of the Fiberfrax board and Min-K insulation were measured under different uniaxial compressive states and ambient environments. The thermal conductivity of the mixed separator pellets (LiCl/MgO/KCl) was also measured along with its contact resistances with interfacing members. To measure the thermal quantities, a steady-state reference bar with thermocouples was employed. The resulting values serve as inputs to a thermal model that aims to predict lifetimes of the batteries.

1. INTRODUCTION

1.1 Motivation

Thermal contact conductance or thermal contact resistance between contacting members has been formally studied over the past century. The first publications on thermal contact conductance were on polished stainless steel surfaces at cryogenic temperatures in the 1930s. When the world was spun into turmoil during the second World War, studies on thermal contact conductance transitioned to military applications such as aircraft and missiles, which focused on thermal transport between metallic components. In the advent of the nuclear age, thermal engineers became interested in the effects of high temperature, high contact pressure, and high gas temperature on thermal contact resistance for the design of nuclear reactors. As the space race with the former Soviet Union became a mission statement for the nation, interstitial metals such as indium, lead, and tin were studied as thermal interface materials (TIMs) for the modular components in spacecraft and satellites in vacuum.

Presently, thermal contact resistance continues to play a significant role in the development small-scale devices for a diverse group of applications in which heat is generated from an electronic device. As the size of electronic devices scales down and power densities increase, the demand for innovative cooling solutions becomes more imperative. The prototypical architecture for electronic devices generally consists of a

heat generating component such as a microprocessor and a heat spreader in tandem with a heat sink that transfers the heat to the ambient environment. Due to the modular assembly of the device architecture, thermal resistances at the interfaces of the components can significantly contribute to the total thermal budget. This thermal resistance, or thermal interface resistance is a consequence of the constriction of heat flow through small contact regions between adjoining components. When a TIM is inserted between the components, this thermal resistance is comprised of the thermal contact resistance at the adjoining interfaces as well as the bulk resistance of the TIM.

1.2 Contributions and Organization of Thesis

Chapter 2 contains a comprehensive literature review of thermal interface materials, carbon nanotube synthesis, carbon nanotube thermal interface materials (CNT TIMs), and mechanical deformation of carbon nanotubes.

Chapter 3 provides an overview of the various techniques used to assess the thermal performance of CNT TIMs (photoacoustic and one-dimensional steady-state reference bar). A comparison between the two measurement techniques is included. This chapter also includes an overview of the palladium thiolate and solder bonding techniques employed in this work.

Chapter 4 presents an innovative bonding technique that involves the use of a metal-organic precursor as the bonding agent. The metal-organic precursor is palladium (Pd) thiolate that was previously developed by T. Bhuvana in her work with Dr. G. U. Kulkarni. After thermolysis, a strong Pd weld is created at the CNT/Ag foil interface that shows

promising thermal performance and possibly indicates a transition from a traditional van der Waals type bond for unbonded interfaces to a more covalent-like bond. Overall, this bonding technique provides a promising method to improve the thermal performance of CNT TIMs at temperatures up to 250°C. The work on this topic was published in the *Proceedings of the ASME InterPACK Conference* in 2009 and later in the *Journal of Electronic Packaging* in June 2011.

Chapter 5 assesses the performance of CNT TIMs for space applications in collaboration with Sandia National Laboratories. The CNT TIMs were irradiated with different doses of gamma rays. Raman spectroscopy and PA measurements were conducted before and after irradiation. This work was initially published in the *Proceedings of the ASME International Mechanical Engineering Congress & Exposition* in 2013 and a more comprehensive overview was published in the *International Journal of Micro-Nano Scale Transport* in 2014.

Chapter 6 focuses on two-sided CNT TIMs grown on Cu foil that were measured using the 1D steady state reference bar technique at Raytheon. This chapter is in conjunction with the Nano Thermal Interface Materials (nTIM) project in collaboration with Raytheon and Georgia Tech. These samples were first solder-bonded and subsequently infiltrated with paraffin wax and discussion is provided regarding the mechanisms for improved thermal performance (effective thermal conductivity and contact resistance). The vital role of wettability of solder and paraffin wax to the CNTs is considered to be paramount to improving thermal performance. The work related to CNT arrays enhanced with paraffin wax was published in *Proceedings of ASME Summer Heat Transfer Conference in 2008*. The work in collaboration with Raytheon on solder bonded TIMs was published in the

Proceedings of the ASME 2011 Pacific Rim Technical Conference and Exhibition on Packaging and Integration of Electronic and Photonic Systems, MEMS and NEMS and won best paper award at the InterPACK 2011 conference. A manuscript related to this project focuses on quantifying the effective thermal conductivity and contact resistances.

Chapter 7 focuses on the thermomechanical performance of CNT TIMs within a pressure range of 20 and 145 kPa. The thermal performance was evaluated using the PA technique while nanoindentation tests, courtesy of Dr. Matthew R. Maschmann at the University of Missouri, served as a supplement to the PA measurements to assess the mechanical performance. The contributions of the bulk and contact resistances are extracted from the PA measurements and the results suggest that CNT TIMs are limited not only by the amount of contact they make with opposing substrates but also by the aggregate changes in their microstructure in response to uniaxial compression normal to the growth direction. The role of CNT-to-CNT contacts and defects on the bulk thermal resistance are highlighted thermal transport mechanisms that adversely affect the effective thermal conductivity of CNT TIMs. A manuscript has been submitted for internal review.

Chapters 8 provides an overview of efforts devoted to assess the thermal performance of CNT TIM and CNT/Petal TIMs at elevated temperatures (up to 450°C). At 450°C, the CNT and CNT/petal TIMs outperform a bare interface as well as a bare Cu foil. Additionally, both TIMs exhibited adequate mechanically cyclic stability at 450°C. A hysteresis in thermal resistance during the temperature cycle was also observed. Post-mortem SEM images revealed that the CNT TIMs were significantly compacted and plastically deformed while the aggregate structure of the CNT/petal TIMs remained relatively unchanged. For the latter, post-mortem SEM images revealed that the petals on

the surface of the TIM flattened, indicating that upon sufficient pressure and temperature conditions, the surface of the CNT/petal TIM began to conform to the stainless steel heat flux meter. This observation suggests that sufficient pressure and temperature conditions are necessary for CNT/petal TIMs to significantly outperform CNT TIMs.

Chapter 9 provides an overview of the work conducted at Sandia National Laboratories in Albuquerque, NM on molten salt battery materials. A steady-state reference bar technique was employed to measure the thermal conductivities of the separator pellets (LiCl/MgO/KCl) and thermally insulating materials (Fiberfrax board and Min-K). The separator thermal conductivity was measured to be approximately 2.30 W/mK and constant within the pressure range of 400 and 2250 kPa. The effective thermal conductivity of the Fiberfrax board and Min-K insulation materials were measured to be on the order of *O(0.1)* W/mK and *O(0.01)* W/mK, respectively, at 350 and 500 psi. This work was published in the *47th Power Conference Proceedings Conference* in 2016.

2. LITERATURE REVIEW

2.1 Thermal Interface Materials

Thermal pads, thermal greases, and metallic foils are commonly inserted between the components to alleviate the constriction of heat flow by conforming to the surface roughness of the components and filling the gaps between them, thus creating more contact points and paths for heat transport [1]. Moreover, many applications require TIMs to accommodate a variety of stress conditions associated with either external vibrations or mismatches in the coefficient of thermal expansion between the components. However, a given TIM may be best suited for only a specific regime in the mechanical and thermal parameter space associated with an application. For example, thermal pads provide high mechanical conformability and effectively dampen low stress vibrations, yet possess low thermal conductivities on the order of 1 W/mK [2]. Thermal greases are commonly chosen for their ability to accommodate mechanical stresses during operation. Non-conductive thermal greases consist of a matrix of electrically insulating polymers and metal oxide filler materials with thermal conductivities less than 0.5 W/mK [3]. To increase the thermal conductivity to approximately 2 W/mK, metallic particles such as silver are substituted as the filler material [3]. When heated above their eutectic point, solder foils conform to surface asperities and offer the highest thermal performance with

thermal conductivities above 20 W/mK [4]. However, when solidified, solder foils suffer from their inability to withstand mechanical stresses due to their rigidity.

2.2 CNT Growth by Microwave Plasma Chemical Vapor Deposition

CNTs can be synthesized by many different methods including electrolysis, pyrolysis, laser ablation, arc discharge, thermal chemical vapor deposition (CVD) and microwave plasma chemical vapor deposition (MPCVD). In this work, CNTs were fabricated using the MPCVD method and typically exhibit a bamboo-like structure as seen in past studies [5]. The energetic electrons created by the plasma can be used to hasten the dissociation of feed gases (H_2, CH_4 in this work) and produce large quantities of free radical, carbon species that are necessary for CNT nucleation. In the work of Qin et al. [6], it was proposed that one role of the plasma was to enhance the diffusion of carbon species into catalyst particles. In more detail, Bower et al. [7] proposed a process for the nucleation and growth of CNTs in a plasma reactor. Initially starting with a thin catalyst layer (Co) and the annealing process, the surface forms semi-spherical islands, which is driven by surface tension and the lowering of total surface energies. These islands serve as CNT nucleation and growth sites that can dictate tube diameter. As carbon species interact with the islands via dissolution, saturation, and precipitation [7], CNTs nucleate and grow as carbon atoms begin self-assemble.

The remarkable mechanical and thermal properties of individual CNTs are a consequence of their high aspect ratio, cylindrical shape that is sewn together by covalently bonded carbon atoms. The elastic modulus of an individual CNT has been measured to be on the order of terapascals [8, 9] while the thermal conductivity of an individual CNT has

been measured to be as high as 3000 W/mK [10, 11], making them strong candidates to strengthen composite materials and efficiently conduct thermal energy. In order to exploit these extraordinary properties for practical applications, CNTs are often mass-produced on a single substrate to match the length scales of larger components and devices. A remarkable feature of the aggregate structure is the formation of billions of neighboring high aspect ratio CNTs that are moderately parallel and vertical with a tortuous microstructure. The underlying framework that governs the as-grown structure balances the strain energy due to ambient vibrations and mechanical constraints [12] with intra- and inter-tube van der Waals interactions [12-15].

2.3 Mechanical Deformation of CNT TIMs

The same mechanisms responsible for the microstructure of as-grown CNT TIMs also govern the state of its aggregate structure when subjected to external mechanical loading. In response to a compressive stress, the concentric shells of individual multi-walled CNTs bend and form buckles, ripples, or wrinkles in a coordinated manner [9, 14 - 18]. During this coordination, the intra-tube spacing between shells of the CNTs is predominantly preserved as van der Waals interactions oppose the compressive stresses induced from bending [9, 18]. As a result, the buckles, ripples, or wrinkles are most pronounced at the outermost tube and propagate to a lesser degree to the inner shells of the CNTs [9, 18]. The compressive response of CNT TIMs to uniaxial compression similarly incorporates the balance of bending stresses with van der Waals interactions, except at a much larger scale at which the entire structure collectively deforms in unison.

An analogy to the deformation of open-cell foams has been employed in prior research to describe the compressive behavior of CNT TIMs, with the stress-strain evolution divided into three distinct regions that represent linear elastic deformation, the onset of coordinated buckling, and rapid densification of the CNT TIM [12-14, 19-25].

2.4 Carbon Nanotube Thermal Interface Materials

Because of their perceived high thermal conductivity, mechanical compliance, and stability over a substantially large temperature range, CNTs have been extensively studied as thermally conductive elements, including as alternatives to current state-of-the-art TIMs [26-41]. Depending on the synthesis method, CNT TIMs are comprised of high aspect ratio, vertically oriented nanotubes with heights ranging orders of magnitude from 1 μm to 1 mm and diameters from 10 to 100 nm. The efficacy of a CNT TIMs is predicated on the ability of the nanotube constituents to collectively act as a cohesive network of parallel heat conductors. The contact area of a typical CNT TIM is dictated by the van der Waal forces between the nanotubes and the opposing substrate as well as the mechanical properties of the constituent nanotubes and their interactions as a collective network.

By modifying wool theory developed by van Wyk [42] to study the mechanical compression of dense fibrous masses to CNT TIMs, Cola et al. [41] predicted that the real area of contact that a CNT TIM makes with the opposing substrate relative to the nominal area is on the order of 0.1% for a dry, unbonded state with characteristic CNT to substrate contact sizes between 1 to 5 nm. Depending on the synthesis method and growth rate of vertically oriented CNT TIMs, density gradients and height variations of nanotubes represent other morphological features that can affect contact area. The amount of contact

area that the CNT TIM makes with the opposing substrate coupled with their mismatches in vibrational modes, density of states and dimensionality [40] between the nanotubes and opposing substrate have commonly been highlighted as significant contributors to the thermal contact resistance. Panzer et al. [27] performed thermoreflectance measurements on palladium-coated vertically oriented single-walled CNTs and determined that a small fraction of CNTs contribute to heat capacity (and ultimately heat conduction) due to such morphological features and material properties. As a result, developments in innovative bonding and semi-bonding techniques have been employed to counteract the poor CNT tip to opposing substrate contact. Notably, thermal contact resistances as low as 1.3 mm^2 K/W [31] and 2 mm^2 K/W [35] have been measured by thermoreflectance and photoacoustic methods for bonded and semi-bonded TIMs, respectively.

The idea of employing CNTs as a TIM was logically proposed after experiments yielded and molecular dynamics simulations predicted impressively high thermal conductivities for individual single- or multiwalled CNTs (3000 W/mK) [10, 11]. Vertically oriented CNT TIMs can be synthesized using many different methods yielding CNTs of varying alignment, density, height, and quality (defectiveness), and they can be thermally characterized by myriad techniques such as photoacoustic [32 - 34], photothermoelectric [43 - 46], thermoreflectance [27], laser flash [47 - 51], 3ω [52, 53], steady state reference bar [54 - 56], and infrared thermometry [57]. This state of affairs involving different synthesis and measurement techniques has likely been the primary cause of the wide range of reported values for the aggregate or effective CNT TIM thermal conductivity, 0.1 – 265 W/mK [27, 32 - 34, 43 - 57]. This range falls well below the measurements and predictions on the thermal conductivity of individual CNTs [10, 11],

with CNT TIMs producing either thermal insulating behavior of randomly oriented CNT mats [56] or a network of vertically oriented parallel conductors that transport heat as well as metals. Consequently, the CNT TIM can either facilitate or impede thermal transport.

Heat conduction in CNT TIMs is fundamentally complex and difficult to experimentally resolve the transport mechanisms with fidelity. The complexities are embedded in extracting the phonon transport mechanisms that affect heat conduction within individual CNTs, the interactions between adjacent CNTs, and the transmission of heat carriers between CNTs and dissimilar materials. The structural condition of the CNTs (defects and quality) can dictate the thermal conductivity of individual CNTs [58]. The effective thermal conductivity is predicated upon the density of defects in the nanotube walls that serve as phonon scattering sites, the inter-tube spacing and morphology that dictate inter-tube coupling, and the distribution of nanotube heights that control the quantity of nanotubes participating in heat conduction. While the structural properties of individual CNTs and the aggregate morphology of the ensemble can affect the heat transport properties of CNT TIMs, the manner in which the effective thermal conductivity is measured or estimated can also lead to wide discrepancies in reported values. The effective thermal conductivity can be measured or estimated by the aforementioned techniques, which are distinguished by the manner in which the response of the CNT sample to heating is directly measured. The photothermal and thermoreflectance techniques measure the thermal response of the CNT sample using optical methods while the photoacoustic method uses a pressure transducer to measure the acoustic response of a gas medium that is thermodynamically related to heat conduction in the CNT sample. The well-established 3ω technique measures the change in electrical resistance of a metallic

heater in contact with the CNT sample that is related to the temperature rise in the heaters. In order to estimate parameters such as the effective thermal conductivity, these techniques employ regression approaches in which the estimated values depend significantly on the sensitivity of the response variable to the estimated parameter within the framework of the thermal model. Another commonly used measurement technique is the laser flash method in which the thermal diffusivity of the CNT sample is directly measured and the effective thermal conductivity of the CNT layer can be estimated from the product of the thermal diffusivity, α, and volumetric thermal capacitance, ρc_p. The associated estimate of the effective thermal conductivity is depends significantly on the choices for the specific heat capacity, c_p, and mass density, ρ. The former is typically assumed to be that of graphite (approx. 700 J/kg K) while the latter has been estimated to either be on the order of O(100 kg/m^3) [47] or O(1000 kg/m^3) [48 - 50]. This wide range in mass densities translates to a correspondingly wide range (1 to 60 W/mK) in reported effective thermal conductivities. In contrast to the foregoing transient techniques, steady-state methods can directly measure temperature gradients within mediums to estimate thermal conductivity as well as temperature discontinuities at interfaces to infer thermal contact resistances. The primary advantage of such steady-state techniques within the framework of estimating effective thermal conductivity is that knowledge of the density and specific heat capacity is not required. Therefore, the effective thermal conductivity can be estimated in a more direct manner that enables better comparisons between values reported in literature. Marconnet et al. [57] used steady-state, high-resolution infrared microscopy to visualize the temperature gradient in MWCNT arrays and measured effective thermal conductivities ranging from 0.3 to 3.6 W/mK, attributing higher effective conductivities to denser packing

fractions. By employing a steady-state method similar to the ASTM standard one-dimensional reference bar technique, Pal et al. [55] estimated the effective thermal conductivity of their MWCNTs and thermal contact resistances to be 0.8 W/mK and 150 mm^2 K/W, respectively. In their work, the effective thermal conductivity and thermal contact resistance were inferred from the linear relationship between the total thermal resistances (bulk and contact) of three MWCNT TIMs and their respective heights (14, 40, and 72 μm).

3. EXPERIMENTAL SETUP

3.1 Photoacoustic Characterization of Multi-Layered Structures

3.1.1 Introduction

The photoacoustic effect (PA) in solids was first described by Parker in 1973, and a more general quantitative model was developed by Rosencwaig and Gersho three years later. While spectroscopic techniques based on the PA effect were initially used to measure optical absorption coefficients of solids, extensions of the PA theory to characterize multi-layer structures have been developed [59-66]. The technique has been used to successfully measure not only the thermal conductivity of thin films [59-66] but also the thermal resistance of both bonded and non-bonded interfaces [32-39].

3.1.2 Theory

A typical multi-layered structure that can be characterized is shown in Figure 3.1. The structure consists of a backing layer 0 and N successive layers. An additional gas medium (air or helium), denoted as layer N + 1, is in contact with layer N (thin titanium layer). The backing layer 0 and gas medium (N+1) are assumed to be thermally thick.

The transient temperature distribution in the multi-layer structure, which is induced by periodic laser heating, can be derived by solving a set of one-dimensional transient heat conduction equations. A detailed derivation is presented in Ref. 59.

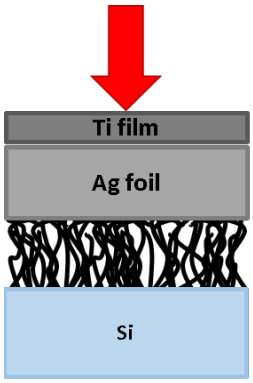

Figure 3.1. Schematic of typical CNT TIM thermally characterized by PA technique.

In summary, the governing equation for thermal transport in each layer is defined as

$$\frac{\partial^2 \theta_i}{\partial x^2} = \frac{1}{\alpha_i}\frac{\partial \theta_i}{\partial t} - \frac{\beta_m I_o}{2k_m}\exp\left(\sum_{m=i+1}^{N} -\beta_m l_m\right) e^{\beta_i (x-l_i)}\left(1+e^{j\omega t}\right) \tag{3.1}$$

where $\theta_i = T_i - T_{amb}$ is the modified temperature in layer i, T_{amb} is the ambient temperature, β_i is the optical absorption coefficient, I_o is the incident laser flux, l_i is the is the distance from the interface between the top layer and gas medium, ω is the modulation frequency, and t is time. The solution to the governing equations consists of three components: a transient, steady dc and steady ac. Since the lock-in amplifier used in a PA measurement only detects the periodic signal, only the steady ac component is usable. The steady ac component in each layer has a complex temperature distribution defined as

$$\tilde{\theta}_{i,s} = \left[A_i e^{\sigma_i (x-l_i)} + B_i e^{-\sigma_i (x-l_i)} - E_i e^{\beta_i (x-l_i)}\right] e^{j\omega t} \tag{3.2}$$

where σ_i is defined at $(1+j)a_i$ with j is imaginary and a_i is the thermal diffusion coefficient representative of the thermal diffusion length, which is dependent upon the thermal

diffusivity of the layer as well as the modulation frequency. The coefficients A_i and B_i are determined from two boundary conditions at the interface of two layers that require the heat flux to be constant across the interface with an associated temperature drop. The temperature in the gas layer is thermodynamically related to the pressure oscillation induced by both a thermal and mechanical piston, which is ultimately sensed by a microphone in the form of a phase shift and amplitude. The periodic temperature in the gas layer is defined as

$$\tilde{\theta}_{N+1,s} = B_{N+1} e^{-\sigma_{N+1}} e^{j\omega t} \tag{3.3}$$

According to the theory of Hu *et al.* [59], the phase shift of the PA signal is $Arg(B_{N+1}) - \pi/4$, and the amplitude of the PA signal is $Abs[(1-\rho)\cdot B_{N+1} P_o / \sqrt{2} l_{N+1} a_{N+1} T_o]$, where P_o and T_o are the ambient pressure and temperature, respectively.

3.1.3 Experimental Setup

The PA apparatus that has been described in detail in previous work [32, 59] was used to characterize thermal contact resistances in Chapters 4, 5, and 7. The experimental setup is illustrated schematically in Figure 3.2 and images of the actual apparatus are shown in Figure 3.3 and 3.4. A new cell was fabricated from an acrylic block as the previous cell was in poor condition after numerous runs during the work of Cola at high pressures and temperatures. The new cell consists of a more robust gas feed and microphone housing. Additionally, the cell base allows for more consistent alignment of sample with the laser beam. For a multilayer structure, the PA technique can resolve both bulk and component resistances in which the measured resistance in Figure 3.1 is defined as

$$R_{meas}(P) = R_{bulk} + R_{contact} = \frac{\overline{h}_{comp}}{k_{eff}} + R_{Ag\ foil-CNT\ TIM} + R_{CNT\ TIM-Ag\ foil} \tag{3.4}$$

where R_{bulk} is the bulk resistance of the CNT TIM defined by the ratio of the compressed CNT TIM height, h_{comp}, to the effective thermal conductivity of the CNT TIM, k_{eff}. $R_{contact}$ is the combined contact resistances of the CNT TIM with the Ag foil and Si growth substrate. The PA technique can resolve the thermal diffusivity or thermal conductivity of layers of interest, however, meticulous care must be taken when accounting for the contact resistance between the layer (Ti) that absorbs the laser irradiation and the layer of interest [65]. For measuring the total thermal resistance between the Ag foil and bottom substrate, as done throughout this work, the PA technique can resolve resistance values between approximately 0.1 and 100 mm^2 K/W [32]. The lower and upper measurement limits are determined by the thermal penetration depth within the layer of interest in which the layer is substantially thermally thin or thick, respectively.

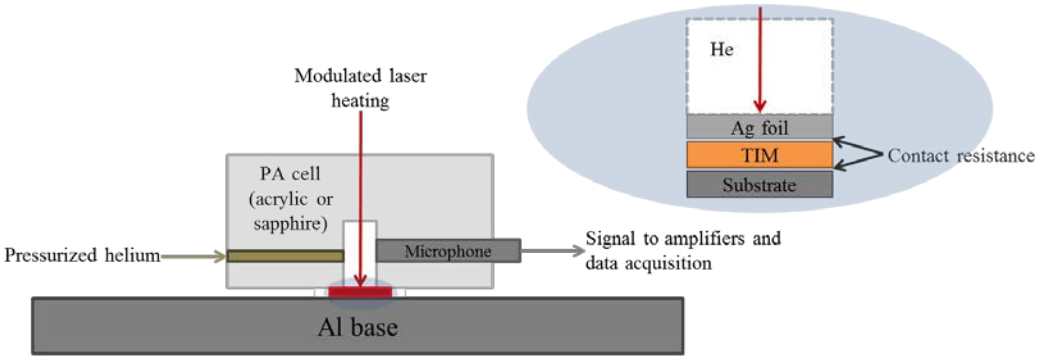

Figure 3.2. Schematic of PA apparatus.

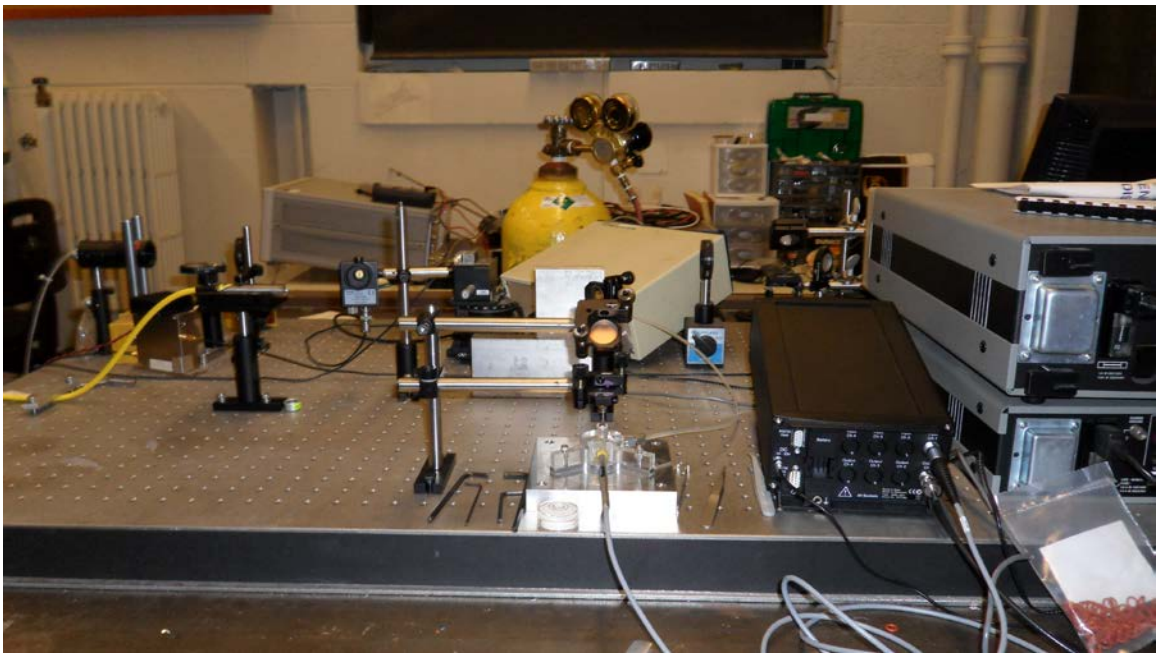

Figure 3.3. Image of PA apparatus showing the laser, cell, helium tank, lock-in amplifier, function generator and conditioning amplifier.

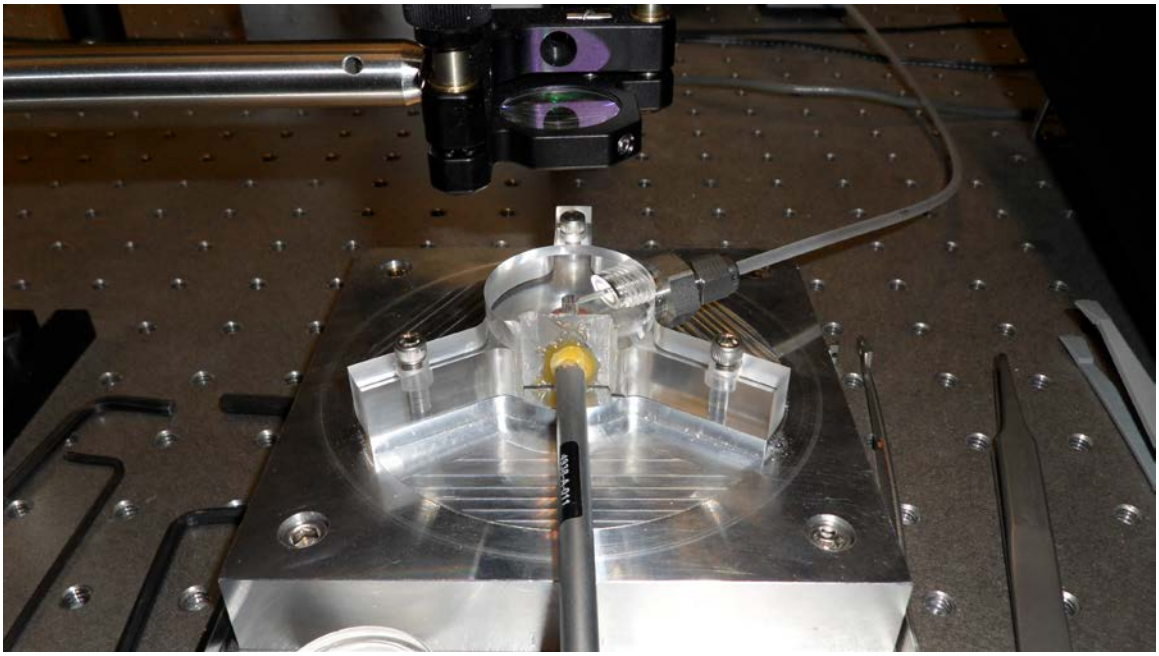

Figure 3.4. Photograph of PA cell showing test stage, microphone and gas feed.

In a given PA measurement, the sample surface is surrounded by a sealed acoustic cell that is pressurized with He gas in a pressure range from 20 to 145 kPa. The PA measurement can also be performed in air at standard temperature and pressure. The sample is then periodically heated over a range of frequencies by a 350 mW, modulated laser source. Using the acoustic signal in conjunction with the thermal model above, thermal interface resistances and thermal diffusivities of specific layers can be determined using a least-squares fitting method.

The measurement uncertainty arises from the capabilities of the microphone to sense the amplitude and phase shift signals, which are typically on the order of ± 1.0° [32]. As previously reported by Cola et al. [32], the uncertainties due to 'known' parameters and laser drift are negligible in comparison to the measured phase of the reference sample from which the ± 1.0° variation manifests itself. The uncertainty in measuring the thermal interface resistance of CNT TIMs shown in Figure 3.2 is lower, approximately 80% less than the reference sample, because they possess a higher thermal resistance and produce a stronger signal [32]. The uncertainty associated with estimation of thermal quantities such as thermal conductivity and thermal resistance is evaluated by determining range of property values that yield amplitude or phase shift values within the measurement uncertainty [65].

3.1.4 Measurement of the Thermal Conductivity of SiO_2

To validate the accuracy of the new PA cell, the thermal conductivity of a thermally grown, 0.5 μm thick SiO_2 layer on Si was measured. An 80 nm Ti absorption layer was deposited atop the SiO_2 layer. The sample was tested at a pressure of 5 psi. The phase shift versus modulation frequency data is shown in Figure 3.5. The phase shift was used as it produces a steadier signal than the amplitude and is indicative of the PA measurements in this work. In a similar manner to Hu et al. [59], a wide range of frequencies was used to probe the SiO_2 layer (1 – 6 kHz). While a maximum frequency of 20 kHz was used in the work of Hu et al. [59], the current laser used in this work was to oscillate at a maximum frequency of 6 kHz. Nonetheless, the maximum frequency is well above the range of frequencies (300 – 1000 Hz) appropriate for CNT TIMs measured in this work. Using an updated algorithm that simplifies choosing initial guesses, a thermal conductivity of the SiO_2 film was measured to be 1.49 ± 0.17 W/mK. This result is in close agreement with the work of Hu et al. [59].

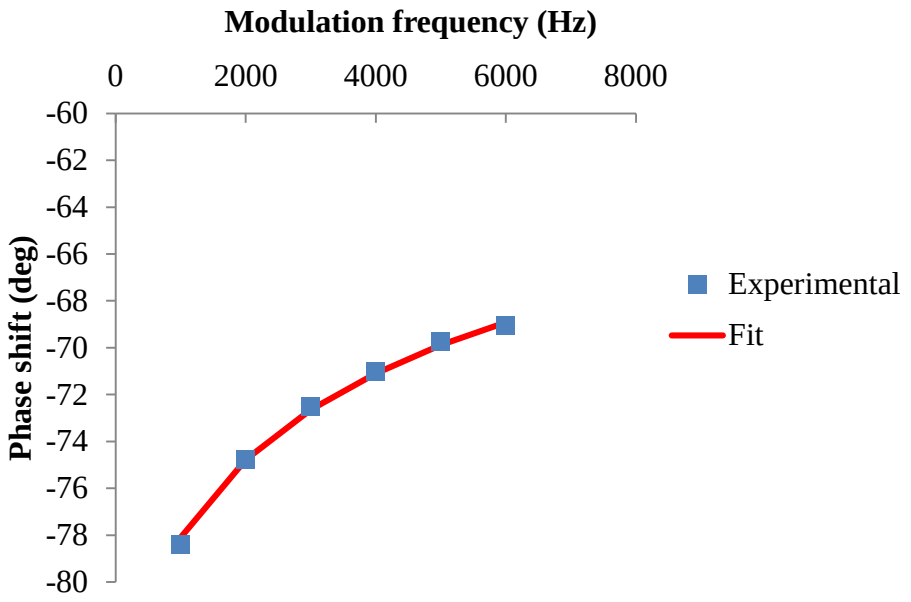

Figure 3.5. Experimental and fitted phase shift data for 0.5 μm thick, thermally grown SiO_2 layer on Si.

3.2. One-Dimensional Reference Bar Measurement with *in situ* Solder Bonding and Paraffin Wax Infiltration (supporting documentation for Chapter 6)

3.2.1 Theory

To measure thermal contact resistance, the technique uses a one-dimensional steady-state (1DSS) heat conduction model to determine the heat flux through two heat flux meters of known thermal conductivity via equally spaced thermocouples or infrared thermography to measure temperature. At the junction between the heat flux meters, the heat flux is constant while a temperature drop exists due to the thermal contact resistance. By extrapolating the temperature profile to the interface, the thermal resistance between the two heat flux meters can be determined from the ratio of the temperature drop to that of the heat flux. Uncertainties in determining the thermal resistance arise from thermocouple

location, temperature measurement, regression analysis, and alignment of the heat flux meters.

3.2.2 Experimental Setup

The apparatus used in this work (Chapter 6) consisted of a precision linear guide with low-friction slide features and ball-in-socket joints to account for heat flux meter misalignment and surface nonplanarity [66]. The heat flux meters were 1 cm^2, 38 cm long copper-molybdenum (CuMo) bars (15/18 composition). Additionally, insulating thermoplastic housing was used to minimize heat loss to less than 10% and the thermocouples were calibrated with an uncertainty of 0.03°C [66]. The measurement uncertainty was expected to be 15% for thermal resistances as low as 4 mm^2 K/W with significant contributions from the uncertainty in the locations of the thermocouples along the length of the heat flux meters and tolerances associated with the diametric clearance of the thermocouple bores [66]. The measurement uncertainty is also dependent on thermal resistance because the accuracy to which the thermocouples are calibrated (0.03°C) has greater influence at smaller temperature differences measured at the interface (see Figure 3.6 below). Therefore, the actual measurement uncertainties for thermal resistances greater and less than 8 mm^2 K/W are below and above 15%, respectively. The measurement uncertainty for low thermal resistances can be improved by increasing the heat rate across the interface and by choosing an appropriate heat flux meter. Further details on the measurement technique and apparatus are in Reference 66.

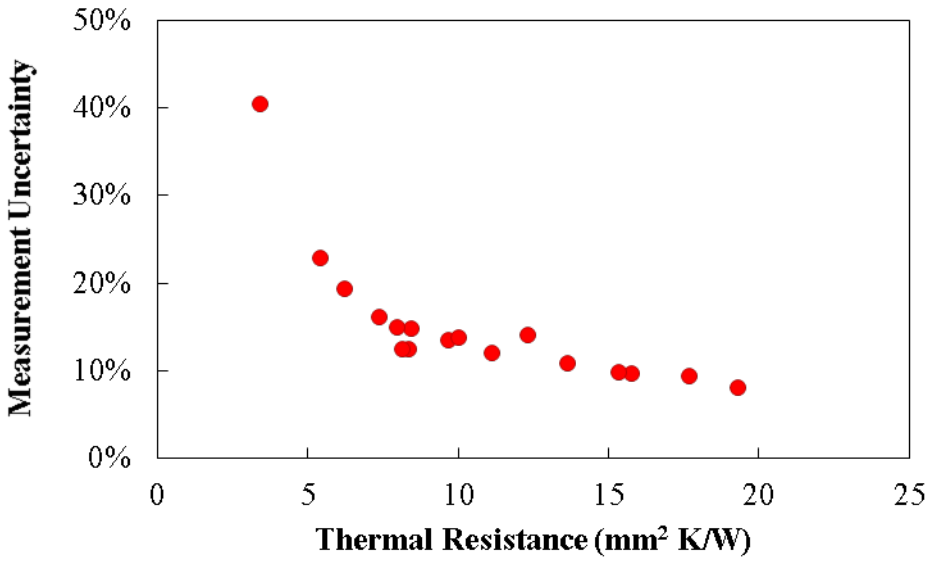

Figure 3.6. Dependence of measurement uncertainty on thermal resistance for 1DSS reference bar technique.

Prior to solder bonding, the tips of the CNT TIMs were metallized with 150 nm of nickel and 250 nm of gold to promote adhesion of the CNT tips to the solder foil. In the test fixture, thin solder foils (Indalloy Sn63, 121, 265) of 0.051 mm thickness bonded the CNT TIMs to the CuMo heat flux meters by raising the temperature above the eutectic point of the solder foil and subsequently cooling until solidified. The bonding temperature was raised to 10-30°C above the eutectic point for 30 seconds while the bonding pressure was maintained at 30 psi. Once bonded, the samples were tested at interface pressures between 135 and 400 kPa with and without the infiltration of paraffin wax. In the fixture, the CNT TIM was infiltrated with paraffin wax using a syringe. Figures 3.7 and 3.8 below show wetting of the solder to the CNT TIMs. Additionally, Figure 3.8 indicates that while the solder engages the CNT tips quite well, it does not penetrate deeply into the CNT TIM. The images were acquired by solder bonding similar CNT TIMs to Si substrates, potting the interface in epoxy, and slicing the stack for imaging.

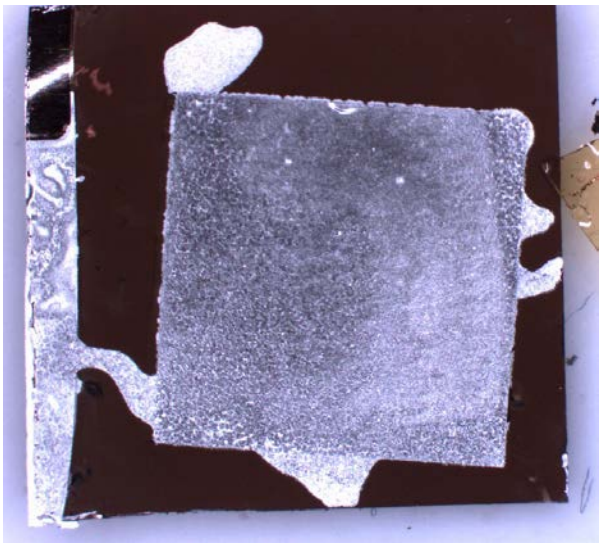

Figure 3.7. Top view of solder wettability of metalized CN T TIM.

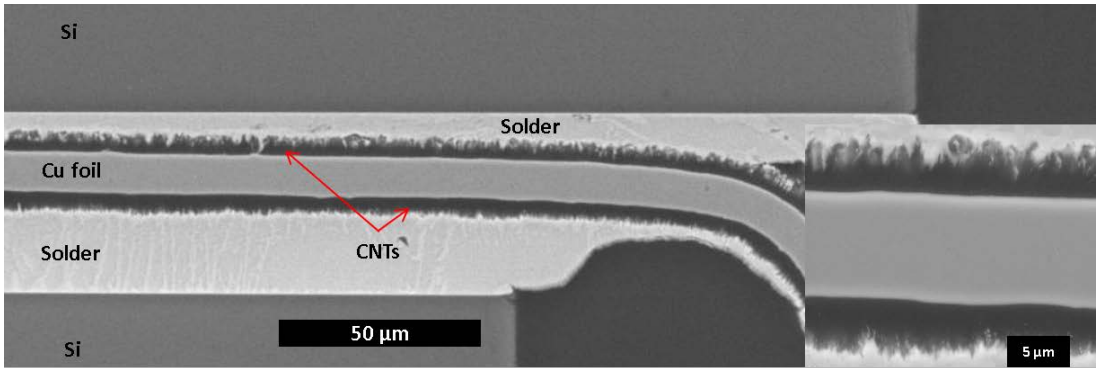

Figure 3.8. Cross section view of solder bonded CNT TIM. Note that this sample was potted in epoxy and sliced to obtain cross section view.

3.2.3 Comparison of 1DSS Reference Bar and Photoacoustic Techniques

Thermal engineers are equipped with a variety of techniques to measure the thermal properties of materials as well as the contact resistance between these materials and other components. Therefore, the ability to confidently compare measurements of such quantities across a variety of measurement techniques is imperative for further development of materials such as TIMs. In this work, the 1DSS reference bar and photoacoustic (PA) techniques are extensively employed to measure the total thermal resistance as well as estimate the contact resistance and effective thermal conductivity of CNT TIMs. As shown in Figure 3.9, measurements of the total thermal resistance of unbonded CNT TIMs by the reference bar technique are approximately a factor of three greater than the total thermal resistance of unbonded CNT TIMs measured by the photoacoustic technique. Variations in the total thermal resistance for each plot group (i.e., unbonded, Pd bonded, solder bonded, and solder bonded with paraffin wax infiltration) are due to differences in CNT TIM height.

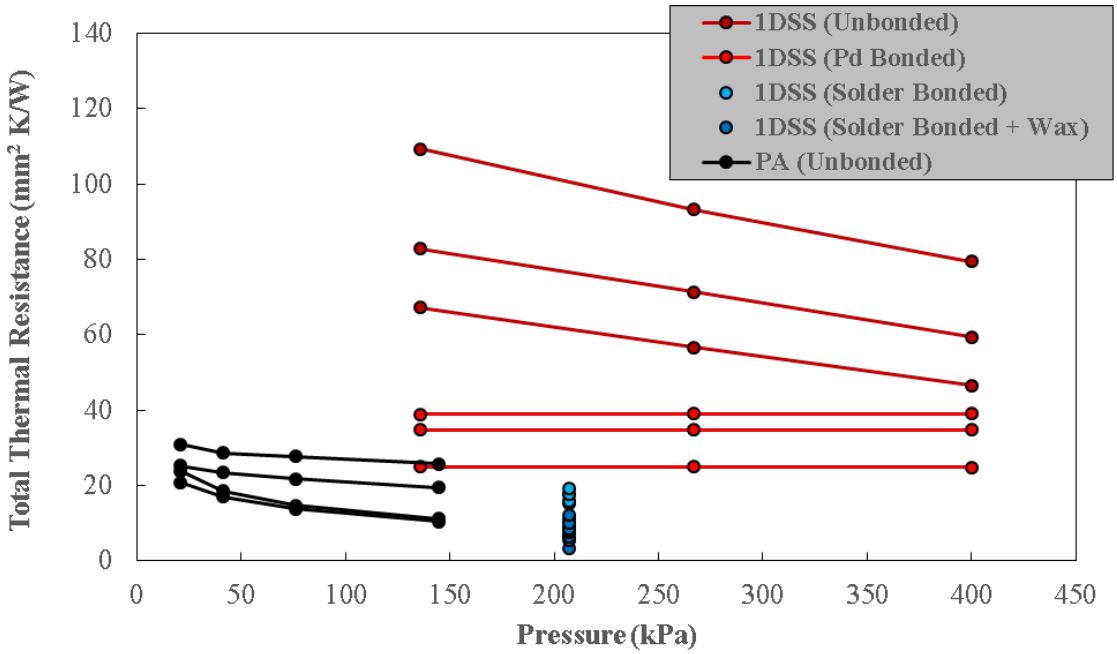

Figure 3.9. Comparison of total thermal resistance of CNT TIMs measured by the 1DSS reference bar and PA techniques.

When the contact resistance (Figure 3.10) and effective thermal conductivity (Figure 3.12) are estimated from the total thermal resistance using the methodology employed in Chapters 6 and 7, we observe that the discrepancy in the total thermal resistance measured by the two techniques is solely due to the contact that is formed between the CNT TIM and opposing surfaces. Furthermore, the rigid and macroscopically irregular surface of the heat flux meters used in the 1DSS technique (Figure 3.11) poorly engage the CNT TIM relative to the flexible and smooth surface of the Ag foil used in the PA technique. Hence, normalizing the total thermal resistance by the apparent contact area (i.e., cross-sectional area of a heat flux meter) rather than the true contact area results in a higher resistance. As observed in Figure 3.10, the engagement is increased as the CNT TIMs are bonded to the heat flux meters and the contact resistances estimated from the 1DSS measurements begin to decrease to within the range of contact resistances estimated from the PA technique. In

contrast, the effective thermal conductivities estimated from both techniques are on the order of *O*(1 W/mK) and exhibit similar dependencies on pressure.

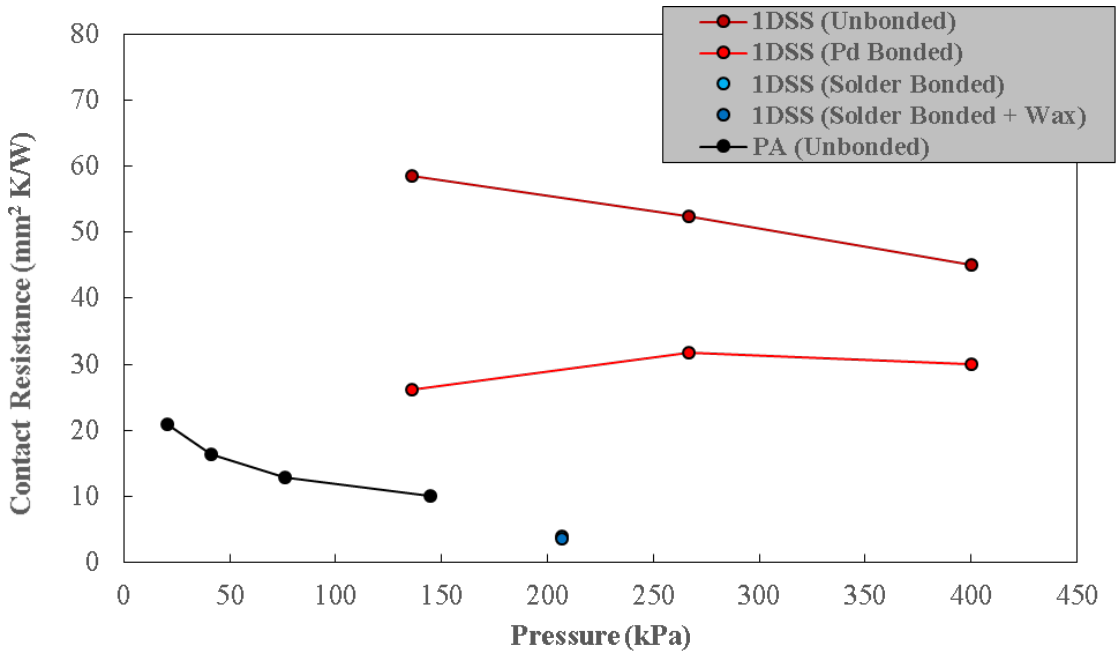

Figure 3.10. Comparison of contact resistance of CNT TIMs estimated from the total thermal resistance measured by the 1DSS reference bar and PA techniques.

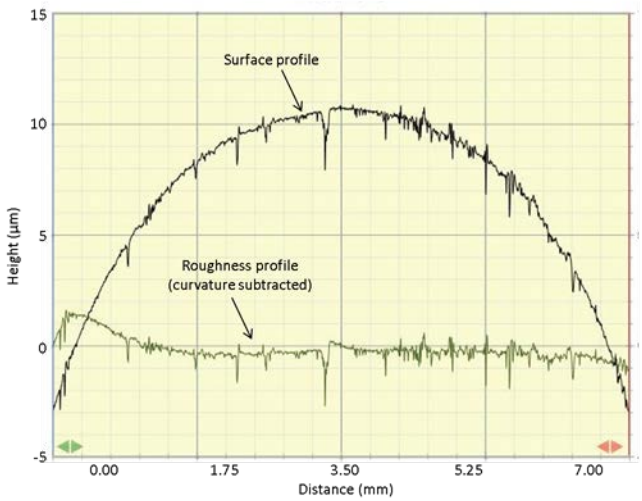

Figure 3.11. Topological surface profile of typical heat flux meter used in 1DSS reference bar technique.

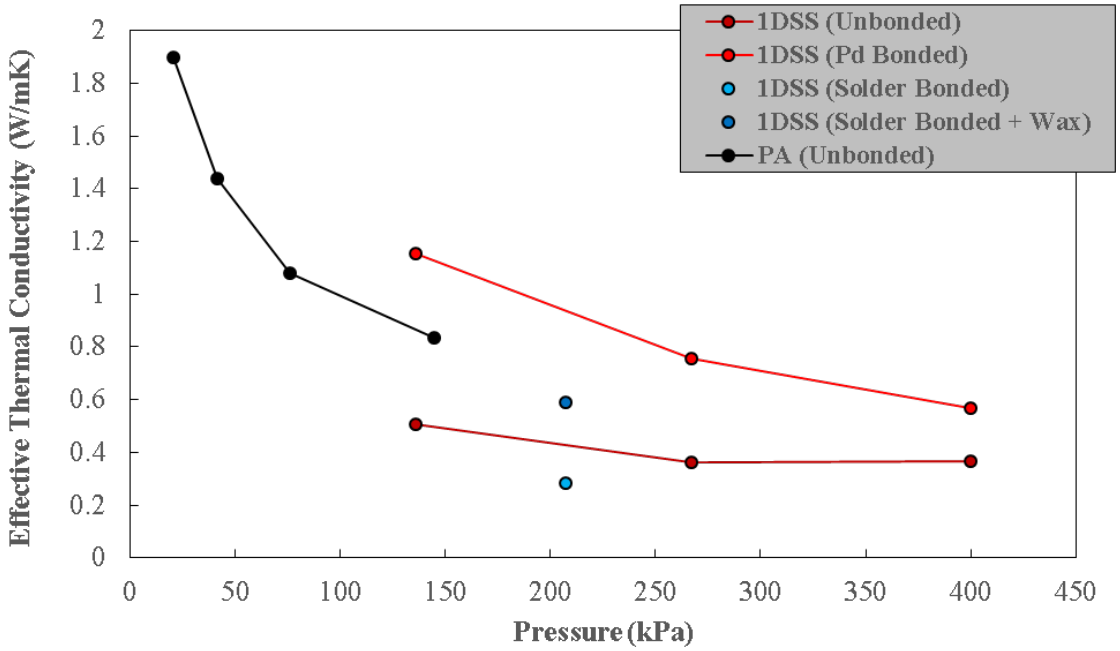

Figure 3.12. Comparison of effective thermal conductivity of CNT TIMs estimated from the total thermal resistance measured by the 1DSS reference bar and PA techniques.

3.3 Palladium Thiolate Bonding of CNT TIMs

3.3.1 Background

Metal alkanethiolates can serve as sources of metal clusters upon thermolysis and yield either metal or metal sulfide nanoparticles [68]. While metal alkanethiolates are insoluble in most organic solvents, Pd alkanethiolates have been reported to be soluble in these solvents and also exhibit repeated self-assembly [69]. The soluble nature of Pd alkanethiolates in such solvents like toluene makes them attractive for forming smooth, thin films on substrates. In a previous investigation by Bhuvana and Kulkarni [70], Pd hexadecanethiolate has been patterned using electron beam lithography and subsequent formation of Pd nanoparticles on thermolysis was demonstrated. Energy-dispersive spectral (EDS) values before and after thermolysis were 21:71:8 and 90:9.6:0.4 for

(Pd:C:S), respectively [69]. Most notably, electrical measurements yielded resistivity values of Pd nanoparticles that were similar to that of bulk Pd. In Section 4.1, we used Pd hexadecanethiolate (Figure 3.13) to coat the CNT sidewalls with Pd nanoparticles. Upon thermolysis, a strong bond at the CNT/Ag interface was observed.

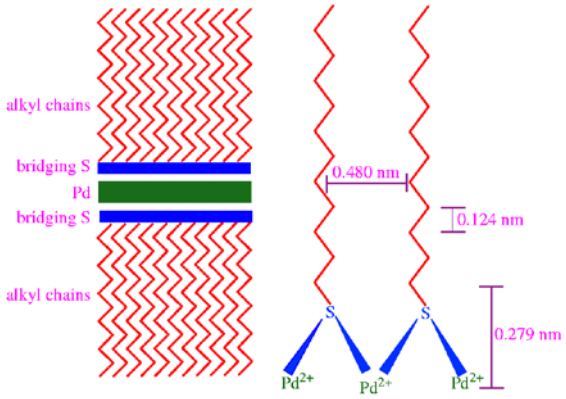

Figure 3.13. $Pd(SC_{16}H_{35})_2$ structure [69].

3.3.2 Bonding Process

For preparation of Pd hexadecanethiolate, an equimolar solution of $Pd(OAc)_2$ (Sigma Aldrich) in toluene is added to hexadecanethiol and stirred vigorously. Following the reaction, the solution becomes viscous and the initial yellow color deepens to an orange-yellow color. The hexadecanethiolate is washed with methanol and acetonitrile to remove excess thiol and finally dissolved in toluene to obtain a 200 mM solution. Using a micropipette, approximately 16 μL of Pd hexadecanethiolate is added to the CNT array. The CNT array is then heated for 5 minutes at 130°C to evaporate the toluene. Finally, the components of the two TIM structures tare formed by sandwiching the substrates under a pressure of 273 kPa and commencing thermolysis at 250°C for 2 hours in air. Figure 3.14 contains an FESEM image of a CNT array after thermolysis at 250°C. The Pd

nanoparticles that decorate the CNT walls typically range from approximately 1 to 10 nm. Similar to other studies [71, 72], we assume that Pd nanoparticles preferentially attach to defect sites in the CNT sidewalls.

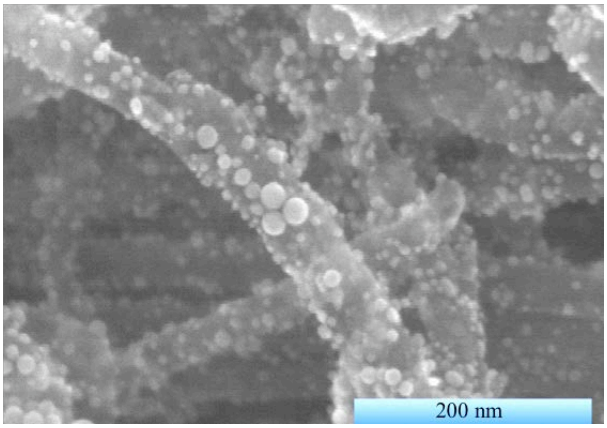

Figure 3.14. Post-thermolysis FESEM image of CNT array on Si substrate.

4. PALLADIUM THIOLATE BONDING OF CARBON NANOTUBE THERMAL INTERFACES

4.1 Introduction

This study aimed to utilize CNT TIMs enhanced with palladium (Pd) nanoparticles to achieve low thermal interface resistances suitable for electronics in a wide temperature range. In particular, two possible enhancements of Pd nanoparticle-coated CNTs on interface conductance are assessed. The first enhancement is an increase in contact area between the CNT 'free tips' and an opposing metal substrate that is formed from the Pd weld. This increase in contact area mitigates the phonon bottleneck at the CNT/metal substrate interface. Secondly, we consider an increase in electron density of states (DOS) near the Fermi level at the CNT/metal substrate interface that is a result of charge transfer between CNTs and Pd nanoparticles. In particular, we discuss the possibility of using electrons as a secondary energy carrier at the interface. One- and two-sided interfaces, comprised of CNT arrays grown on Si substrates, are bonded to opposing metal substrates using a new method that utilizes the behavior of Pd hexadecanethiolate upon thermolysis. Using a transient PA technique, bulk and component thermal interface resistances of the Pd-bonded CNT interfaces were resolved.

Recent thermal resistance values for CNT based TIMs have been measured to be between 1 – 20 mm^2 K/W [26-41]. The thermal resistance values include both bonded

and non-bonded interfaces, and measurements were obtained using different characterization techniques (1DSS reference bar, thermoreflectance, PA, and 3ω). Weak bonding at heterogeneous interfaces, differences in phonon dispersion and density of states, and wave constriction effects are factors that could hinder further reduction in thermal contact resistance. Adverse phonon constriction can be moderated by increasing the interfacial contact area. In an effort to increase the interfacial contact area, developments in bonded and semi-bonded CNT TIMs have rendered thermal interface resistances as low as 1.3 mm^2 K/W [31] and 2 mm^2 K/W [34], respectively. CNTs exhibit ballistic conduction of electrons in the outermost tubes [73] and ohmic current-voltage characteristics with certain metals [74-76]. When this effect is coupled with a strong metallic-like bond at the CNT/metal substrate interface, phonon constriction could be circumvented by using electrons as a secondary energy carrier. A possible way to achieve electron transmission is through a strong CNT/metal substrate bond and sufficiently high electron DOS at the interface.

Functionalizing CNTs with metal nanoparticles (Pt, Au, Pd, Ag, Au) has been an area of growing interest for a diverse set of applications [72, 77 - 79]. For example, a biosensor [77] involving Au/Pd nanocube-augmented SWCNTs showed significant increases in glucose sensing capabilities. The increased performance was attributed to a highly sensitive surface area, low resistance pathway at the nanocube-SWCNT interface, and selective enzyme adhesion, activity, and electron transfer at the enzyme, Au/Pd nanocube interfaces. Metal nanoparticles can adhere to CNTs through covalent or van der Waals interactions, which can lead to charge transfer. Voggu et al. [80] performed *ab initio* calculations on semiconducting single-walled CNTs interacting with Au and Pt

nanoparticles and found a significant increase in the ratio of metallic to semiconducting tubes. Charge density analysis showed a decrease in electron density in the valance band of Au and an increase in the outer orbitals of C, indicating direct charge transfer. A recent study [72] also found significant changes in the Raman G-band peak intensity for pristine and silver nanoparticle-decorated metallic SWCNTs, indicating that the nanoparticles alter the electronic transitions of the tubes. With its high work function [81] and strong adhesion to CNTs, Pd has proven to be a metal that electronically couples well to CNTs [74-76, 81]. Additionally, it has been suggested that efficient carrier injection from Pd monolayers to graphene can be accomplished because of the band structure that results from the hybridization between the d orbital of Pd and p-π orbital of graphene [82].

4.2 Experimental Setup

4.2.1 CNT TIM Fabrication and Characterization

In manner similar to that described by Xu and Fisher [29], an electron beam evaporative system was used to deposit a tri-layer metal catalyst stack consisting of 30 nm Ti, 10 nm Al, and 3 nm Fe on polished intrinsic Si substrates. For a two-sided interface, the tri-layer catalyst was deposited on both a Si substrate and 25 μm thick Cu foil purchased from Alfa Aesar (Puratronic®, 99.999% metals basis). Vertically oriented CNT arrays of moderately high density were then synthesized in a SEKI AX5200S microwave plasma chemical vapor deposition (MPCVD) system described in detail in previous work [83]. In summary, the growth chamber was evacuated to 1 Torr and purged with N_2 for 5 min. The samples were heated in N_2 (30 sccm) to a growth temperature of 900^{o}C. The N_2 valve was then closed

and 50 sccm of H_2 was introduced to maintain a pressure of 10 Torr in the growth chamber. After the chamber pressure stabilized, a 200 W plasma was ignited and 10 sccm of CH_4 was introduced to commence 10 minutes of CNT synthesis. The samples were imaged using a Hitachi field-emission scanning electron microscope (FESEM). Figure 4.1 contains images of the vertically oriented CNT arrays synthesized on Si. CNT arrays grown on Cu foil are similar. The array densities were estimated to be approximately 10^8-10^9 CNTs/mm^2. This estimation was conducted by manually counting CNTs from five different array locations at a moderate magnification in the FESEM. The average CNT diameter for each array was approximately 30 nm while the array heights were approximately 15-25 μm.

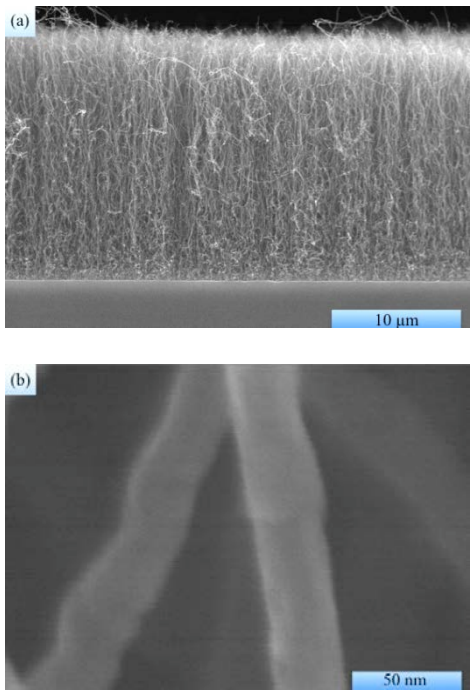

Figure 4.1. CNT arrays synthesized on Si substrate. (a) FESEM cross-section image illustrating array height and (b) FESEM image illustrating CNT diameter.

4.3 Results and Discussion

The PA technique was used to resolve bulk thermal interface resistances of one- and two-sided TIMs with configurations of Si/CNT/Ag and Si/CNT/CNT/Cu. The latter samples had CNT arrays grown on both the Si and Cu substrates, and the resulting interface formed a two-sided, Velcro™-like structure (Figure 4.2). In addition, component resistances were resolved on a separate Si/CNT/Ag sample to elucidate possible mechanisms for enhanced performance.

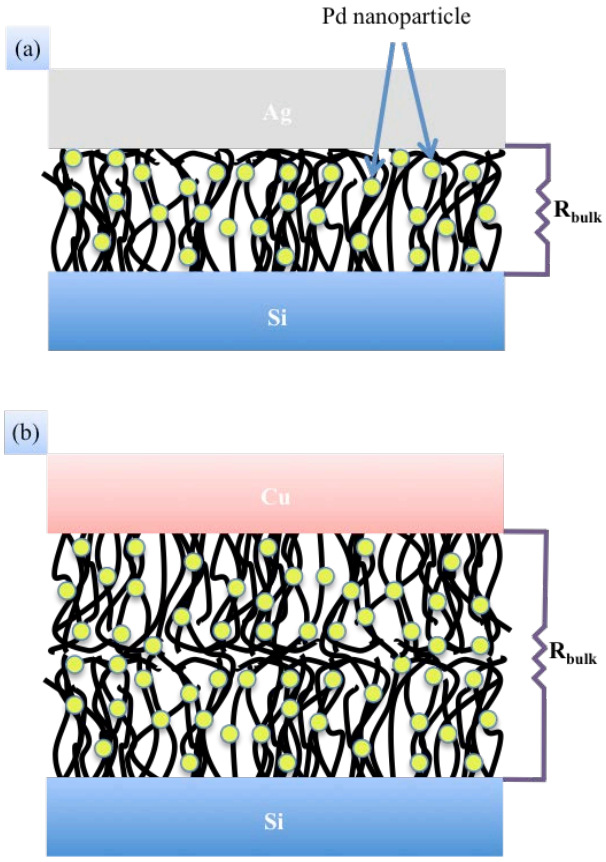

Figure 4.2. Cross-sections of various TIM structures tested using PA technique. (a) Si/CNT/Ag and (b) Si/CNT/CNT/Cu.

In order to ensure proper operation of the pressure-field microphone used in the PA setup, the maximum temperature tested was 250°C, and the chamber pressure was limited

to 34 kPa. Bulk resistance measurements for the Si/CNT/Ag and Si/CNT/CNT/Cu samples were taken in a temperature range of 27°C to 250°C while the component resistance measurement on the second Si/CNT/Ag sample was performed at 27°C. Figure 4.3 shows bulk thermal resistance values as a function of temperature for the Si/CNT/Ag and Si/CNT/CNT/Cu samples. The resolved component resistances for the second Si/CNT/Ag are tabulated in Table 4.1.

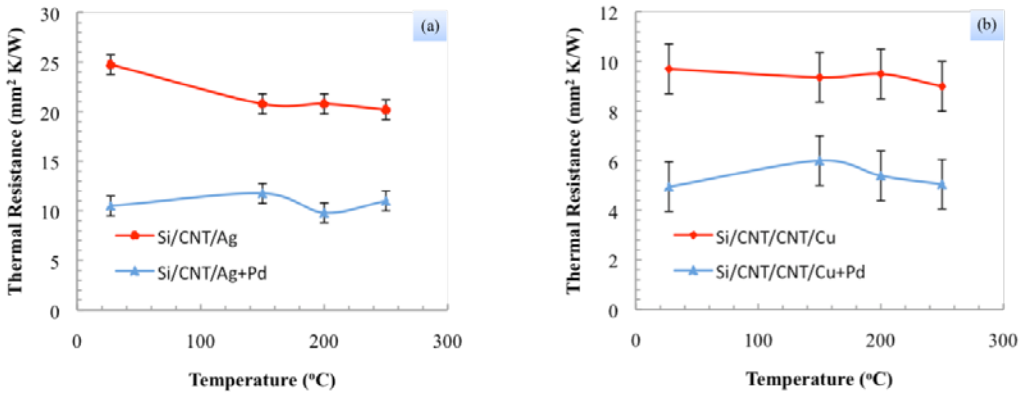

Figure 4.3. Bulk thermal interface resistance as a function of temperature. (a) Si/CNT/Ag w/ and w/o Pd nanoparticles and (b) Si/CNT/CNT/Cu w/ and w/o Pd nanoparticles.

Table 4.1. Component thermal resistances for Si/CNT/Ag structure with and without Pd nanoparticles.

Sample	$R_{Si\text{-}CNT}$ (mm^2 K/W)	R_{CNT} (mm^2 K/W)	$R_{CNT\text{-}Ag}$ (mm^2 K/W)
Si/CNT/Ag	2 ± 1	< 1	40 ± 4
Si/CNT+Pd/Ag	< 1	< 1	15 ± 1

Within the temperature range, the Si/CNT/Ag and Si/CNT/CNT/Cu structures decorated with Pd nanoparticles significantly outperform the structures without Pd

nanoparticles where the average thermal resistance value for the Pd nanoparticle-enhanced structures was 11 mm^2 K/W and 5 mm^2 K/W, respectively. Averaging thermal resistances across the temperature range yielded reductions of thermal resistance across the interface of approximately 50% in both cases. In addition, all structures exhibited only small variations in performance across the temperature range, indicating thermal stability and applicability to devices that operate in this temperature range. To assess the effect that toluene has on the morphology of the CNT array and thermal transport, an additional set of samples were fabricated under the same heating and loading conditions and tested by PA. The interface resistances tabulated in Table 4.2 indicate that while toluene is expected to significantly alter the CNT array morphology, its effect on thermal transport is negligible compared to the welding process that occurs during thermolysis.

Table 4.2. Bulk thermal resistances for Si/CNT/Ag structures with and without Pd nanoparticles and/or toluene.

Sample	$R_{Si\text{-}CNT}$ (mm^2 K/W)
Si/CNT/Ag	21 ± 1
Si/CNT+toluene/Ag	21 ± 1
Si/CNT+Pd/Ag	14 ± 1

Thermal testing was proceeded by assessment of the Pd enhanced bond by FESEM. Figures 4.4 and 4.5 contain images of the structures after the bond was broken and the substrates were separated. For the Si/CNT/Ag structure, the Si and Ag foil substrates are depicted in Figure 4.4 while the Si and Cu foil substrates of the Si/CNT/CNT/Cu structure

corresponds to Figure 4.4. Clumps of CNTs that either remain attached to their Si growth substrate or are bonded to the Ag foil are readily seen in Figure 4.4. Additionally, Figure 4.4 (a) shows a mesoscopic chasm in the CNT array and at higher magnification, Figure 4.4 (b) reveals sites in which CNTs were once attached to the growth substrate. Examination of Figures 4.4 (c) and (d) indicates the clumps of CNTs are also attached to the Ag foil. While not observable in the Si/CNT/Ag structure, the CNT arrays in Figures 4.5 (a) and (c), in particular the latter, resemble a topographical landscape indicating that significant bonding occurred at or around the CNT/CNT interface and most likely depends on the extent that one array penetrates into the other.

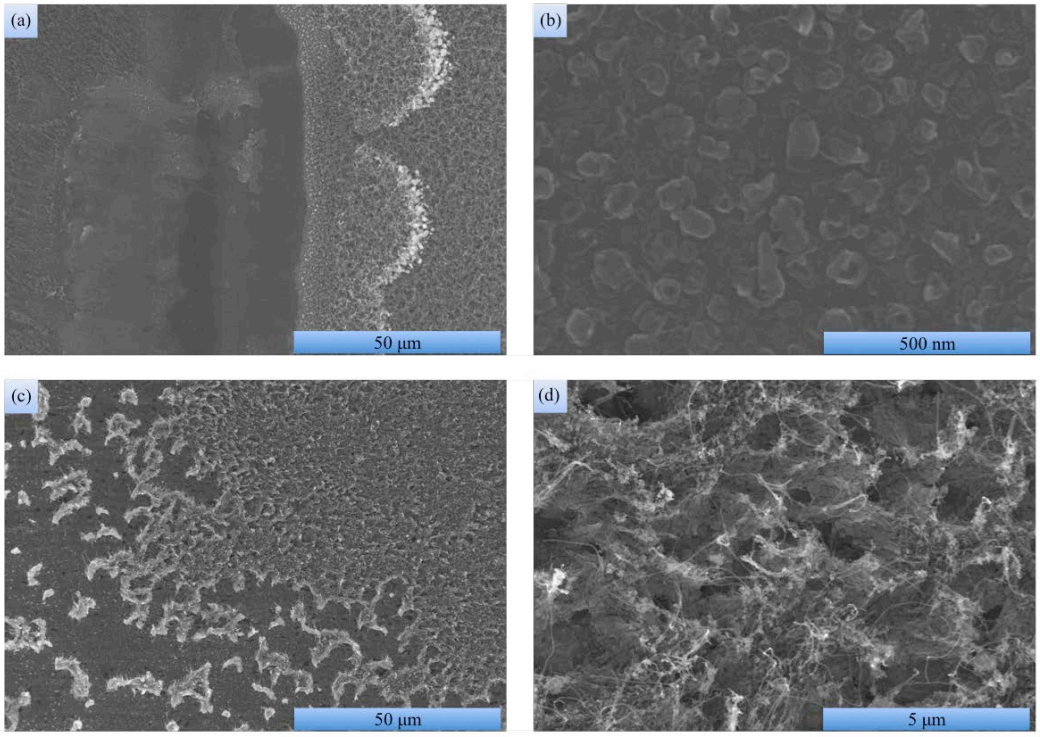

Figure 4.4. FESEM images of Si/CNT/Ag foil structure after detachment. (a) and (b) correspond to the Si substrate while (c) and (d) correspond to the Ag foil.

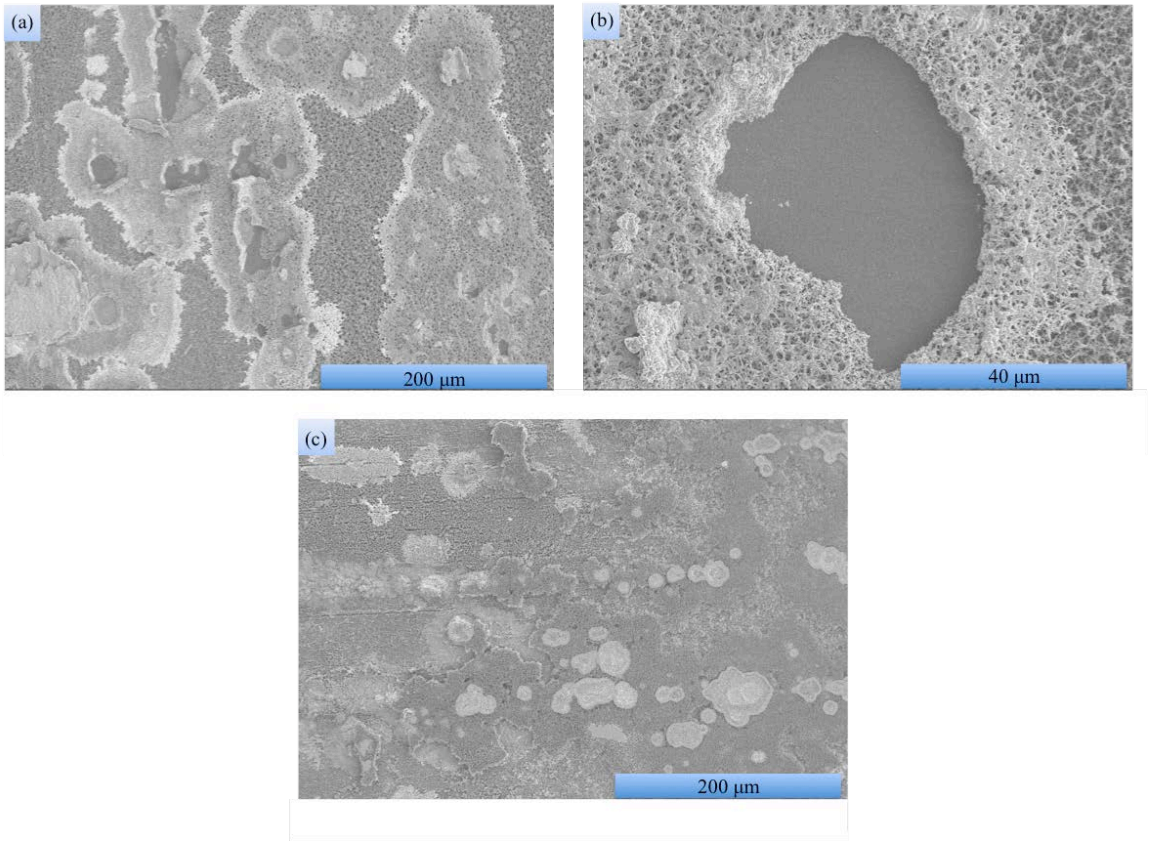

Figure 4.5. FESEM images of Si/CNT/CNT/Cu structure after detachment. (a) and (b) correspond to the Si substrate while (c) corresponds to the Cu foil.

The summary results in Table 4.1 indicate that reductions in bulk thermal resistance between decorated and undecorated TIMs occurred at the Si-CNT and CNT-Ag interfaces, with the latter having the largest reduction. These results are consistent with Ref. 31 in which the dominant thermal resistance was at the CNT 'free tip' interface as opposed to the growth substrate interface where the CNTs are well adhered. This significant reduction at the CNT-Ag interface can be attributed to two mechanisms, both comprising of nano- and mesoscopically sized contact regions as seen in Figures 4.4 and 4.5.

First, upon thermolysis, a strong bond between at the CNT/Ag was created such that greater contact area was achieved and we attribute the majority of improvement to the reduced phonon reflection at the CNT/Ag interface. In a previous study [33], the authors

concluded that the increase in contact area reduced phonon reflection at the boundary consisting of nano-sized contacts and provided enhanced pathways for heat conduction. Similarly, we postulate that the primary effect of Pd nanoparticles is to enlarge individual contact points both at the CNT/CNT and CNT/substrate interfaces. In a broader perspective relative to length scales, the ballistic component of constriction resistance that dominates its diffusive counterpart [41] would be more influential in an unbonded structure that primarily consists of many nano-sized contact points as opposed to a Pd bonded structure in which the aggregated effect of Pd nanoparticles gives rise to more mesoscopically sized contact regions.

Secondly, in previous work by Bhuvana and Kulkarni [70], thermal treatment of Pd hexadecanethiolate at 230°C in air produced metallic Pd nanowires with a specific electrical resistivity near 0.300 μΩm. Similarly, thermal treatment of structures in this study could have produced a metallic-like bond between CNT free ends and Ag foil via Pd nanoparticles in which a higher electron DOS near the Fermi level at the CNT/Ag interface was established. We also note that two types of contacts can exist at a CNT/metal interface: side- and end-contacted. Although the general orientation of the dense, CNT arrays in Figure 4.1 (a) is vertical, we assume that the majority of the contacts have side-contacted geometries upon compression into an interface. For non-bonded, side-contacted geometries, the contact quality depends on tunneling of electrons across an energy barrier created by van der Waals interaction at the metal/CNT interface [84] and since the physical separation between the metal and CNT is comparable to the carbon/metal bond length, tunneling depends on the chemical composition and configuration of electronic states at the surface [74]. If we consider Ag making uniform contact to graphene and the

transmission of an electron across the CNT/Ag interface, then in-plane wave vector conservation is enforced and for good coupling, the metal Fermi wave vector ($k_{f,Ag}$ = 1.2 $Å^{-1}$) should be comparable to that of graphene ($k_{f,graph.} = 4\pi/3a_o$ = 1.70 $Å^{-1}$) [84, 85]. Under weak coupling assumption (i.e., van der Waals interaction), calculated transmission probabilities at a uniform metal/graphene contact have been shown to exhibit a monotonic increase with contact length depending on CNT chirality [85]. Indeed, the transmission probabilities reported in Ref. 85 are quite small and therefore serve as a lower limit because the calculations were based on coupling strengths ~ $O(10^{-3})$ eV. Furthermore, if the coupling strength were increased via a metallic-like bond, then higher transmission probabilities could be achieved.

For larger diameter tubes, such as the CNTs in the present work, wave vector conservation becomes increasingly important [85]. However, such conservation principles can be relaxed when disorder (defects and impurities) are present [85]. Plasma-enhanced chemical vapor deposition (PECVD) grown CNTs in previous work have exhibited relatively high defects at the sidewalls due to plasma etching [83, 86, 87]. Thus, the additional disorder from sidewall defects caused by PECVD synthesis and Pd impurities at the CNT/Ag interface could relax wave vector conservation constraints. In this case, additional scattering from defects and Pd impurities could increase the transmission probability across the CNT/Ag interface, mediated by the presence of the Pd nanoparticles. However, for CNT/metal contacts as opposed to graphene/metal, it has been shown that coupling of electronic states between the CNT and metal will exist regardless of scattering from defects and impurities [88]. We expect similar effects to be operative for the two-

sided TIM configuration (Figure 4.2 (b)), with most of the improvement localized at the CNT/CNT interface.

4.4 Conclusions

In this study, CNT TIMs enhanced with Pd nanoparticles were fabricated using a previously developed method for CNT synthesis and a new process for bonding interfaces using Pd hexadecanethiolate. A transient photoacoustic technique was used to resolve bulk and component thermal interface resistances. All structures enhanced with Pd nanoparticles exhibited markedly improved thermal performance and thermal interface resistances that are comparable to previously reported values in the literature and that outperform most state-of-the-art TIMs used in industry. We attribute the majority of improved performance to the strong Pd weld that reduced phonon reflection at the interface by increasing the contact area between the CNT 'free-tips' and an opposing metal substrate. In addition, we considered utilizing electrons as a secondary energy carrier at the interface because of an increase in electron density of states at the CNT/Ag interface and offered discussion on the dependence that electron transmission has on wave vector conservation and disorder. With thermal stability across a wide temperature range, these structures are suitable for a variety of applications, particularly high-temperature electronics. Further investigation of energy and charge transport mechanisms at interfaces and Raman characterization of the CNT TIMs will elucidate the results of this study. Lastly, additional optimization related to coating and thermolysis of the Pd hexadecanethiolate solution on the CNT arrays could further reduce thermal interface resistance.

5. CNT TIMS IN ABNORMAL ENVIRONMENTS

5.1 Introduction

Systems in space are often exposed to higher levels of radiation, including charged particles and electromagnetic waves, than their terrestrial counterparts due to the lack of the atmosphere to serve as an absorbing medium. Particle radiation has been shown to drastically affect CNTs [88-91] by forming inter-tube bonds and cross-linking [91]. TIMs are shielded from these radiation sources which are easily absorbed by the external components of a spacecraft. On the other hand, high-energy electromagnetic waves such as gamma rays penetrate the exterior materials with minimal attenuation thus providing the potential to affect the CNT TIM.

Skakalova et al. [92] observed an increase in the Young's modulus and electrical conductivity of single-walled CNT (SWCNT) papers exposed to gamma-irradiation doses of 5, 17 and 50 Mrad. The maximum change was observed for a dose of 17 Mrad, however, the number of data points are too few to draw a concrete conclusion. Guo et al. [93] observed a dramatic increase in the I_D/I_G of the Raman spectrum of gamma-ray irradiated multi-walled CNTs (MWCNTs), which was attributed to the large presence of sp^3-hybridized carbon atoms. This is opposite the trend reported by Xu et al. [94], who noted an 8% decrease in I_D/I_G for MWCNTs irradiated to 20 Mrad in air, signaling improved graphitic order. However, when the gamma-ray dosing was conducted in epoxy chloropropane a 9% increase in I_D/I_G occurred. Miao et al. [95] investigated the

effects of dose rate and total dose on the breaking stress and Young's modulus of MWCNT yarns. Gamma-irradiation was found to increase both of these properties, however the majority of the changes occur rapidly at doses below 10 Mrad. Furthermore, dose rate was negligible on the measured results.

In this work, CNT TIMs are exposed to representative doses of gamma radiation in an effort to explore their capabilities in aerospace and deep space exploration applications. In a gamma cell, the CNT TIMs were irradiated at a rate of 250 rad/s to total doses of 50 Mrad and 100 Mrad. The I_D/I_G band ratio of the tubes was tracked using a Renishaw InVia Raman microscope, and the thermal interface resistances were monitored using a previously developed photoacoustic technique.

5.2 Experimental Setup

5.2.1 CNT TIM Fabrication and Characterization

Vertically aligned CNT arrays of low density were then synthesized in the MPCVD. The samples were imaged using a Hitachi field-emission scanning electron microscope (FESEM). Figure 5.1 contains images of the vertically aligned CNT arrays synthesized on Si. The array characteristics possessed average densities of 10^8-10^9 CNTs/mm^2, tube diameters of 30 nm, and heights near 10 μm.

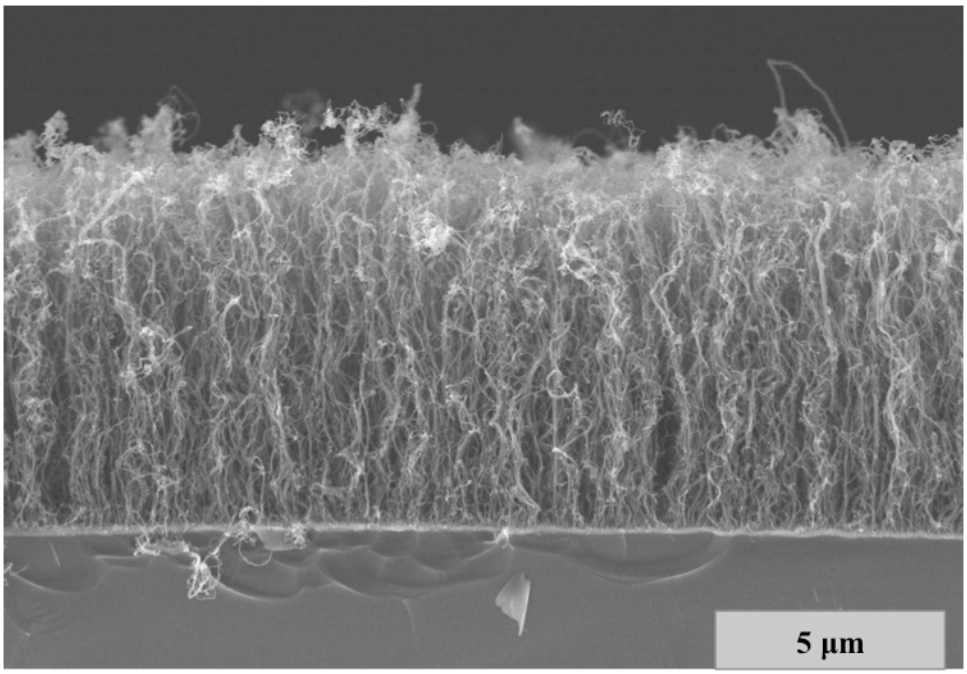

Figure 5.1. FESEM of CNT TIM grown on Si tab by MPCVD.

5.2.2 Radiation Dosing

Radiation aging of the samples was performed in a gamma cell shown in Figure 5.2 below. The TIM samples were separated into two bags containing equal numbers of test coupons. The bags were inserted vertically into the test cell together and since the gamma rays penetrated through the materials, no spacing between bags was necessary. The samples were exposed to a gamma ray dose rate of 250 rads/sec for approximately 55 hours to obtain a 50 Mrad dose on each bag. One bag containing three of six samples was removed from the gamma cell, while the second bag was reinserted to the gamma cell for an additional 55 hours to receive a total cumulative 100 Mrad dose of gamma irradiation.

Figure 5.2. Photograph of test samples in the gamma cell.

5.3 Results and Discussion

5.3.1 Raman Characterization

Raman spectra for every sample were collected at several locations on the sample surface. For all samples and locations the Raman spectra show the presence three distinct spectral features, as shown in Figures 5.3 (a) and (b): the D-peak at ~1360 cm^{-1}, G-peak at ~1585 cm^{-1} and a small peak at ~1620 cm^{-1}. To evaluate the impact of the radiation damage to the CNT films, the ratio of the intensities of the D and G peaks monitored before and after irradiation, as it is a useful indicator of long range order in carbon structures [71].

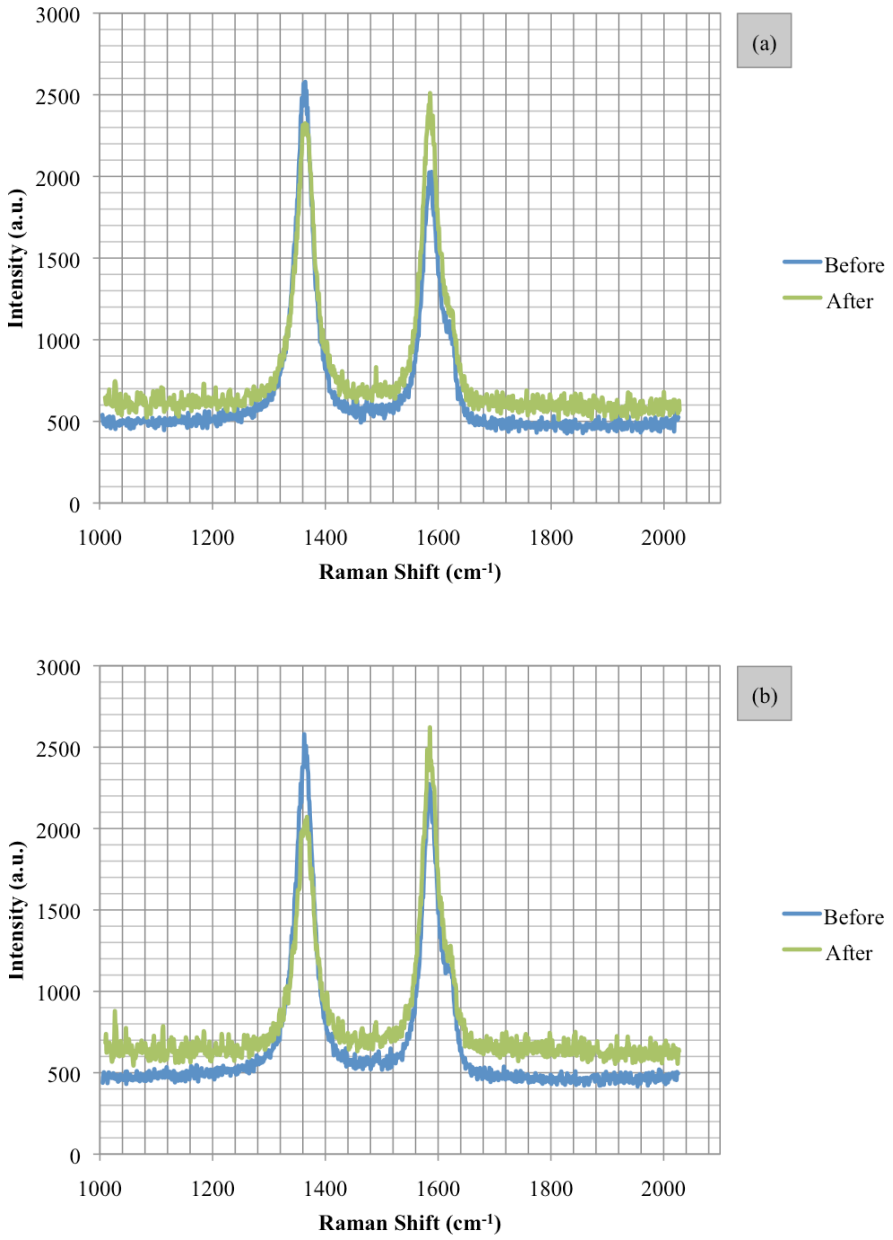

Figure 5.3. Raman spectra for CNT TIMs exposed to (a) 50 Mrad and (b) 100Mrad gamma radiation. Raman spectra before exposure also shown.

To determine the intensities of each peak, the acquired Raman spectra were analyzed by fitting them to a Breit-Wagner-Fano (BWF) spectral line shape [96]. This procedure removes uncertainty due to contributions from overlapping peaks in determining the peak

intensity. All samples before irradiation showed I_D/I_G ratios of ~1.3 which is higher than typical for MWCNTs [97] indicating significant presence of defects or edge effects resulting from the probing geometry used for the Raman measurement. After irradiation, samples subjected to a 50 Mrad dose exhibited a much lower I_D/I_G ratio of approximately 1.00; 100 Mrad samples showed a slightly lower ratio of approximately 0.95. The ratio of the D'-peak height to the G-peak height is also affected, but less markedly, changing from approximately 0.40 before irradiation to approximately 0.35 after irradiation for both doses. These changes result in a decrease of approximately 20% in the I_D/I_G ratios for both exposures and indicate that the I_D/I_G ratio is independent of gamma radiation dose, at least within the range of dosages tested. Figure 5.4 below summarizes these observations.

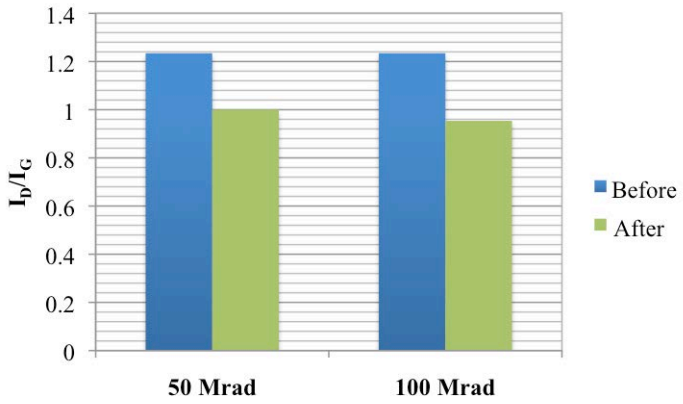

Figure 5.4. I_D to I_G band ratios for CNT TIMs before and after exposure to 50 and 100 Mrad.

The trends observed in Figure 5.4 resemble those reported by Xu et al. [94] but contradict the trends reported by Guo et al. [93]. Thus, sp-3 hybridization does not occur in the tube structures in this work, and the increase in quality is most likely due to improved graphitic order within the tube walls [94]. The scatter in the reported results could be attributed to the plethora of growth processes for CNT arrays that yield myriad tube structures.

5.3.2 Thermal Characterization

The thermal resistances for six CNT TIMs were measured by the PA technique at a contact pressure 134 kPa and room temperature. Each of the CNT TIMs was tested before and after exposure. Figure 5.5 contains a plot of the thermal resistance values for the six CNT TIMs before and after exposure. The resistance values in the figure are averaged across three samples for each of the dosages. Based on the measurement uncertainty, the error associated with the thermal resistances is 1 mm^2 K/W. The thermal results indicate that exposure to gamma radiation dosages between 50 and 100 Mrad has no effect on thermal performance. The slight decreases in thermal resistance after exposure to both 50 and 100 Mrad are most likely due to the sequential process of thermal testing the CNT TIMs rather than CNT interaction with gamma radiation. The thermal results are encouraging because the performance did not degrade after exposure, indicating that the CNT TIMs can withstand gamma-ray irradiation without adverse thermal effects, at least within the range of 50 and 100 Mrad dosages.

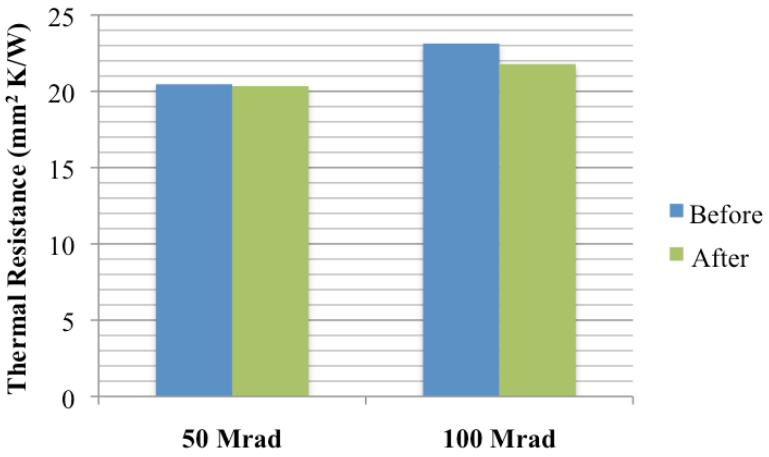

Figure 5.5. Thermal resistance for CNT TIMs before and after exposure to 50 and 100 Mrad. The opposing substrate was a 25 μm thick Ag foil. Thermal resistance values are averaged across three samples.

5.4 Conclusions

CNT-TIMs were exposed to gamma radiation in dosages of 50 and 100 Mrad. The quality of the CNTs, based on the I_D/I_G band ratio, was monitored by Raman spectroscopy and showed a moderate increase in the graphitic order of the CNT walls. Additionally, the thermal interface resistance was measured before and after gamma-ray irradiation using a transient photoacoustic method and while the exposure to such radiation has the potential to significantly affect CNT TIMs, no degradation in thermal performance was observed. Further studies such as thermal testing in a range of contact pressures coupled with nanoindentation experiments would help delineate the effects of gamma irradiation on the thermomechanical performance of CNTs.

Acknowledgment

Sandia National Laboratories is a multi-program laboratory managed and operated by Sandia Corporation, a wholly owned subsidiary of Lockheed Martin Corporation, for the U.S. Department of Energy's National Nuclear Security Administration under contract DE-AC04-94AL85000.

6. SOLDER BONDED AND PARAFFIN WAX INFILTRATED CNT TIMS

6.1 Introduction

As the size of electronic devices scales down and power densities increase, the need for innovative cooling solutions becomes more imperative. The prototypical architecture for electronic devices generally consists of a heat generating component such as a microprocessor and a heat spreader in tandem with a heat sink that transfers the heat to the ambient environment. Because of the modular assembly of the cooling architecture, thermal resistances at interfaces between components can significantly contribute to the total thermal budget. This thermal resistance, or thermal interface resistance is a consequence of the constriction of heat flow through small contact regions between adjoining components. When a TIM is inserted between the components, this thermal resistance is comprised of the thermal contact resistance at the adjoining interfaces as well as the intrinsic resistance of the TIM. This work considers the behavior of carbon nanotube array TIM materials of practical sizes and fabrication methods, with the aim of quantifying the effects of solder bonding and wax infiltration using a 1D reference bar technique.

Thermal pads, thermal greases, and metallic foils are commonly inserted between the components to alleviate the constriction of heat flow by conforming to the surface roughness of the components and filling the gaps between them, thus creating more

contact points and paths for heat transport [1]. Moreover, many applications require the TIM to accommodate a variety of stress conditions associated with either external vibrations or mismatches in the coefficient of thermal expansion between the components. However, a given TIM may best suited for only specific regime in the mechanical and thermal parameter space associated with a specific application. For example, thermal pads provide high mechanical conformability and effectively dampen low stress vibrations, yet possess low thermal conductivities on the order of 1 W/mK [2]. Thermal greases are commonly chosen for their ability to accommodate mechanical stresses during operation. Non-conductive thermal greases consist of a matrix of electrically insulating polymers and metal oxide filler materials with thermal conductivities less than 0.5 W/mK [3]. To increase the thermal conductivity to approximately 2 W/mK, metallic particles such as silver are substituted as the filler material [3]. When heated above their eutectic point, solder foils conform to surface asperities and offer the highest thermal performance with thermal conductivities above 20 W/mK [4]. However, when solidified, solder foils suffer from their inability to withstand mechanical stresses due to their rigidity.

In this work, MWCNT TIMs were sequentially solder bonded and infiltrated with paraffin wax while fixture in a one-dimensional, steady-state apparatus with copper-molybdenum bars as heat flux meters. The total thermal interface resistance was measured over the pressure range of 135 to 400 kPa. MWCNT CNT TIMs of varying heights were fabricated using microwave plasma CVD (MPCVD), which typically yield highly defective bamboo-like structures [5, 83, 86] with tortuous morphologies. Although the defect concentration of the CNT TIMs are not quantified in this work, we assume that heat conduction within the CNTs grown by this method is predominately diffusive, provided

that the most dominant phonon mean free path is much smaller than the number of defects per unit length with effective CNT heights on the order of 1 μm. In the diffusive regime, the effective thermal conductivity remains constant and the intrinsic thermal resistance scales linearly with CNT TIM height, which enables an analysis similar to Pal et al. [55] for estimating the effective thermal conductivity from thermal resistance and effective CNT TIM height measurements. The dependencies of thermal resistance on the compression of the CNT TIMs in unbonded and bonded states and the addition of paraffin wax into the interface material are considered. The CNT TIM height and volume fraction are also assessed to determine the contributions of contact resistance and intrinsic resistance to the total thermal resistance.

6.2 Experimental Setup

6.2.1 CNT TIM Fabrication and Characterization

MWCNT TIMs were fabricated using a microwave plasma chemical vapor deposition chamber [83] on both sides of 10 μm thick copper foil. Two groups of CNT TIMs were fabricated with different heights and volume fractions. The first group was grown using 100W of plasma generator power for 2.5 minutes and yielded CNT TIM heights between 5 – 7 μm. The second group was grown using 200W of plasma generator power for 2.5 minutes and yielded CNT TIM heights of approximately 17 μm. The additional plasma generator power increases the growth rate of the CNTs. CNT TIM heights were estimated by field emission scanning electron microscopy (FESEM) images from a cross-section view while the volume fractions were estimated by measuring the CNT mass before and

after synthesis using an Orion-Cahn C33 microbalance with a sensitivity of 1 µg. FESEM images of the CNT TIMs are shown below in Figure 6.1, and the total CNT TIM heights (side 1 and side 2) and volume fractions are plotted in Figure 6.3. The average CNT TIM heights range from approximately 5 to 18 µm and the mass densities range from approximately 0.05 to 0.13 g/cm^3 before compression.

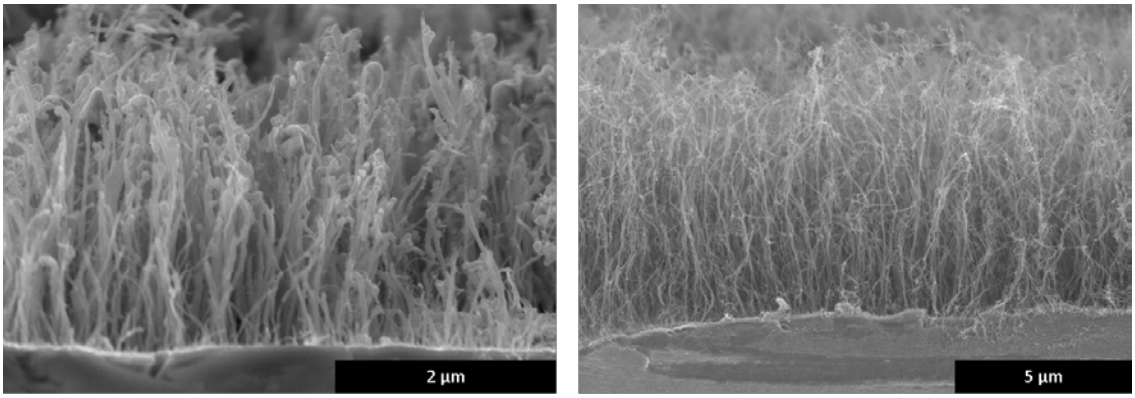

Figure 6.1. FESEM images of CNT TIMs after synthesis.

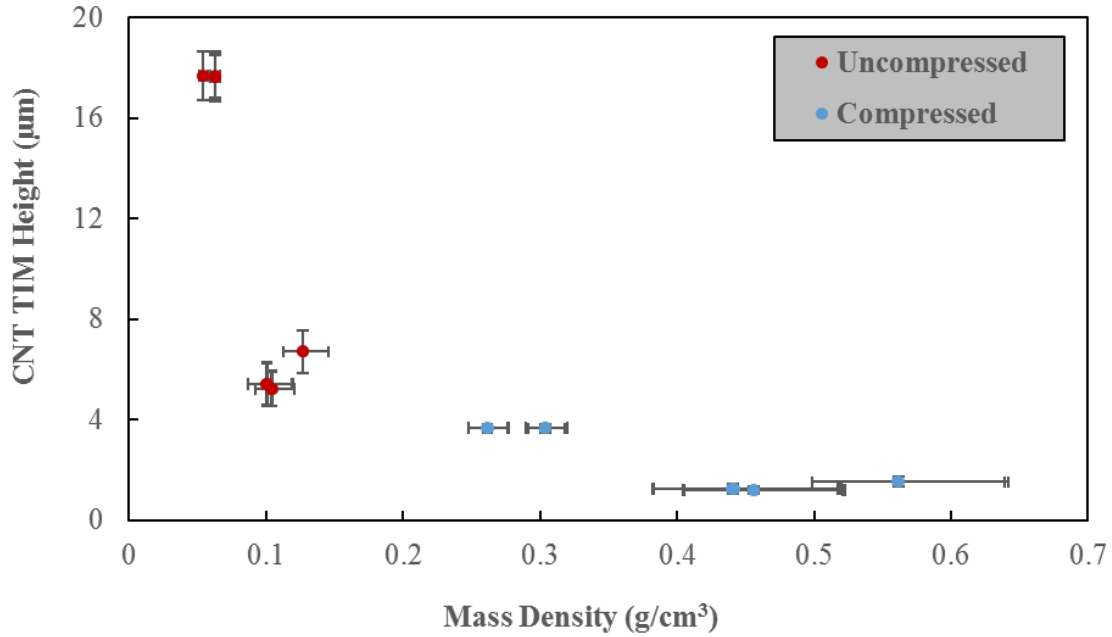

Figure 6.2. Average CNT TIM heights and mass density estimates.

6.3 Results and Discussion

6.3.1 Thermal Measurements

Figure 6.3 below shows 1D reference bar measurements of the total thermal resistance as a function of applied pressure for CNT TIMs that were unbonded and bonded with solder foils to the CuMo heat flux meters. Thermal resistance values are also shown for bare 10 µm thick, Cu foil for reference. The most apparent distinction between the unbonded and bonded states is embedded in the dependence of thermal resistance on the applied pressure. In the unbonded state, the thermal resistance values decrease nonlinearly with increased pressure and are expected to approach an asymptotic value at pressures much greater than 400 kPa.

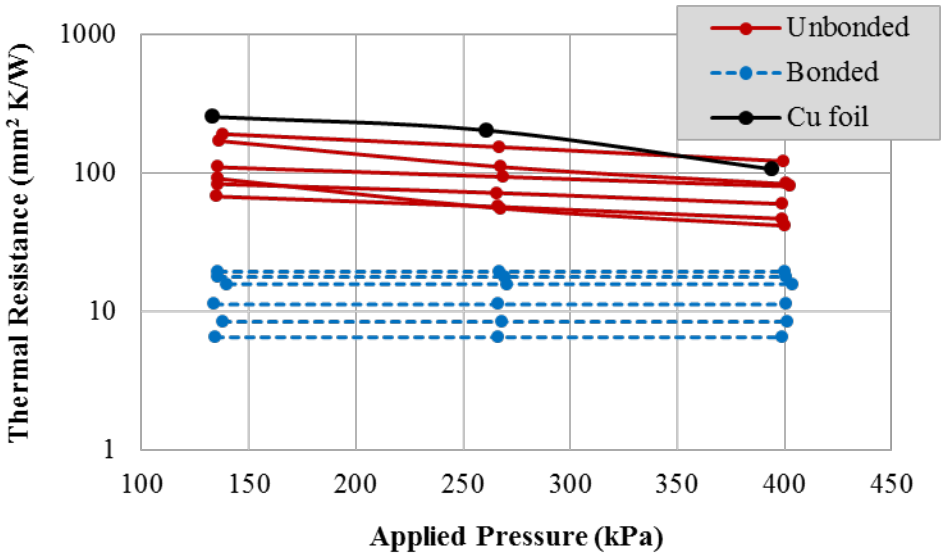

Figure 6.3. Thermal resistance values measured by 1D reference bar technique for bare, 10 µm thick Cu foil as well as CNT TIMs on 10 µm thick Cu foil that were unbonded and bonded with solder foils to the CuMo heat flux meters.

Figures 6.4 and 6.5 below show the total thermal resistance plotted against CNT TIM height and volume fraction, respectively. Note that the thermal resistance values are representative of CNT TIMs that were initially bonded to the heat flux meters with solder foil and subsequently infiltrated with paraffin wax. The values for total thermal resistance, height, and volume fraction were taken at the highest applied pressure in order to minimize variations in alignment and sample to sample loading to the total thermal resistance. Figures 6.4 and 6.5, respectively indicate that the thermal resistance moderately correlates with the CNT TIM height and volume fraction. Figure 6.6 shows the probability density curves for the uncertainties associated with the measured thermal resistance and CNT TIM height. A linear fit to the data in Figure 6.4 was used to calculate the effective thermal conductivity of the CNT TIM and equivalent contact resistance (CNT TIM to heat flux meter)

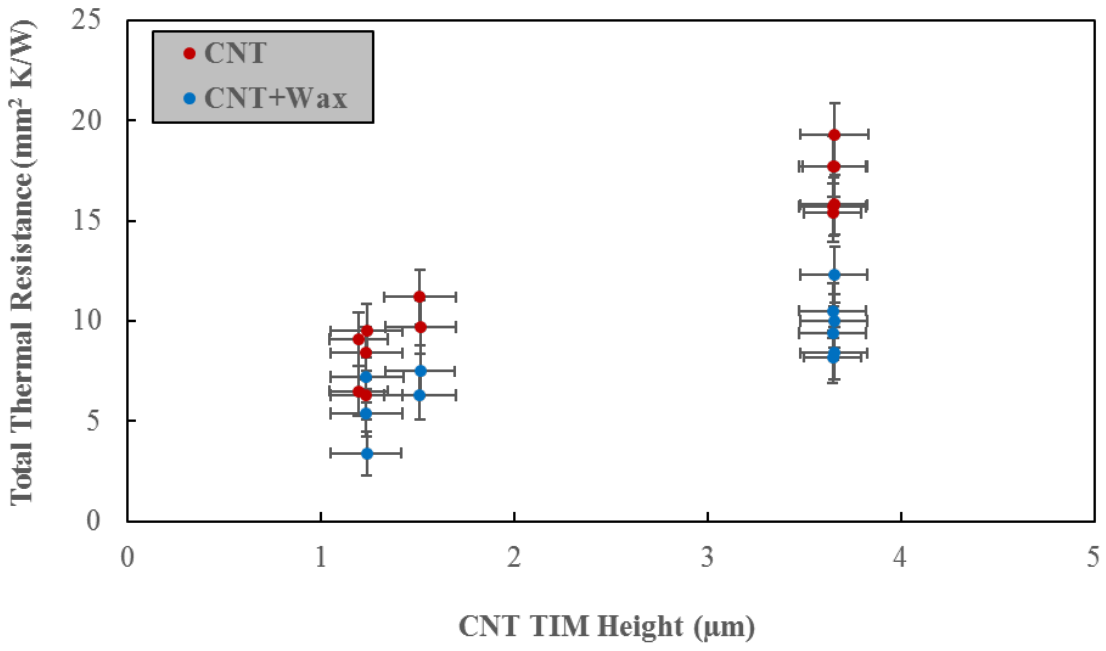

Figure 6.4. Total thermal resistance measured by 1D reference bar technique as a function of CNT TIM height with and without paraffin wax.

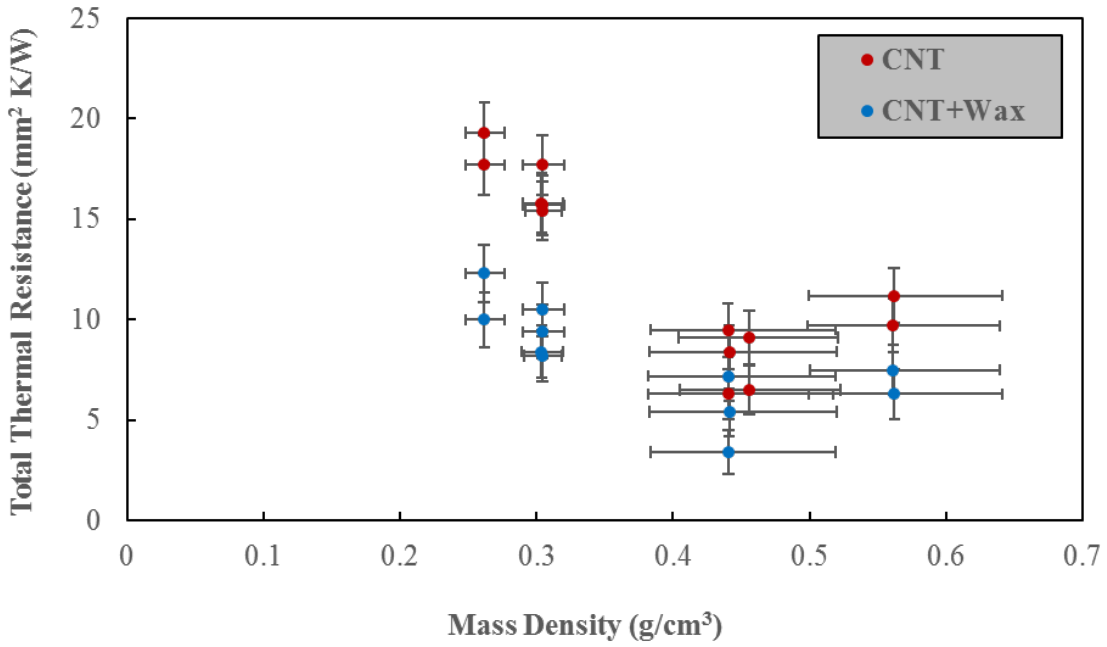

Figure 6.5. Total thermal resistance measured by 1D reference bar technique as a function of CNT TIM mass density with and without paraffin wax**.**

The total thermal resistance Equation (6.1) is comprised of series of thermal resistances: (i) contact between the CNT TIM and Cu foil growth substrate with a catalyst layer medium and (ii) contact between the CNT TIM and CuMo heat flux meters with a solder medium, and (iii) the bulk resistances of the CNT TIMs, Cu foil growth substrate, and solder layers. Note that due to the double-sided structure of the CNT TIM, $R_{contact}$ includes eight contact resistances (two for the growth substrate interface before and after the catalyst layer and two for the CNT to CuMo heat flux meter interface before and after the solder layer) while R_{bulk}, R_{solder}, R_{foil} include the bulk resistances of the CNT TIM, solder layers, and Cu foil respectively.

$$R_{total} = R_{bulk} + R_{contact} + R_{solder} + R_{foil} \tag{6.1}$$

Assuming a linear relationship approximately fits the data in Figure R2, Equation (6.1) can be rewritten as

$$R_{total} - R_{solder} - R_{foil} = mh + C \tag{6.2}$$

where the slope, *m*, represents the change in the bulk resistance of the stack with CNT TIM height, *h*, as shown below in Equation (6.3.

$$m = \frac{dR_{bulk}}{dh} \tag{6.3}$$

If the contact resistances and bulk resistances of the solder and Cu foil are assumed to be independent of the CNT TIM height, then the contact resistances as well as the bulk resistances of the solder and Cu foil manifest themselves as a constant, or equivalent contact resistance, R_{eq}, determined by the thermal resistance as t → 0 and k_{eff} is the inverse of the slope as shown below in Eqs. 4 and 5

$$\mathrm{C} = R_{contact} = \mathrm{R}_{eq} \tag{6.4}$$

$$k_{eff} = \left(\frac{dR_{bulk}}{dh} \right)^{-1} \tag{6.5}$$

Therefore, Equation (6.2) can be rewritten as

$$R_{total} - R_{solder} - R_{foil} = \frac{h}{k_{eff}} + R_{eq} \tag{6.6}$$

The average uncertainty in measuring thermal resistance is 15% (see Figure 3.6 and Figure 6.6 (a)) and represents the 95% confidence interval associated with the measurement of temperature, thermocouple location, and data fitting. The uncertainty in estimating the average CNT TIM height is approximately 20% and the estimated CNT TIM heights are assumed to follow a normal distribution bounded by this uncertainty (Figure 6.6 (b)). A

bootstrapping method [98, 99] was implemented to determine the uncertainty of estimations effective thermal conductivity of the CNT TIMs and the equivalent contact resistance. The probability density functions of the effective thermal conductivity of the CNT TIMs and equivalent contact resistance with and without wax are shown below in Figure 6.7 (a) and (b), respectively.

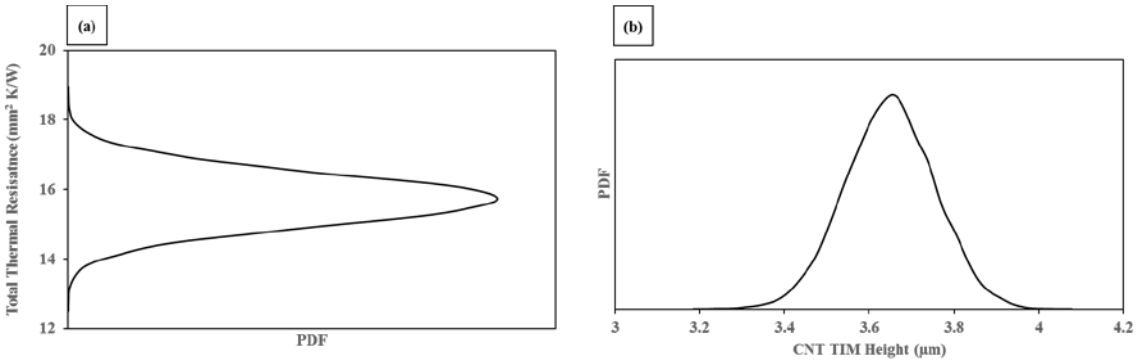

Figure 6.6. Probability density curves for uncertainties in (a) measured thermal resistance and (b) CNT TIM height.

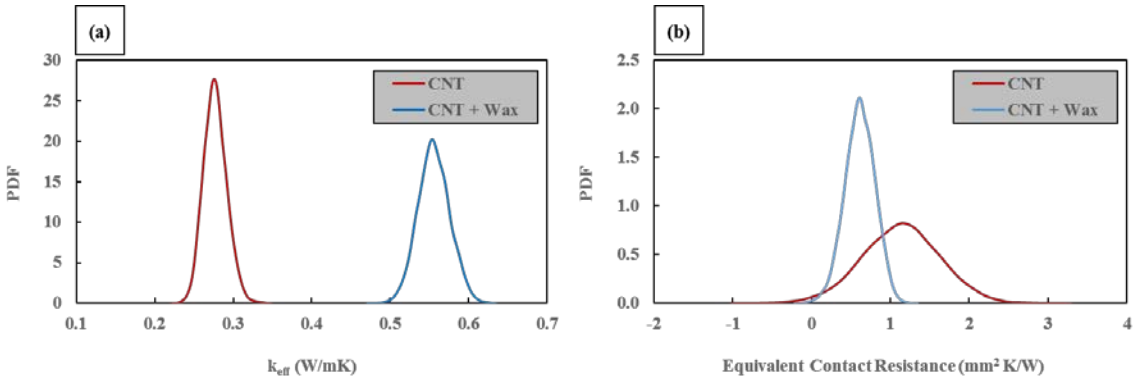

Figure 6.7. Probability density functions of the (a) effective thermal conductivity of the CNT TIMs with and without wax and (b) equivalent contact resistance with and without wax.

By carrying out the bootstrapping simulation using Equation (6.6), estimates for the effective thermal conductivities and the corresponding 95% confidence bounds are 0.28 (0.25, 0.30) and 0.55 (0.52, 0.59) W/mK without and with paraffin wax, respectively. These values reside on the lower end of the reported values for the effective thermal

conductivity of CNT TIMs [27, 32 - 34, 43 - 57]. The equivalent contact resistance is slightly reduced when paraffin wax is added as significant contact was already established during solder bonding. Note that the tail ends of the equivalent contact resistance distributions are negative and non-physical. The negative resistances are an artifact of the measurement uncertainty and lower limit of the 1DSS reference bar technique. This artificial feature would be eliminated if a TIM without CNTs was measured (i.e., zero CNT TIM height).

Using these estimates for the effective thermal conductivities of CNT TIMs without and with paraffin wax, the contributions of the bulk thermal resistance and equivalent contact resistance to the total thermal resistance are plotted in Figure 6.8 and 6.9 for the CNT TIMs, respectively. The equivalent contact resistance is independent of CNT TIM height and the variation is due to the differences in thermal conductivity of the solder foils. In contrast, due to the relatively low effective thermal conductivity of the CNT TIM, thermal transport through the CNT TIM plays a significant role in the thermal performance and scales linearly with height. The contribution of the CNT TIM to the total resistance is significantly mitigated when paraffin wax is added as the bulk resistance deceases below the equivalent contact resistance for the shorter CNT TIMs.

The thermal conductivity of paraffin wax used in this study was not directly measured nor used in the calculations of k_{eff}, but can be estimated from a simple equivalent thermal resistance consisting of two parallel components, one for thermal conduction through CNTs and another through the paraffin wax. Assuming no thermal transport between the CNTs and surrounding paraffin wax medium as well as the average k_{eff} of the CNT TIM without wax, the estimate of the thermal conductivity of paraffin wax is approximately

0.34 W/mK, which is within the upper range of values reported for different types of paraffin (0.15 – 0.36 W/mK [100]). Given that the CNT TIMs are compressed to a maximum volume fraction of 27%, we postulate that the predominant effect of paraffin wax is to fill the air gaps void of CNTs and provide a parallel pathway for thermal transport across the interface. A similar effect has been observed for CNT TIMs tested in vacuum and air in which air serves an analogous role to paraffin wax [101]. However, paraffin wax can also provide alternate pathways for thermal conduction for CNTs that do not make contact with the solder (CNT → wax → solder or CNT → wax → CNT) [102] and cannot be explicitly determined from the measurements.

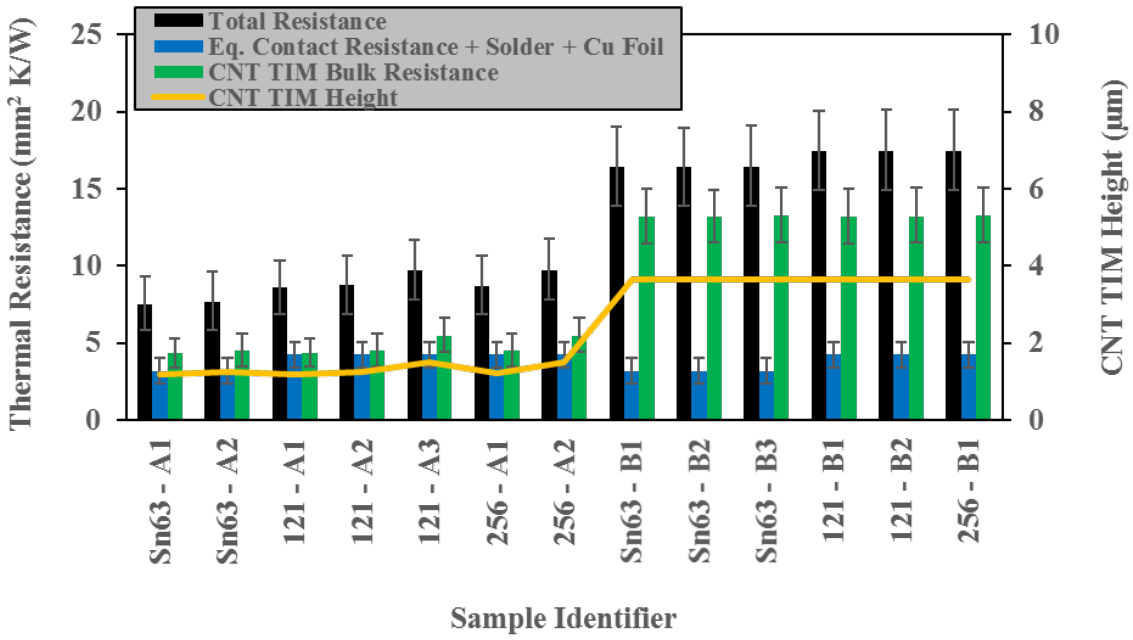

Figure 6.8. Contributions of the bulk thermal resistance, contact resistance, solder resistance, and Cu foil resistance relative to the total thermal resistance for CNT TIMs without wax. Samples identified with the letter A were grown using 100W plasma generator power while those identified with the letter B were grown using 200W plasma power. Sn63, 121, and 256 refer to the type of solder foil.

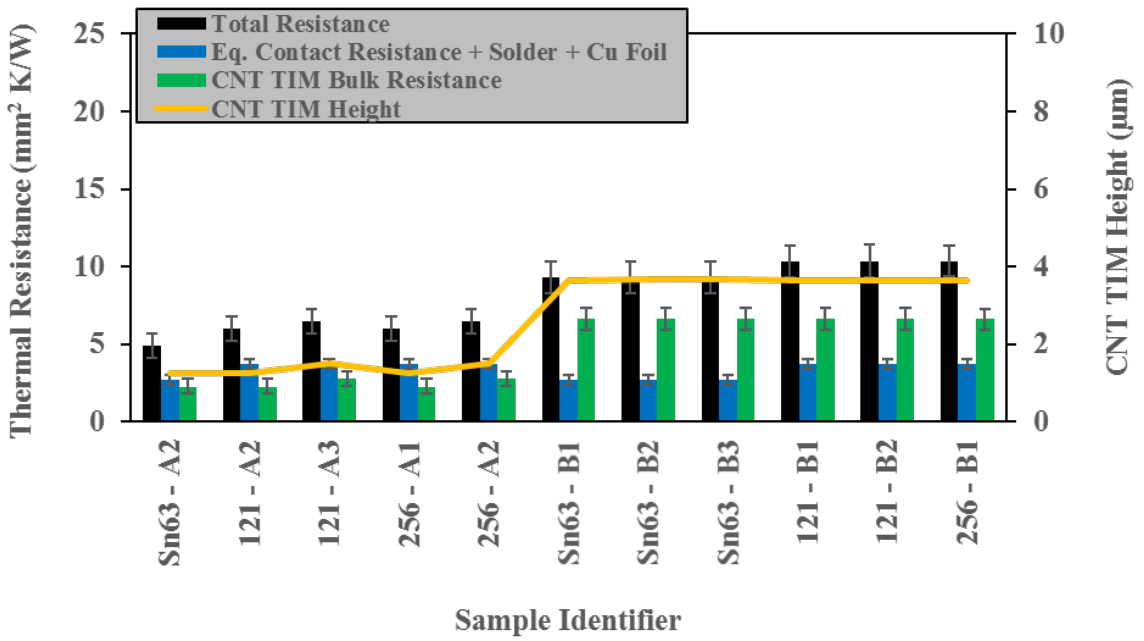

Figure 6.9. Contributions of the bulk thermal resistance, contact resistance, solder resistance, and Cu foil resistance relative to the total thermal resistance for CNT TIMs with wax. Samples identified with the letter A were grown using 100W plasma generator power while those identified with the letter B were grown using 200W plasma power. Sn63, 121, and 256 refer to the type of solder foil.

6.4 Conclusions

When the CNT TIMs are bonded to solder, a drastic reduction in thermal resistance relative to the unbonded state is achieved. In the bonded state, the thermal resistance was observed to be independent of pressure, indicating that the wettability of solder to the CNT TIMs is sufficient enough to maximize the contact area and minimize the contact resistance. While 1D reference bar technique employed in this work cannot directly resolve the component resistances (bulk and contact), an alternative method to extracting their contributions to the total thermal resistance was proposed. In a bonded state, the CNT TIMs exhibit moderate correlations to both CNT TIM height and volume fraction with shorter CNT TIMs having lower thermal resistance than taller CNT TIMs. A linear fit to

the thermal resistance and CNT TIM height data reveals a lower limit to the effective thermal conductivity of the compressed TIMs of approximately 0.28 W/mK without paraffin wax and 0.55 W/mK with paraffin wax. These values are on the lower end of reported values for standalone and composite CNT TIMs, which is attributed to the high degree of compaction that the CNT TIMs undergo during thermal testing within a pressure range of 135 and 400 kPa. The role of paraffin wax is expected to provide a parallel pathway to thermal transport and potentially mitigate CNT to CNT interactions.

7. THERMOMECHANICAL PERFORMANCE OF CNT TIMS

7.1 Introduction

The scope of this study involves CNT TIMs that can be used to facilitate the transfer of thermal energy from a heat-generating device to a thermal sink. TIMs of a variety of types are commonly used in the electronics cooling industry in which heat-generating devices such as microprocessors and thermal management components (e.g., heat spreaders) are commonly assembled in a modular fashion. This modular assembly causes thermal interface resistances (TIR) to manifest at mating surfaces, which are often mediated by inserting TIMs between the modular components. By applying a compressive load to the modular assembly, thermally conductive pathways are created across the interface. CNT TIMs have been viewed as potential alternatives to current commercially available TIMs [27 - 41] such as thermal pads and paste due to the intrinsically high thermal conductivity of individual, isolated CNTs and their ability to mechanically comply with the topography of opposing materials.

The outstanding mechanical and thermal properties of individual CNTs are a consequence of their high aspect ratio and cylindrical shape that is maintained by covalently bonded carbon atoms. The elastic modulus of an individual CNT has been measured to be on the order of teraPascals [8, 9] while the thermal conductivity of an individual CNT has been measured to be as high as 3000 W/mK [10, 11], making CNTs

strong candidates to strengthen composite materials and efficiently conduct thermal energy. In order to exploit these extraordinary properties for practical applications, CNTs are often mass-produced on a single substrate to match the length scales of larger components and devices. CNT arrays, bundles, forests, films, mats or CNTs are commonly produced in chemical vapor deposition processes. A feature of the aggregate structure is the formation of billions of neighboring high-aspect ratio CNTs that are nominally parallel and vertical, yet exhibit a tortuous microstructure. The underlying framework that governs the as-grown structure balances the strain energy due to ambient vibrations and mechanical constraints [12] with intra- and inter-tube van der Waals interactions [12 - 15].

The same mechanisms responsible for the microstructure of as-grown CNT TIMs also govern the state of its aggregate structure when subjected to external mechanical loading. In response to a compressive stress, the concentric shells of individual multi-walled CNTs bend and form buckles, ripples, or wrinkles in a coordinated manner [9, 14 - 18]. During this coordination, the intra-tube spacing between shells of the CNTs is predominantly preserved as van der Waals interactions oppose the compressive stresses induced from bending [9, 18]. As a result, the buckles, ripples, or wrinkles are most pronounced at the outermost tube and propagate to a lesser degree to the inner shells of the CNTs [9, 18]. The compressive response of CNT TIMs to uniaxial compression similarly incorporates the balance of bending stresses with van der Waals interactions, except at a much larger scale at which the entire structure collectively deforms in unison.

An analogy to the deformation of open-cell foams has been employed in prior research to describe the compressive behavior of CNT TIMs, with the stress-strain evolution divided into three distinct regions that represent linear elastic deformation, the onset of coordinated

buckling, and rapid densification of the CNT [12 - 14, 19 - 28]. A possible implication of the mechanical behavior is that heat conduction within the CNT may be coupled to changes in microstructure under a compressive stress. Indeed, heat conduction in CNT TIMs does not resemble a system of billions of pristine, individual, and isolated elements that independently conduct heat in parallel, each with its exceptional thermal conductivity [10, 12], but rather a coordinated network of conducting constituents [40, 56]. The coordinated network is mechanically and thermally constrained by van der Waals forces and exhibits much less desirable thermal properties, with steady state and transient measurements of the aggregate or effective thermal conductivity of CNT TIMs reported over a tremendously wide range of 0.3 – 265 W/mK [27, 32 - 34, 43 - 57].

Heat conduction in CNT TIMs is fundamentally complex, and the underlying transport mechanisms are difficult to resolve experimentally with high fidelity. The complexities are embedded in extracting the phonon transport mechanisms that affect heat conduction within individual CNTs, the interactions between adjacent CNTs, and the transmission of heat carriers between CNTs and dissimilar materials. The structural condition of CNTs (defects and quality) can dictate the thermal conductivity of individual CNTs [58]. The mass density, alignment, and waviness of the CNT microstructure can dictate the quantity and sizes of CNT-to-CNT contacts and ultimately the CNT-to-CNT contact conductance through van der Waals interactions. For bare interfaces (i.e., without a TIM), conduction through the gaseous medium can play a significant role in thermal transport across the interface, particularly at low contact pressures for which the solid-solid contact area is small and when the surface profiles of the opposing materials produce a gap distance (0.1-10 μm) that is comparable to the mean free path of gas molecules (0.064 μm for air) [1].

In addition to the gap distance, heat transport by this mechanism also depends on the thermal conductivity of the gas as well as the efficacy of energy transfer between the gas molecules and surface of the solid [46]. For CNT TIMs, conduction through the gaseous voids between CNTs can serve as a parallel transport mechanism for CNT CNTs of low mass density and short heights [101].

In this study, the thermomechanical performance of CNT TIMs under uniaxial compression is evaluated by measuring the bulk TIR (contact and bulk resistances) between Ag foil and a Si substrate (on which the CNTs are grown) at different compressive loads. To fit within the framework of the measurements, the CNT TIM is considered to be a non-interacting composite layer consisting of CNTs and air with an effective thermal conductivity, with additional thermal contact resistances to the Ag foil and Si growth substrate. The complex and intricate thermal transport mechanisms associated with the layered system (Ag foil, CNT TIM CNT, and growth substrate) are not explicitly quantified or individually resolved, but rather lumped into the bulk and contact resistances resulting from the TIR measurements. Nanoindentation results are also reported on duplicate samples, as *in situ* monitoring of the mechanical behavior during thermal testing was not possible. The nanoindentation results serve to complement the TIR measurements in order to infer mechanical effects that correlate to thermal performance, particularly the changes in thermal resistance under uniaxial compressive loading.

7.2 Experimental Setup

7.2.1 MWCNT TIM Fabrication

MWCNT TIMs were fabricated in-house using a microwave plasma enhanced chemical vapor deposition chamber [83] on standard silicon substrates. By controlling the synthesis times, CNT TIMs of varying heights (3 to 50 μm) were produced. A set of companion CNT TIMs was also prepared for the corresponding nanoindentation measurements. The heights were estimated by field emission scanning electron microscopy (FESEM) images from a cross-section view while the mass densities were estimated by measuring the CNT mass before and after synthesis. The as-grown mass densities ranged between approximately 0.04 – 0.06 g/cm^3. Post-mortem FESEM images of short, moderately tall, and tall CNT TIMs are shown in Figure 7.1.

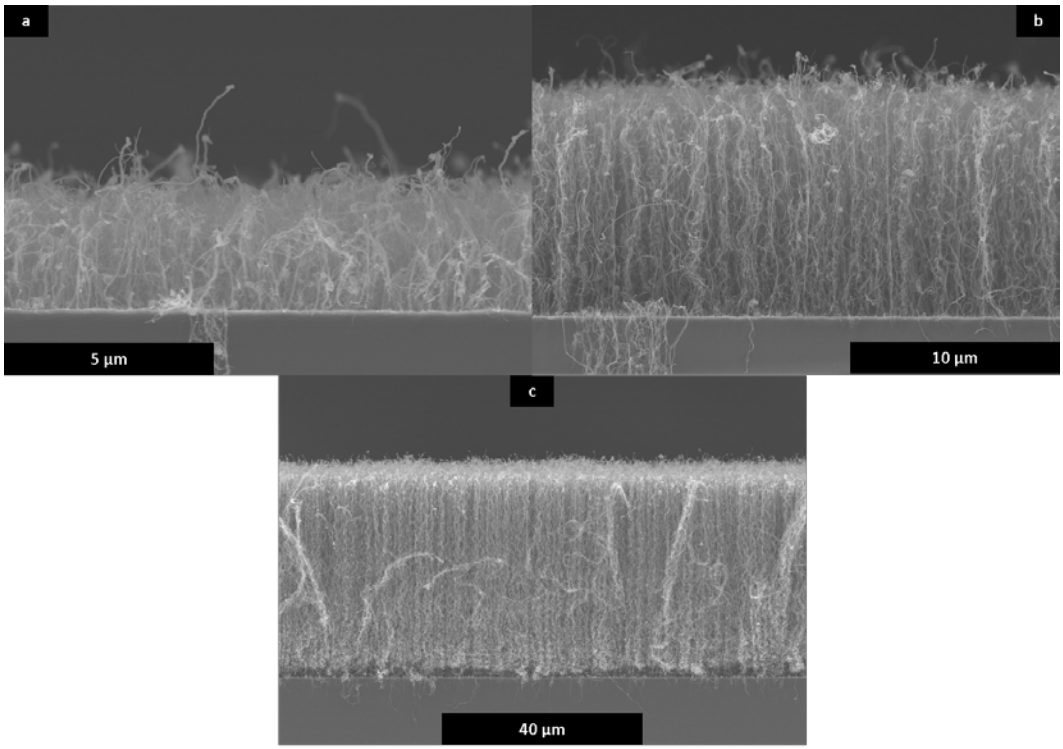

Figure 7.1. FESEM images of (a) 3.5, (b) 10, and (c) 41 µm tall CNT TIMs post thermal measurement.

Evidence of plastic deformation or buckling is difficult to observe in Figures 7.1 (a) and 7.1 (b) for the 3.5 and 10 µm tall CNT TIMs, but the 41 µm tall CNT TIM clearly displays these features as shown in Figure 7.2. The top of the CNT TIM appears to retain vertical alignment while a single buckling mode is present approximately at the midsection of the CNT TIM. Near the Si substrate, coordinated buckling of the CNTs and regions of localized strain can be observed.

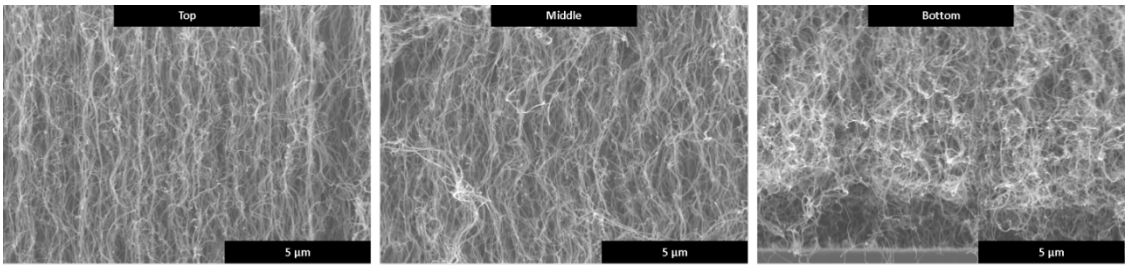

Figure 7.2. Magnified FESEM images of 41 µm tall CNT showing different morphologies spanning the height of the CNT TIM.

7.2.2 Photoacoustic Thermal Characterization

In electronics cooling applications, the microprocessor and thermal management components including the TIM are compressively preloaded to contact pressures between 15 - 60 kPa that can be subsequently amplified to a significantly higher pressure of 138 kPa in the event of a mechanical shock [103]. Additionally, depending on the absolute temperature of the components and relative differences in temperature and coefficients of thermal expansion during normal operation, stress tensors in other directions are likely present, but are not formally considered in this work. Within this pressure range, the thermal performance of CNT TIMs was evaluated using a transient PA technique. The thermal interface resistance between the Si substrate and opposing material (Ag foil) was directly measured, while the effective thermal conductivities and thermal contact resistances were inferred from a linear fit to thermal resistance measurements and CNT TIM height estimations. A more detailed review of the PA technique can be found in References 32, 59, and 65.

Figure 7.3 shows the experimental setup, and Figure 7.4 is a schematic of a typical multi-layered stack. During thermal testing the Ti-coated Ag foil was surrounded by a sealed acoustic cell that was pressurized with helium at four different pressures,

approximately 21, 41, 75, and 145 kPa, which sequentially compressed the CNT TIMs. The multi-layered stack was then heated over a range of frequencies by a 350 mW, modulated laser source. The thermal response of the multi-layered stack induces a transient temperature field in the gas that can be related to cell pressure. A microphone housed in the chamber wall measures the phase shift of the temperature-induced pressure response in the acoustic chamber, and the signal is then directed to a lock-in amplifier. Using the acoustic signal in conjunction with a model developed in prior work [32, 59, 65] that is based on a one-dimensional transient conduction analysis, thermal interface resistances were determined using a nonlinear least-square fitting algorithm. Similar to the work of Reference 59, the measurement technique was benchmarked against a 0.5 μm thick SiO_2 layer of known thermal conductivity (1.40 W/mK). By measuring the phase shift response of the SiO_2 layer in the frequency range of 1 to 6 kHz, the thermal conductivity was measured to be approximately 1.49 ± 0.17 W/mK.

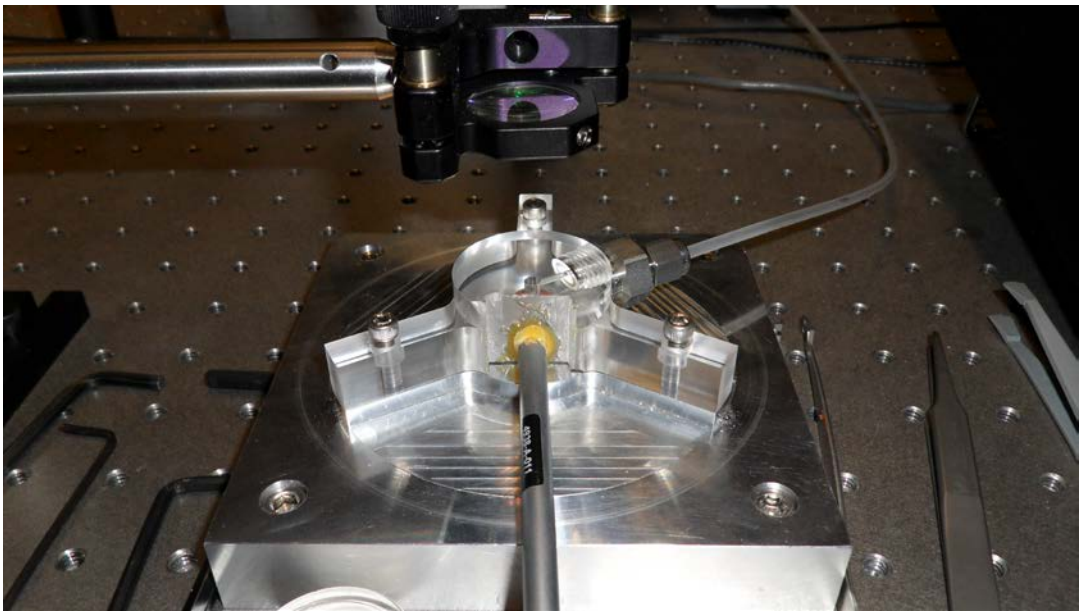

Figure 7.3. Experimental setup of photoacoustic technique and schematic of CNT TIMs in a configuration for thermal measurement in the PA technique.

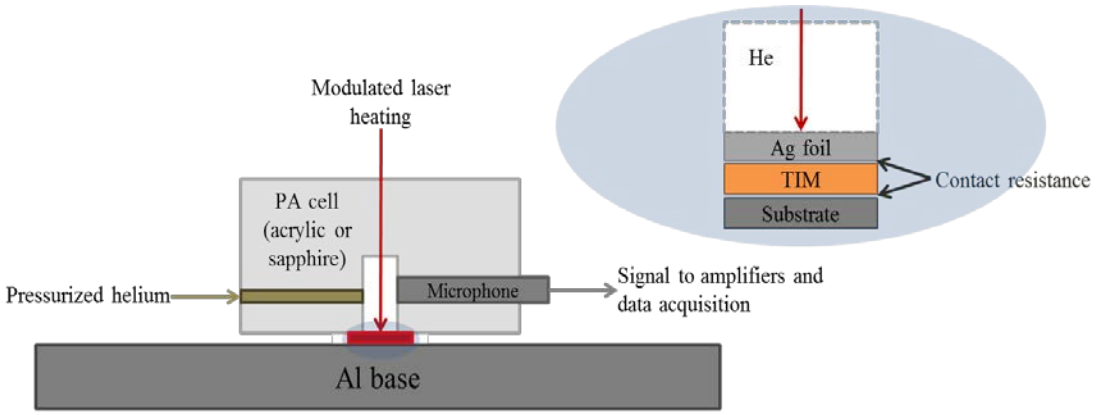

Figure 7.4. Schematic illustrating PA measurement of a multi-layered stack consisting of Ag foil, TIM, and substrate.

7.2.3 Nanoindentation Measurements

Indentation measurements on the 3.5, 10, and 41 μm tall CNT TIMs were conducted using a nanoindenter (Agilent G200) [21]. To mimic the compression of the CNT TIMs by the Ag foil in the PA technique, a 100 μm diamond flat punch was used during the indentation measurements. Two indentation methods were applied to each of the aforementioned CNT TIMs. Both methods involved indents at 9 different locations in a 3x3 grid pattern with a 500 μm spacing between indent locations. The first method consisted of a single load and unload segment at a constant strain rate of 0.1 s^{-1} [102]. The second method consisted of sequential cycles of load and unload segments in which the unloading stiffness as a function of stress was extracted from the unloading curve of each segment. The first method was used to estimate the CNT TIM height as a function of pressure for the PA measurements. The second method was used to infer deformation features and changes in stiffness that complement the PA measurements.

7.2.4 Uncertainty Quantification

Uncertainty in the thermal resistance measured by the PA technique arises from the variability in the phase shift signal acquired by the microphone as well as the uncertainty associated with loading the CNT TIM into the PA cell. The former has been shown to have an uncertainty of (±0.2°) [32]. The latter was determined by measuring the thermal resistance of the same CNT TIM at five different instances in which the Ag foil was moved out of contact with the CNT TIM and realigned for the next measurement. The uncertainty with the loading procedure was determined to be approximately (±1°) and is propagated through the analysis to determine the contact resistance and effective thermal conductivity. We find this approach to be appropriate because the uncertainty in the loading procedure is significantly greater than the uncertainty in the phase shift signal and serves as a better representation when comparing thermal resistance measurements of different CNT TIMs. This uncertainty was assumed to be normally distributed with a standard deviation of ± 1°, and the error bars in the proceeding figures represent the 95% confidence interval.

The CNT TIM height is frequently used in the following discussion, and the uncertainty was determined by the error associated with the image analysis employed to determine the initial and compressed CNT TIM heights. An example of the image analysis is shown in Figure 7.5.

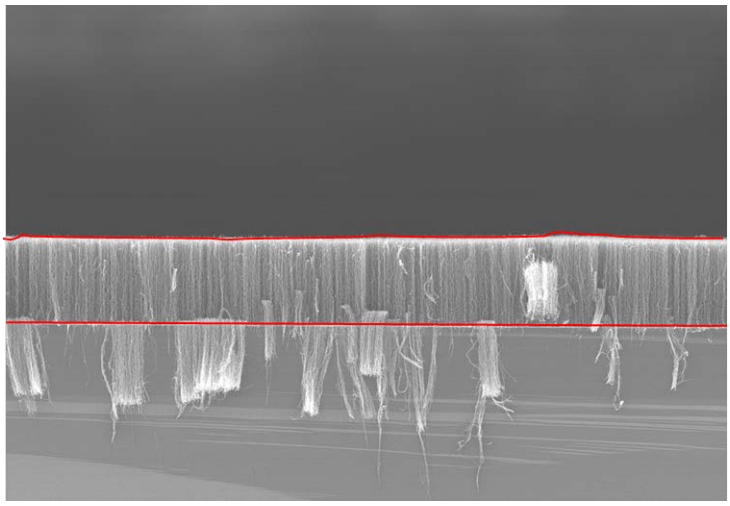

Figure 7.5. Image analysis performed on an SEM image to determine the initial and compressed CNT TIM height.

The bottom traced line in Figure 7.5 represents the interface between the Si substrate and CNTs while the top traced line is the contour defining the apparent roughness of the CNT tips. The CNT TIM height was assumed to be normally distributed with a mean and standard deviation determined from the distance between the two traced lines at each longitudinal slice of the SEM image. The width of the longitudinal slice was determined from the resolution of the image. We note that uncertainty can arise from the perspective in which the SEM image is captured (i.e., non-orthogonal projection). However, this uncertainty is difficult to quantify and is not included in the analysis.

The mass of CNTs used to calculate the mass density was assumed to follow a normal distribution with a standard deviation of ± 5 μg (microbalance specification data sheet reports ± 1 μg). The aforementioned uncertainties were propagated through the entire analysis using a boot-strapping method with ten thousand ‘virtual’ samples.

7.3 Results and Discussion

7.3.1 Mechanical Compression

The displacements into the CNT TIMs are plotted against the engineering stress applied by the indenter in Figures 7.6 (a) - (c) for the 3.5, 10, and 41 μm tall CNT TIMs, respectively. The unloading stiffness as a function of engineering stress is plotted in Figure 7.6 (d). The engineering stress is defined as the applied load sensed by the indenter divided by the cross-sectional area of the indenter. Note that throughout the proceeding sections, the engineering stress is assumed to be equivalent to the applied cell pressure in the PA measurement. For the taller CNT TIMs (10 and 41 μm), the displacement curves exhibit behaviors similar to open-cell foams [104, 105] in that three distinct regions exist: (i) a linear elastic region at stresses approximately less than 160 kPa, (ii) a flat plateau region at stresses approximately above 160 kPa and (iii) a densification region at higher stresses. Between the linear elastic and flat plateau regions, the stiffness of the 10 and 41 μm tall CNT TIMs increases until a stress of approximately 80 kPa is reached and then decreases as the CNT TIM begins to buckle in a coordinated manner [13, 19]. A monotonic increase in stiffness is observed for the 3.5 μm CNT TIM, which is likely due to substrate effects.

In the flat plateau region, the CNT TIM is significantly strained with a small increase in stress, while the densification region is indicative of significant increases in mass density as CNTs are compacted as well as stiffening effects from the Si substrate. The flat plateau and densification regions are representative of regimes in which significant microstructural changes in the aggregate CNT structure are occurring with plastic deformation observed during the unloading cycles. Plastic deformation is also apparent for the shortest, 3.5 μm

tall CNT TIM, but its displacement curve is noticeably different than those of taller CNT TIMs, likely due to substrate effects.

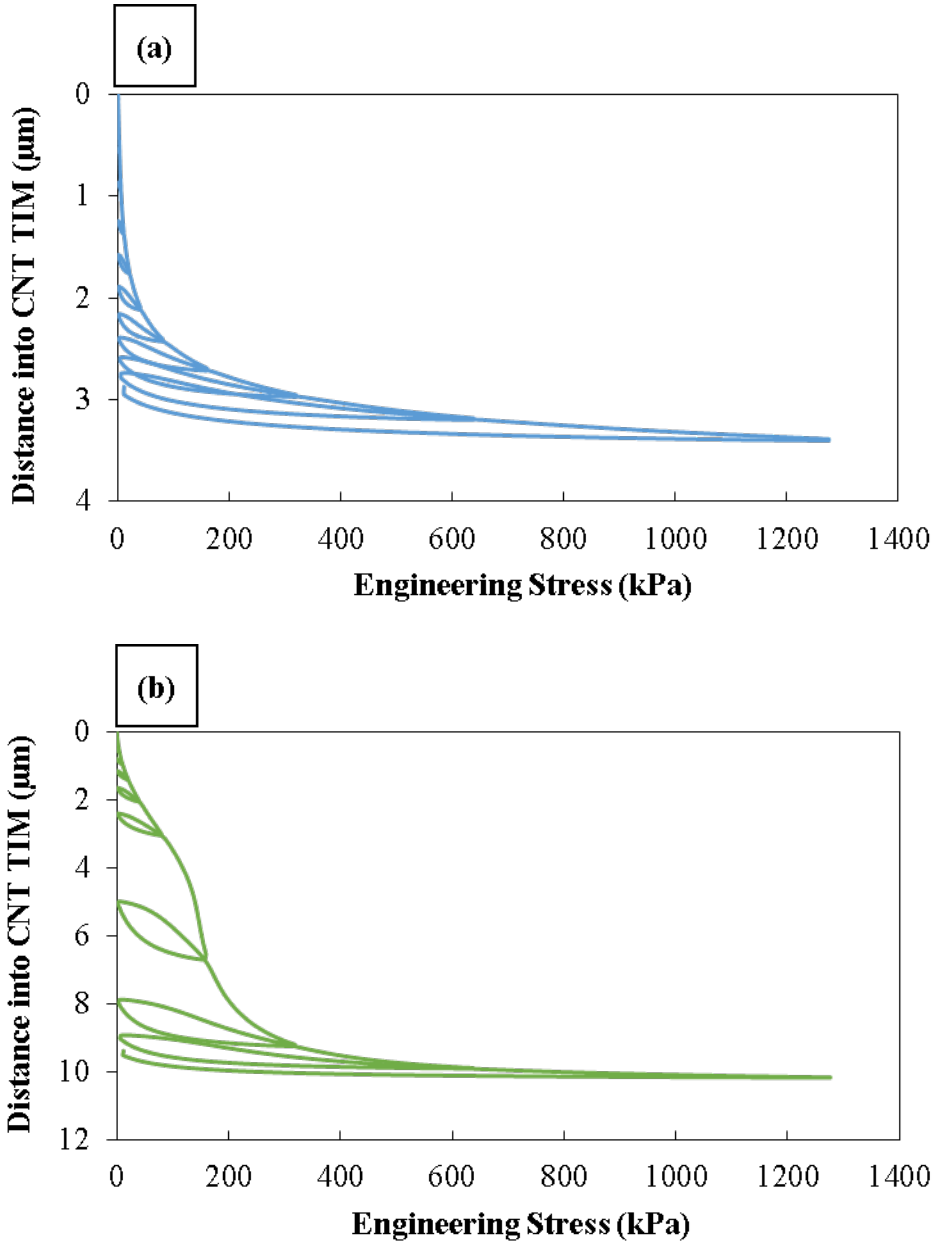

Figure 7.6. Distance into CNT TIM as a function of engineering stress for (a) 3.5 µm, (b), 10 µm, and (c) 41 µm. (d) Unloading stiffness as a function of engineering stress.

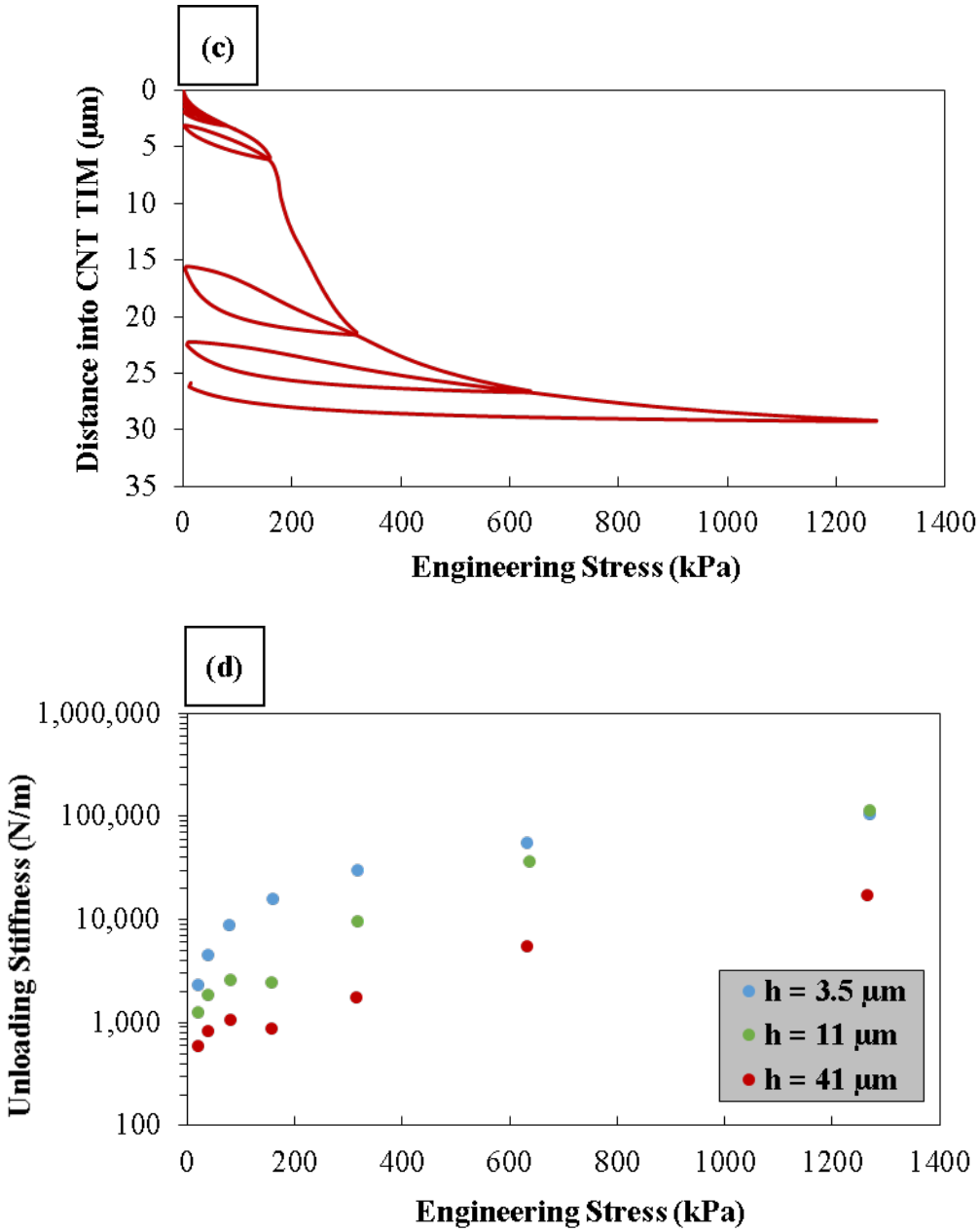

Figure 7.6. Continued.

7.3.2 Estimation of CNT TIM Height

Height estimates as functions of stress for the 3.5, 10, and 41 µm tall CNT TIMs were determined directly from nanoindentation measurements. Height estimates for CNT TIMs

that did not undergo nanoindentation measurements were determined with a calibration curve based on their as-grown heights and compression profiles of the 3.5, 10 and 41 μm tall CNT TIMs. As shown in Figure 7.7, a piecewise linear fit from the nanoindentation measurements was used to determine the change in CNT TIM height of the 3.5, 10, and 41 μm tall CNT TIMs at different stresses. In the absence of an indentation measurement, the piecewise linear fits allow for estimation of the change in height of other CNT TIMs based on their initial as-grown heights. For example, the height of a CNT TIM compressed to 145 kPa with an as-grown height of 15 μm can be determined from the dashed red line in Figure 7.7. Figure 7.8 shows the compressed heights of the 3.5, 10, and 41 μm tall CNT TIMs as functions of stress (solid lines) as well as the compressed heights of the other CNT TIMs that were not measured by nanoindentation. The circled points in Figure 7.8 correspond to the calibration curves in Figure 7.7 and represent the applied cell pressure at which the CNT TIMs were compressed during PA measurements.

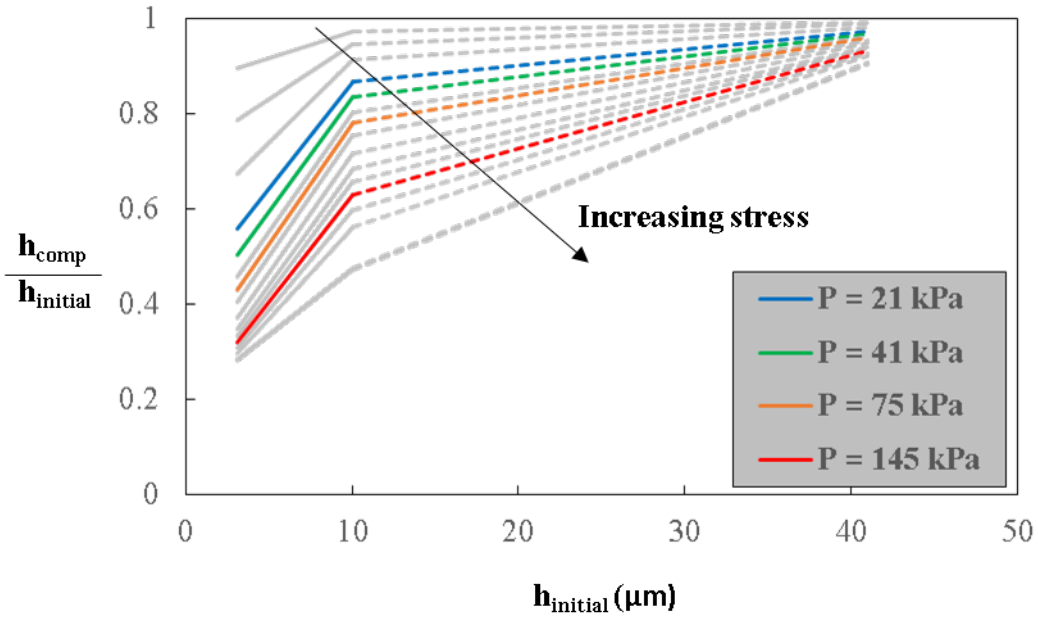

Figure 7.7. Piecewise linear fit at 21, 41, 76, and 145 kPa of the change in CNT TIM height relative to the initial CNT TIM height for the 3.5, 10, and 41 µm tall CNT TIMs measured by nanoindentation.

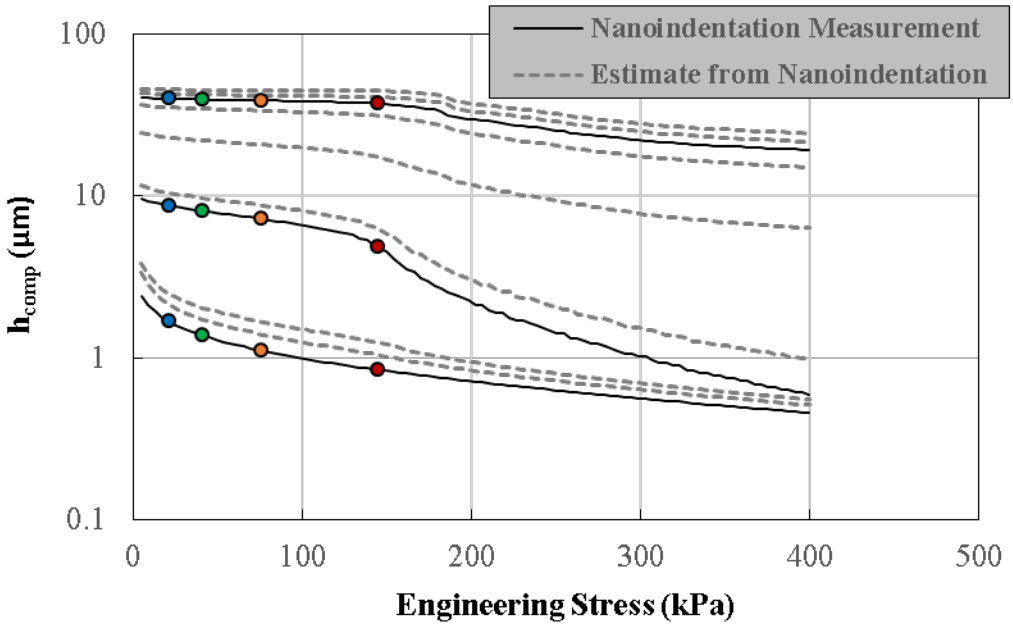

Figure 7.8. Compressed CNT TIM height as a function of engineering stress for the 3.5, 10, and 41 µm tall CNT TIMs measured by nanoindentation (solid lines) as well as estimates of the compressed CNT TIM heights for CNT TIMs not measured by nanoindentation (dashed lines).

7.3.3 Thermal Performance

Thermal resistance values obtained by the PA technique are shown in Figure 7.9 for as-grown CNT TIMs in three general height regimes: (i) < 10 μm (short CNT TIM), (ii) 10 - 30 μm (moderately tall CNT TIM) and (iii) greater than 30 μm (tall CNT TIM). The height regimes are defined in this manner in order to provide a categorical methodology to predict the thermal performance of CNT TIMs grown using our deposition process based on initial heights. For example, a CNT TIM with an as-grown height of 25 μm is expected have a thermal resistance profile similar to a 10 μm tall CNT TIM. An interface with a liquid metal as the TIM (GaInSn eutectic, k = 16.5 W/mK [106]) as well as an interface without a CNT TIM were also measured for comparison.

Thermal resistances were assessed at four pressures between 21 and 145 kPa with the maximum pressure limited by the acoustic hardware. Additionally, the thermal resistance values represent the resistance between the Ag foil and Si growth substrate with the CNT TIM separating these two layers. Note that the pressure corresponds to the gas pressure within the photoacoustic cell, which in turn induces a uniaxial compressive stress on the Ag foil and underlying CNT TIM. Thus, the thermal resistance without an applied cell pressure (0 kPa) represents the thermal resistance at a compressive load comprising the weight of foil and the photoacoustic cell (approximately 2 kPa).

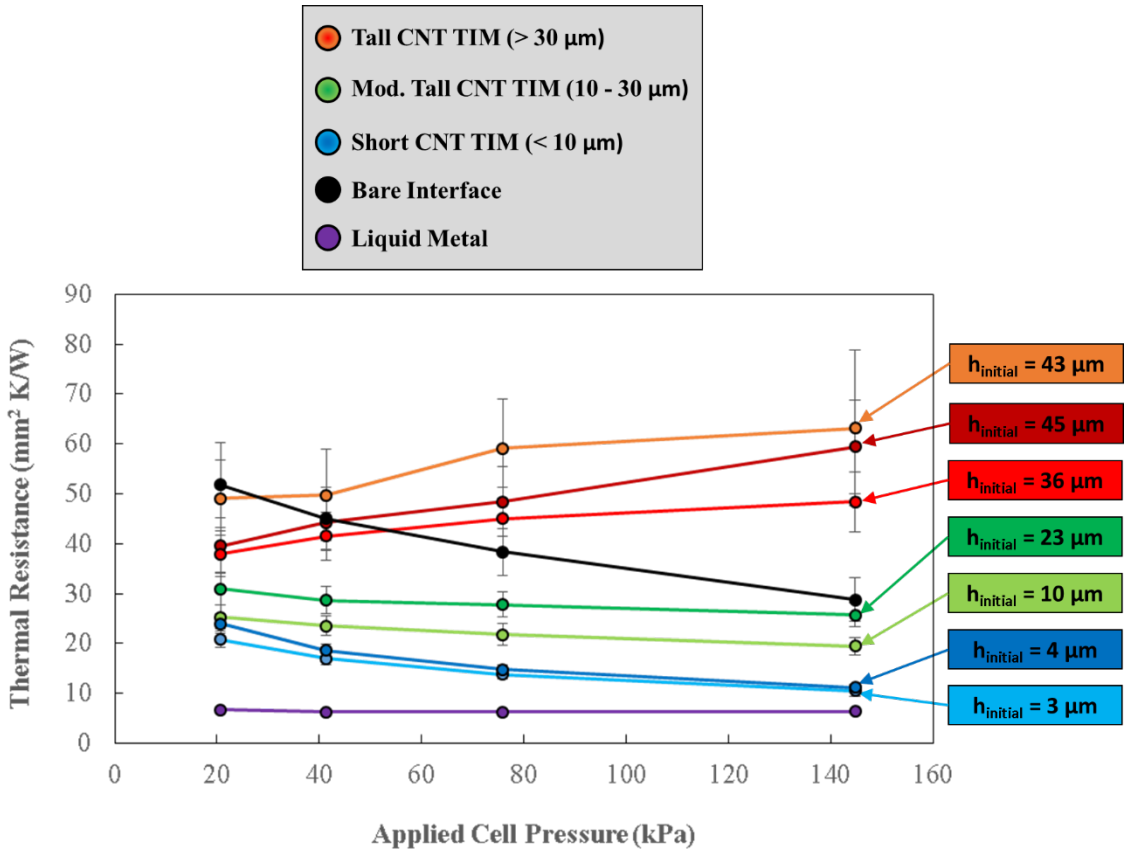

Figure 7.9. Thermal resistance measured by the photoacoustic technique as a function of applied cell pressure for CNT TIM heights ranging from 3 to 50 µm. Measurements of a bare interface (Ag foil to Si) and liquid metal are shown for comparison. The solid lines are displayed to guide the eye.

The GaInSn eutectic exhibits the lowest thermal resistance, and its thermal resistance also remains constant with pressure. The latter is an indication that the contact area with the opposing substrates is maximized once the opposing substrates (Ag foil and Si) come into contact with the GaInSn eutectic. Additionally, the interface without a CNT TIM has the most aggressive decrease in thermal resistance as the pressure increases, followed by short and moderately CNT TIMs. Across the pressure range at which the thermal measurements were conducted, the thermal performance of the CNT TIMs typically reside between two extremes: (i) an interface dominated by the contact resistance (i.e., a bare

interface) and (ii) a TIM that wets the opposing substrates well and conducts heat efficiently (i.e., liquid metal). The shortest CNT TIMs exhibit the lowest thermal resistance followed by the moderately tall and tallest CNT TIMs in ascending order. Within this pressure range, short and moderately tall CNT TIMs display a monotonic decrease in thermal resistance as pressure increases. Conversely, tall CNT TIMs exhibit a monotonic increase in thermal resistance as pressure increases, to the point that a bare interface thermally outperforms it at the highest pressure.

The thermal network of the CNT TIM as a function of the applied cell pressure is shown in Equation (7.1). The network is represented in a manner to tailor the foregoing analysis to the framework of the measured thermal resistance in Figure 7.9 and interface configuration in Figure 7.10. In this representation, phonon scattering mechanisms within individual CNTs induced by defects and kinks as well as intra- and inter-tube van der Waals interactions are inherently included in the bulk resistance. Additionally, since the CNT TIM is considered to be a non-interaction composite comprised of CNTs and air, the bulk resistance also incorporates heat conduction through the gaseous voids. Similarly, the transmission of heat carriers across solid-solid and solid-gas interfaces is implicitly included in the contact resistance.

$$R_{meas}\left(P\right) = R_{bulk} + R_{contact} = \frac{h_{comp}}{k_{eff}} + R_{Ag\ foil-CNT\ TIM} + R_{CNT\ TIM-Ag\ foil} \tag{7.1}$$

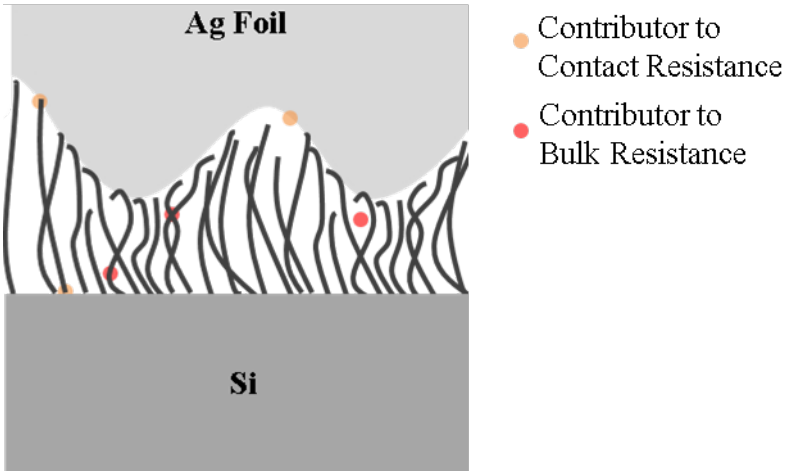

Figure 7.10. Schematic of interface showing contributors to contact and bulk resistances.

In Equation (7.1), R_{bulk} is the bulk resistance of the CNT TIM defined by the ratio of compressed CNT TIM height, h_{comp}, to the effective thermal conductivity of the CNT TIM, k_{eff}. $R_{contact}$ is the combined contact resistances of the CNT TIM with the Ag foil and Si growth substrate. Within this framework, the effective thermal conductivity of the CNT TIM at each pressure can be estimated by a linear fit of Equation (7.1) to the measured thermal resistances and CNT TIM height estimates as shown in Figure 7.11. The inverse slope represents the effective thermal conductivity of the CNT TIM, while the intercept with the vertical axis represents the combined contact resistance of the CNT TIM with the Ag foil and Si substrate.

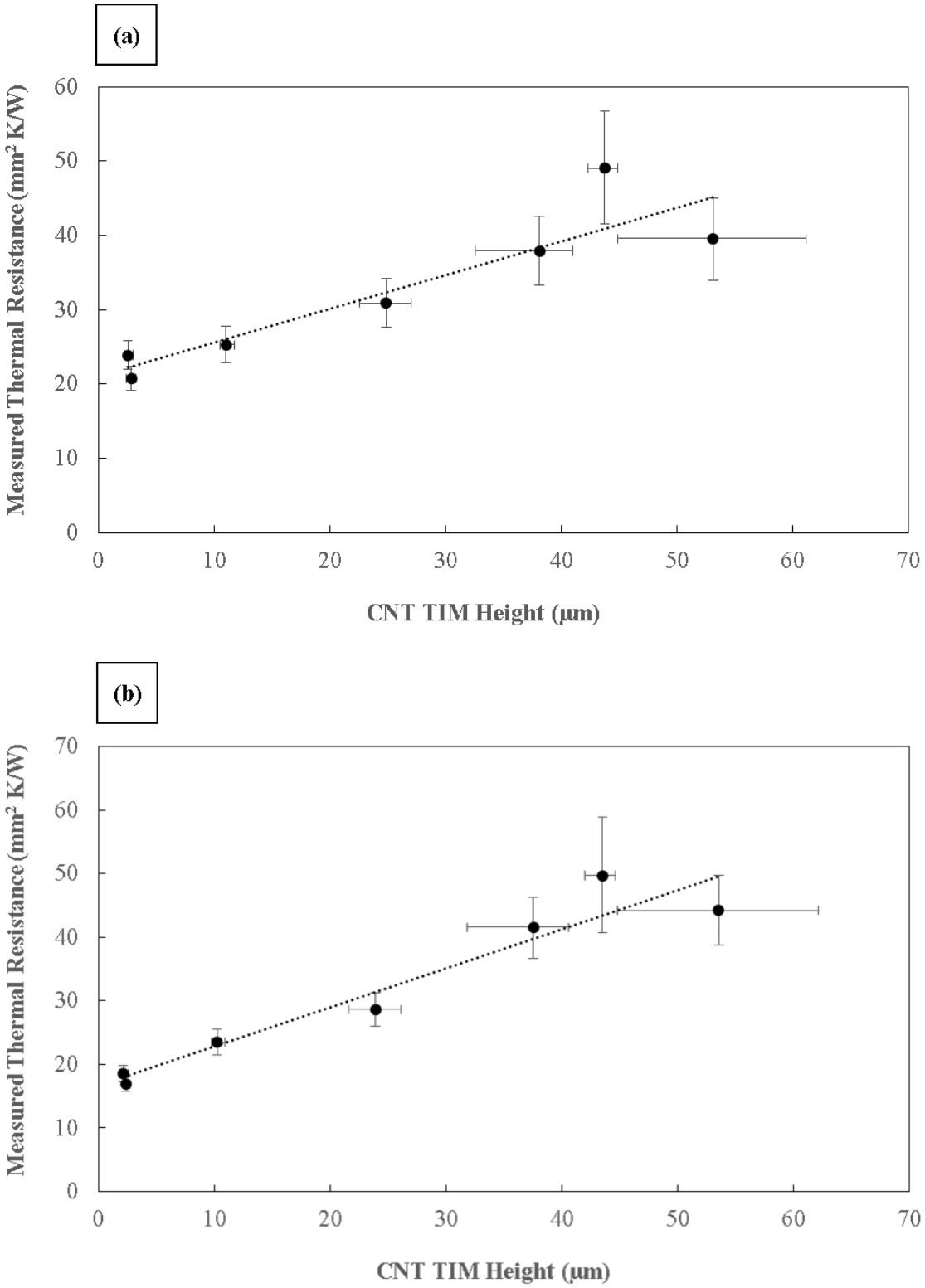

Figure 7.11. Total thermal resistance as a function of CNT TIM Height at (a) 21 kPa, (b) 41 kPa, (c) 76 kPa, and (d) 145 kPa. Inverse slope of the linear fit is the effective thermal conductivity and the intercept is the contact resistance.

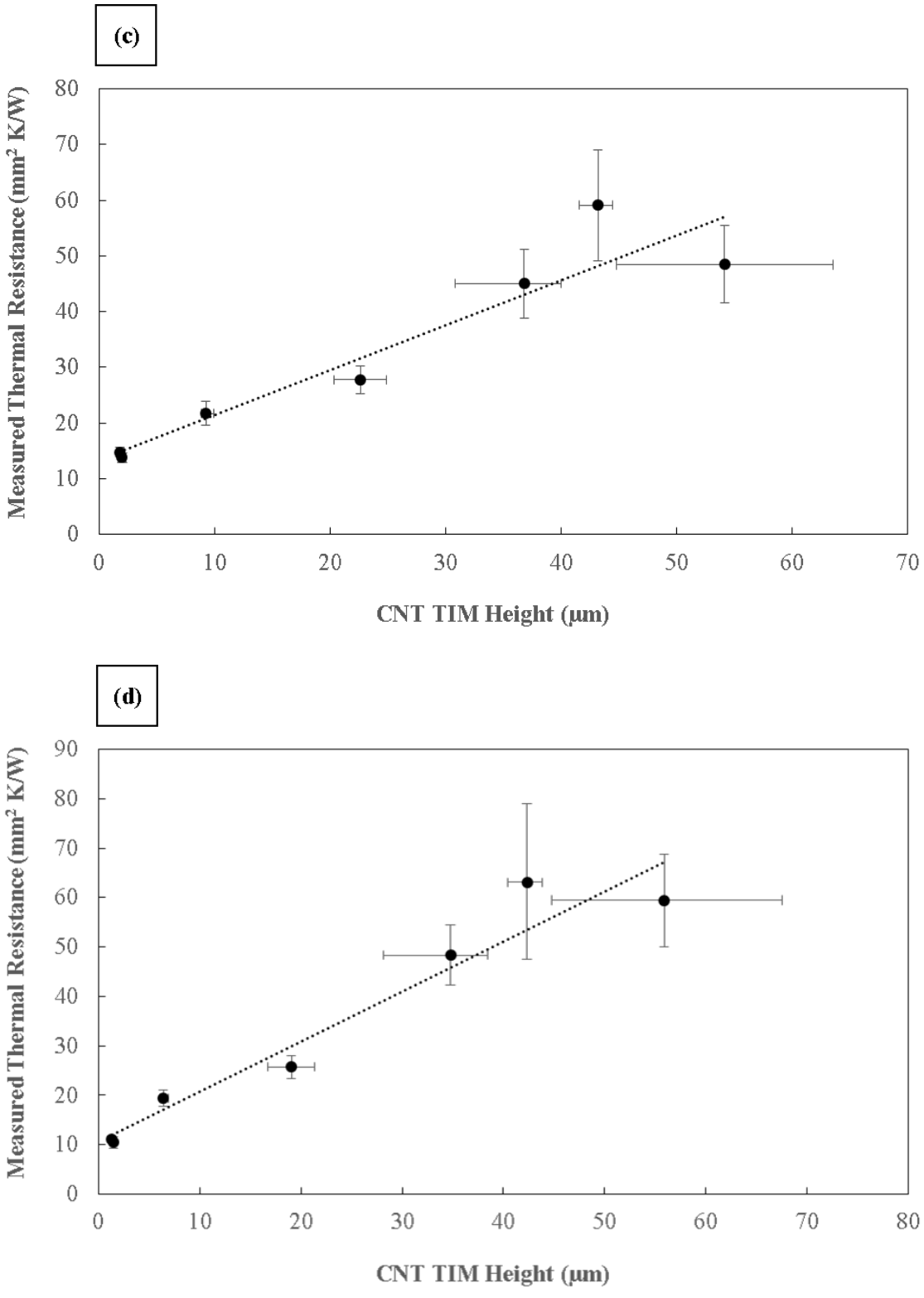

Figure 7.11. Continued.

An important implication of applying a linear fit to the data in Figure 7.11 is that the contact resistance and effective thermal conductivity are independent of CNT height. For CNT heights ranging from 5 to 150 μm, Taphouse et al. [107] observed a similar trend (i.e., higher thermal resistance with taller CNT TIMs) and qualitatively attributed the dependence of a contact-dominated thermal resistance on CNT height to non-uniformities in CNT growth rate and ultimately CNT surface roughness as observed through SEM imaging. The effect of CNT height on the effective thermal conductivity depends on the average distance a phonon travels before scattering (i.e., mean free path). If the dominant phonon mean free path is significantly less than the CNT height, then the effective thermal conductivity should not be affected by CNT height. Indeed, a study quantifying the surface roughness and dominant phonon mean free paths of these CNT TIMs would serve as a strong supplement to the underlying implications of applying a linear fit to the data in Figure 7.11, but such an analysis falls outside the scope of this work. Nonetheless, if CNT height significantly influenced the contact resistance and effective thermal conductivity, then the data in Figure 7.11 would exhibit nonlinear behavior, and at least within the range of CNT heights in this work, a linear fit seems to adequately describe the data.

A feature that can be inferred from Figure 7.11 is that the coefficient of determination (R^2 value) of the linear fit monotonically increases (Figure 7.12), suggesting that variations in the alignment of the CNT TIM with the Ag foil during the assembly procedure are mitigated as the pressure increases. The effective thermal conductivity of the CNT TIM and the combined contact resistances with the Ag foil and Si growth substrate as functions of pressure are shown in Figure 7.13.

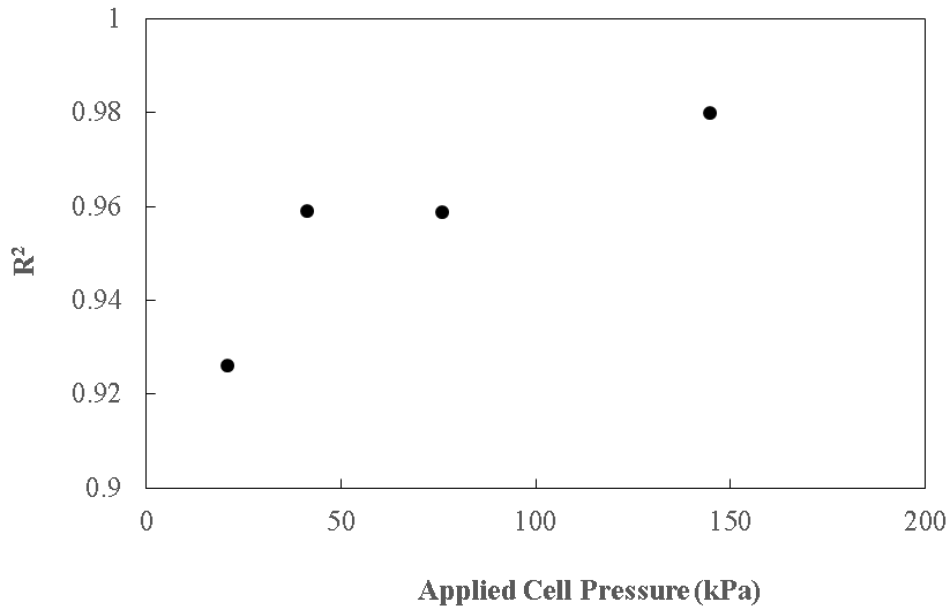

Figure 7.12. Coefficient of determination of linear fits to TIR and CNT TIM height measurements at different pressures.

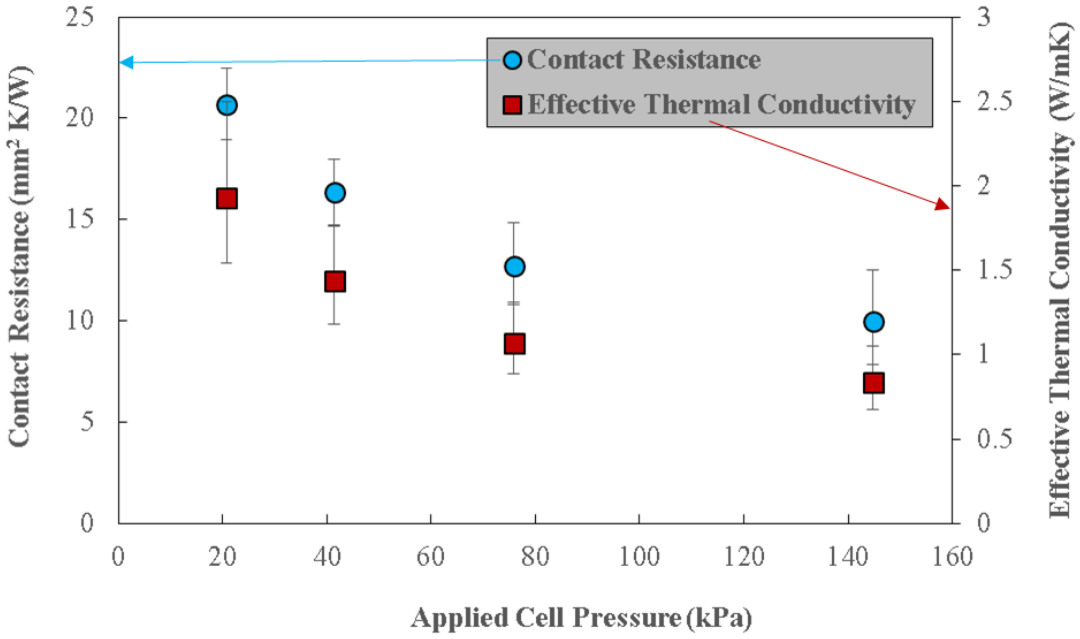

Figure 7.13. CNT TIM effective thermal conductivity and the combined contact resistance with Ag foil and Si growth substrate.

The contact resistances in Figure 7.13 are comparable to previously reported values for similar CNT TIMs grown on Si substrates that were measured by the photoacoustic technique [32 - 34]. The contact resistance between the CNT TIM and Ag foil is expected to dominate the combined contact resistance because phonon transmission at this interface depends on weak van der Waals interactions [41], whereas the CNTs are expected to covalently root into the catalyst layer on the Si growth substrate [108]. The effective thermal conductivities in Figure 7.13 reside on the lower end of the range of reported values [27, 32 - 34, 43 - 57] and correspond well with Bougher et al. [34] using the photoacoustic technique and Pal et al. [55] using similar analysis in this work. Bougher *et al.* treated the CNT TIM as a thermally capacitive layer in the photoacoustic model and employed multivariate regression to determine the effective thermal conductivity and contact resistances to the opposing substrates. In order to eliminate the uncertainties associated with density and heat capacity estimations, the CNT TIM was not included as a thermally capacitive medium in this work. Nonetheless, the agreement between the effective thermal conductivities resulting from these differing approaches is encouraging, considering the wide range of reported values [27, 32 - 34, 43 - 57].

With the contact resistances, effective thermal conductivities, and CNT TIM heights determined at the four pressures the thermal resistances of the CNT TIMs were measured, the contributions of the bulk and contact resistances can be compared. Figure 7.14 shows comparisons of the bulk and contact resistances to the total thermal resistance as a function of pressure for CNT TIMs with as-grown heights of 3, 10, 23, and 43 μm.

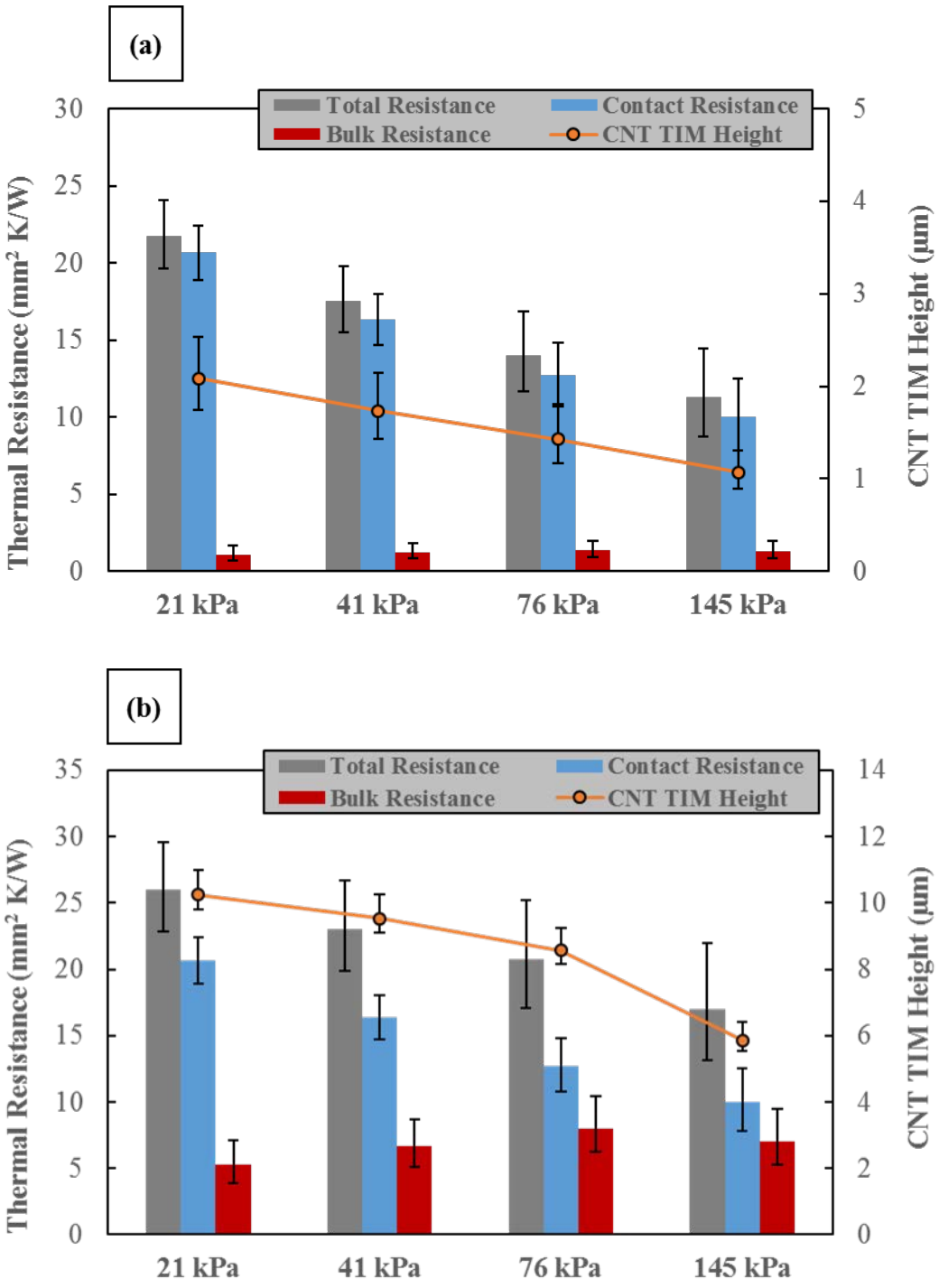

Figure 7.14. Comparison of the contributions of the bulk and contact resistance to the total thermal resistance as function of pressure for CNT TIMs with as-grown heights of (a) 3, (b) 10, (c) 23, and (d) 43 μm.

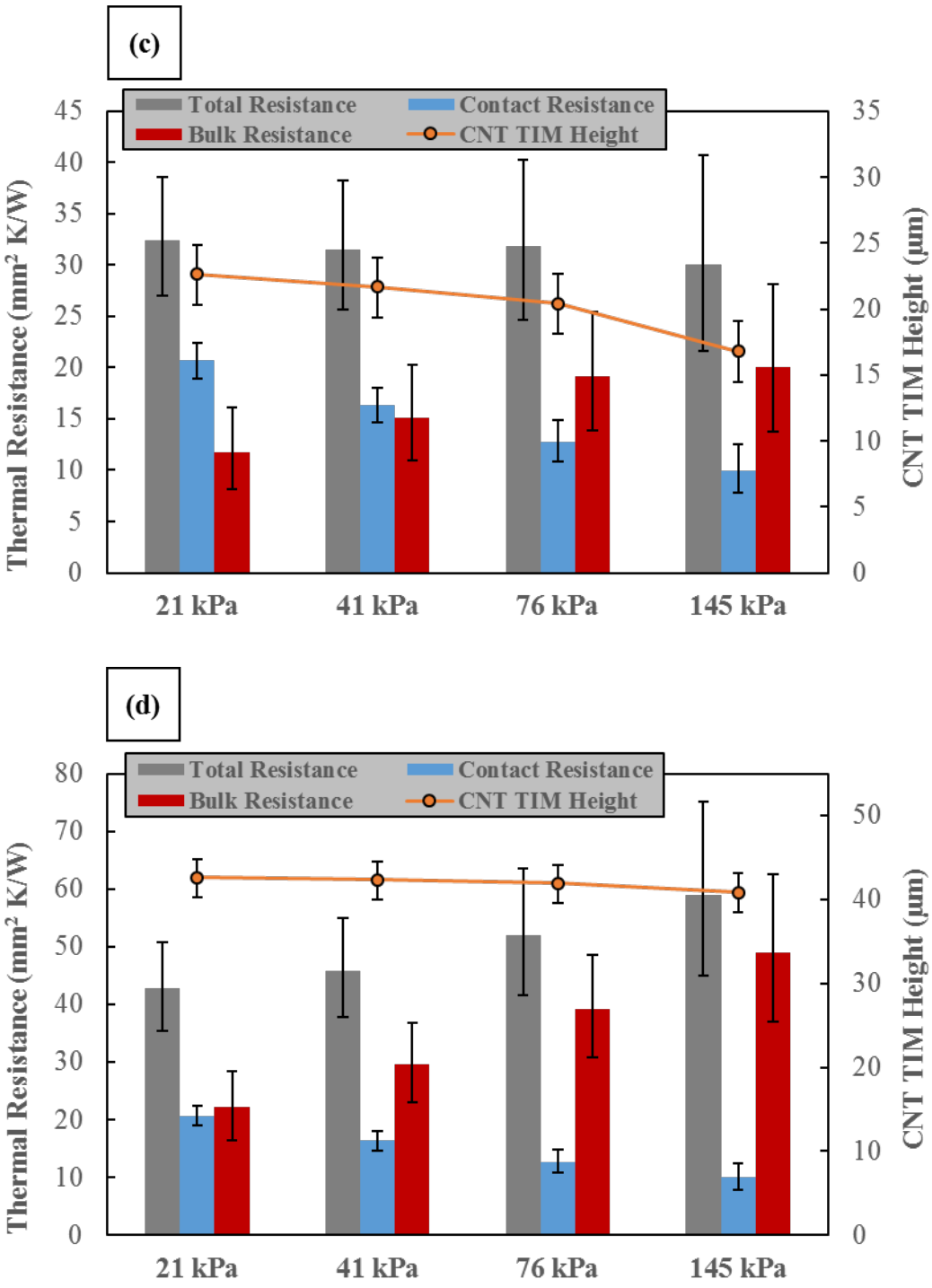

Figure 7.14. Continued.

For shortest CNT TIM (Figure 7.14a), the total thermal resistance is dominated by the contact made with the Ag foil as the bulk resistance is significantly lower than the contact

resistance, and the change in total thermal resistance with pressure is driven by the change in contact resistance. For the CNT TIM with an as-grown height of 10 μm (Figure 7.14b), the contact resistance remains the main contributor to total thermal resistance, but the bulk resistance is greater than that of the shortest CNT TIM. As a result, the decrease in total thermal resistance with pressure is less pronounced relative to the shortest CNT TIM. For the CNT TIMs with as-grown heights of 23 and 43 μm (Figures R7.14c and 7.14d), the bulk resistance is even more influential relative to the contact resistance and ultimately causes an increase in the total thermal resistance as pressure increases.

Within the range of pressures at which the PA measurements were performed, both the contact resistance to the opposing substrates and the effective thermal conductivity monotonically decrease as the CNT TIM compresses. The former is expected as the CNT tips elastically bend and the size of CNT to Ag foil contacts increases as the interface is compressed [41]. As the compression profile of the CNT TIM transitions from the linear elastic to buckling region, we postulate that stiffening due to CNT-to-CNT contacts and localized strain adversely affects thermal transport within the CNT TIM, causing the effective thermal conductivity to reduce.

Effective medium approximations are commonly employed to describe the effective thermal conductivity of CNT TIMs [57, 109] as a function of volume fraction. Within the framework of an effective medium approximation, the effective thermal conductivity will increase with volume fraction as the CNT TIM compresses. To calculate the volume fraction (i.e., the ratio of the volume occupied by CNTs to the nominal volume), the density of a single MWCNT is required, which can be difficult to measure with high fidelity given the variation in the number of walls in a given MWCNT. Therefore, mass density, which

only requires knowledge of measurable quantities (i.e., mass of the CNT array, apparent cross-sectional area of the Si growth substrate, and CNT TIM height), was used as a surrogate for volume fraction. The mass density for short, moderately tall, and tall CNT TIMs are plotted as functions of pressure in Figure 7.15. For the 3, 10, and 43 μm tall CNT TIMs, the mass densities monotonically increase with pressure by factors of approximately 3.7, 2.0, and 1.1, respectively.

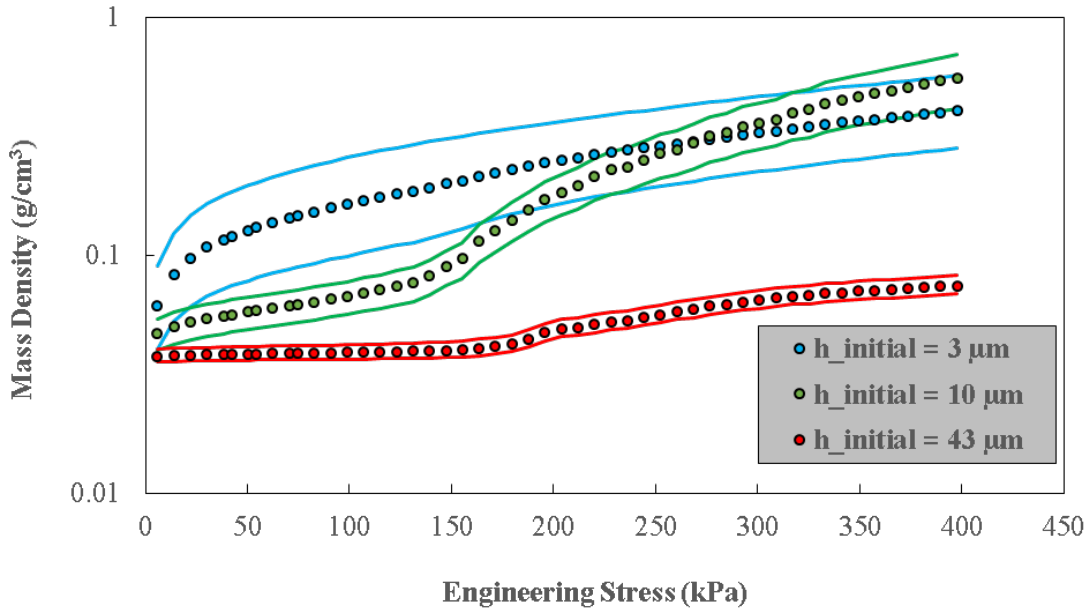

Figure 7.15. Mass density as a function of engineering stress for (a) 3, (b) 10, and (c) 41 μm tall CNT TIMs. Solid lines represent the 95% confidence intervals.

A consequence of a monotonically increasing mass density is that an effective medium approximation, such as the model developed by Nan et al. [109], would predict a continual increase in the effective thermal conductivity as a function of pressure that contradicts the observations in this work. Additionally, according to Equation (7.1), a monotonic increase in effective thermal conductivity (decrease in the bulk resistance) in conjunction with a monotonic decrease in contact resistance will result in a monotonic decrease in total

thermal resistance, which is not observed for the tallest CNT TIMs. In the work of Na et al. [110], the thermal resistance of CNT arrays of varying heights and mass densities was shown to decrease by approximately 70% with an approximate three-fold increase in the as-grown mass density (0.07 to 0.26 g/cm^3), which is expected because a greater packing density should increase the number of CNTs that participate in thermal transport. In this work, the range of as-grown mass densities is limited to approximately 0.02 g/cm^3, with the shortest CNT TIMs having the highest mass density and the tallest CNT TIMs having the lowest. Therefore, we expect the number of CNTs participating in thermal transport to be similar amongst our CNT TIMs.

While the as-grown mass density can be used as a basic indicator of thermal performance [110], the mechanical effects on thermal transport within CNT TIMs as they are compressed is not captured solely by this quantity. As moderately tall and tall CNT TIMs stiffen under compression due to inter-tube interactions [13, 19], their mass densities also steadily increase, and as they begin to buckle and deform in a coordinated manner, their mass densities increase at a relatively faster rate. Therefore, tracking mass density as a function of pressure in tandem with stiffness (Figure R1) can serve as an indicator of microstructural changes affecting thermal transport (i.e., inter-tube interactions as the CNT TIM stiffens and localized strain as the CNT TIM buckles) as the CNT TIM is compressed.

The preceding analysis and observations show evidence of a complex interplay between the contact and bulk resistances that are driven by the mechanical response of CNT TIMs to compression. The dependence of the contact resistance on pressure is congruent with traditional thermal contact conductance theory [1, 41] as the quantity and sizes of CNT-to-Ag foil contacts should increase upon compression, thus enhancing the

pathways for heat conduction. In contrast, minimal literature has been reported on the pressure dependence of the effective thermal conductivity of CNT TIMs, with many publications either measuring this quantity at a single pressure or assuming that the CNT TIM conducts heat effectively enough to neglect its contribution to the total temperature drop across the interface. The only prior work documenting pressure-dependent effective thermal conductivity of CNT TIMs was by Lin et al. [50], who reported a decrease in thermal diffusivity with increasing compressive stresses using the laser flash technique. Despite the dearth of prior work, the roles of defects, localized strain, and CNT-to-CNT contacts are commonly highlighted as key factors that can affect the effective thermal conductivity of CNT TIMs and are often qualitatively considered due to the difficultly in quantifying their contributions experimentally. Defects, localized strain, and CNT-to-CNT contacts should increasingly affect heat conduction not only in individual CNTs but also in the aggregate CNT TIM structure as the CNT TIM buckles (defects and localized strain) in a coordinated fashion (CNT-to-CNT contacts). Using microthermometry on individual MWCNTs, Pettes and Shi [58] reported thermal conductivities between 42 and 343 W/mK at 300 K, which corresponded to phonon mean free paths between 4 – 30 nm. And importantly, TEM imaging in their study revealed high defect concentrations (dislocations) within the MWCNTs that moderately correlated with the characteristic phonon mean free paths. Recent molecular dynamics simulations by Volkov et al. [111] indicate that significant reductions in thermal conductance of single-walled CNTs occur when buckling kinks are introduced into the lattice. Using the 3ω method on MWCNT bundles, Aliev et al. [112] reported that the thermal conductivity of CNT bundles monotonically decreased as CNTs were added to the bundles and elucidated the role of CNT-to-CNT contacts in

damping out-of-plane acoustic and optical phonon modes that significantly contribute to heat conduction.

7.4 Conclusions

The present nanoindention measurements reveal that tall and moderately tall CNT TIMs stiffen in the linearly elastic region, soften in the coordinated buckling region, and finally stiffen again in the densification region. Parallel PA measurements indicate that in the linearly elastic region and at the onset of the coordinated buckling region, shorter CNT TIMs have lower total thermal resistance relative to taller CNT TIMs due to a lower bulk resistance. Hence, the contributions of the bulk and contact resistances to the total thermal resistance can be modulated with CNT TIM height. Indeed, having the ability to control the contributions of the bulk and contact resistances could be advantageous depending on the application. If the application is limited more by thermal constraints relative to mechanical constraints (i.e., high heat flux and low mechanical stress), then shorter CNT TIMs may be a better option. In contrast, taller CNT TIMs may be more appropriate for applications that are limited by the mechanical constraints relative to thermal constraints (i.e., high mechanical stress and low heat flux).

8. THERMAL CONTACT CONDUCTANCE AT ELEVATED TEMPERATURES: MEASUREMENT SYSTEM AND THE CAPABILITIES OF CNT AND CNT/PETAL TIMS AT ELEVATED TEMPERATURES

8.1 Introduction

In a review of thermal management for future heat-generating electronics, panelists from Northrup Grumman, JPL, and Rockwell Collins explored the challenges that thermal engineers face in designing innovative cooling solutions for systems subjected to harsh or extreme environments in military, automotive and space applications. As many of these electronics are assembled in a modular fashion that manifests a thermal contact resistance, the need to develop light-weight TIMs of higher thermal conductivity and lower thermal coefficients of expansions was highlighted as a critical issue, particularly in extreme temperature and pressure enviornments. Electronic components in future NASA space systems will require operation in wide pressure and temperature ranges between 0 and 10 MPa and from -230°C to 486°C, while military units in avionics currently involve operation between -55°C and 125°C [113] under shock and vibration stimuli. In the automotive industry, semiconductor power densities are currently at 300 W/cm^2 [113] whereas the Intel i7 chip only generates 50 W/cm^2. Additionally, drive motor controllers in next-generation hybrid and fully-electric vehicles can generate heat in the kilowatt range [113]. Thermal contact conductance at elevated temperatures also

plays an important role in thermoelectric applications in which operating temperatues can reach 1000°C [114] and SiC devices that can theoretically operate up to 600°C [36].

In comparison to room temperature or sub-100°C applications, in which many different TIMs are available, high-temperature applications are relegated to sparse options. Thermal greases and solders are effective at reducing the temperature drop in microprocesser related applications, but will significantly degrade at temperatures above 180°C (Arctic Silver 5, Arctic Silver Inc. [115]) and 280°C (AuSn Indalloy, Indium Inc. [116]). As a result, thermal engineers often do not use TIMs (bare interface) or are limited to metallic foils in high-temperature applications. However, at the elevated temperatues and pressues, diffusion bonding between the constituent materials occurs, rendering any rework or maintanence a difficult task. Graftech Inc. offers graphitic based foils that are suitable for high-temperature applications and depending on the thickness of the foil, perform between 10 and 100 mm^2 K/W. While as-grown CNT TIMs, without any subsequent bonding technique or treatment, do not break performance barriers relative to current room-temperature, commercially-available TIMs, their stability at elevated temperatures may render them more appropriate for high-temperature applications. Studies have shown that CNTs are stable in oxididative environments up to approximately 450°C [117, 118], with defects and diameter playing a major role in their reactivity with oxygen [117]. Bom et al. [117] and Zhao et al. [118] increased the stability of raw CNTs in oxidative environments to 700-800°C by annealing out the defects at temperatures between 2800-3000°C in oxygen-free atmospheres.

An equally important necessicity is the development of experimental systems that are capable of measuring the performance of TIMs and quantifying thermal properties of

materials in extreme environments. Additionally, many materials, such as metals, exhibit strong temperature dependent thermal and mechanical properties at these temperatures. Commonly used data analysis techniques ignore both of these factors and as a result yield inaccurate results, rendering a need for measurement systems with such capabilities in high-temperature environments. Presently, experimental quantification of the performance of TIMs and thermal properties of materials at eleveted temperatures is particularly sparse for abnormal thermal environments, with values often selected from room-temperature results, or in some cases, ignored completely. However, many different techniques are certainly able to recreate high-temperature environments [114, 119 - 121]. The photoacoustic technique is capable of testing the performance of TIMs up to 250°C [36, 38], as limited by the microphone hardware.

In this work, a thermal contact resistance measurement system at Sandia National Laboratories was built and modified to measure the contact resistance of metallic interfaces under wide interfacial pressure (0.1 – 8 MPa) and temperature (>450°C) ranges. The system was used to measure the thermal contact resistance of stainless steel, aluminum and copper interfaces as well as CNT and CNT/graphitic petal TIMs.

8.2 Experimental Setup

The measurement system is based on the ASTM D470-06 standard [122] for measuring contact resistance. The system is equipped with two bars of known thermal conductivity that serve as heat flux meters. Each heat flux meter has 7 thermocouples to monitor the temperature gradient and thus make known the heat flux at the interface between the two bars. In this work, the heat flux meters are stainless steel 304, Al6061, or Cu101001 and

of tailored length to provide a large enough temperature gradient to yield accurate measurements of the thermal contact resistance between them. At elevated temperatures, radial radiation heat flux from meters causes significant non-linearity of the measured temperature profile. To mitigate these losses, eliminate convective losses, and ultimately maximize heat conduction across the interface, the measurement system is housed in a Kurt J. Lesker© vacuum chamber capable of reaching pressures below 10 μTorr. Additionally, an Au electroplated type 304 stainless steel radiation shield surrounds the heat flux meters to further reduce radiative losses. The maximum interface temperature with this equipment is approximately 630°C for bare interfaces. The interface pressure can be adjusted *in situ* and can also compress the interface up to 8 MPa for ½-inch diameter heat flux meters. Due to the large thermal mass that the system possesses and thus long time constants, a custom PID controller was implemented to maintain a constant pressure (+/- 0.5 kPa) on the interface. A real-time multivariate regression code, based on the Levenberg-Marquardt method, was developed to fit thermal quantities to the experimental data.

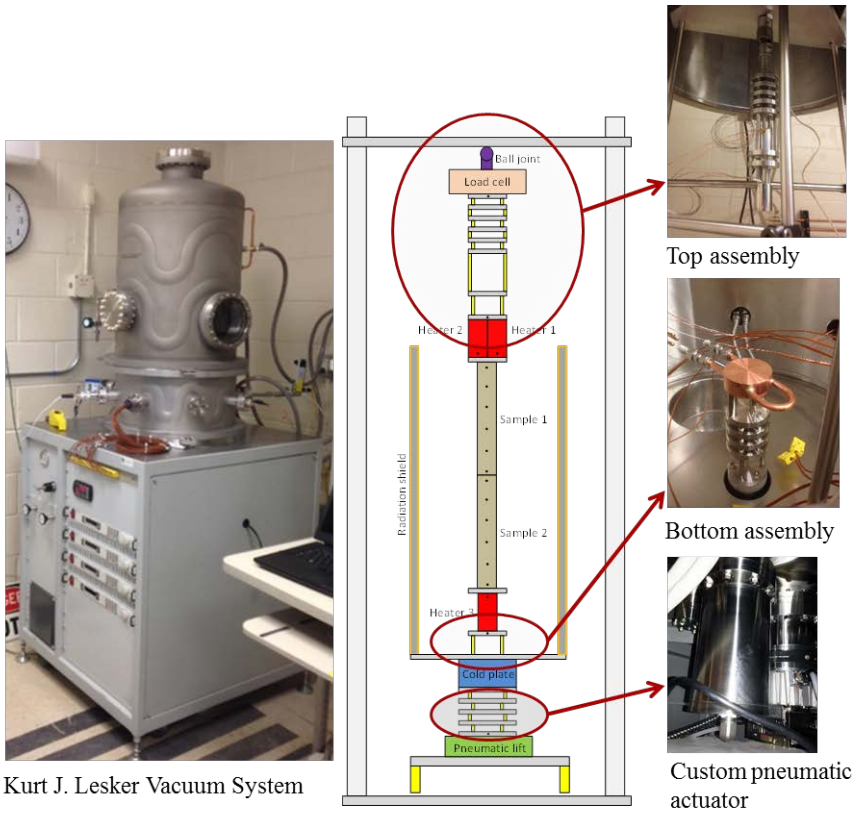

Figure 8.1. 1D steady-state measurement system for thermal conductivity and thermal contact resistance measurements at elevated temperatures [123].

The model accompanying the measurement system is based on the one-dimensional heat conduction equation with an extra term to account for radiative losses. The governing equation and boundary conditions are

$$k\frac{d^2T}{dx^2}+\frac{dk}{dT}\left(\frac{dT}{dx}\right)^2-\frac{\sigma}{R_{rad}}\left(T^4-T_o^4\right)=0 \tag{8.1}$$

$$T\left(x=0\right)=T_1 \qquad T\left(x=2L\right)=T_4 \qquad q''\left(x=L\right)=-k\frac{dT}{dx} \tag{8.2 - 8.4}$$

in which T is the temperature in the heat flux maters, k is the temperature-dependent thermal conductivity of the heat flux meters, σ is the Stefan-Boltzmann constant, T_0 is the

temperature of the bell jar, and R_{rad} is the radiative resistance between the heat flux meters and bell jar. R_{rad} is defined below as

$$R_{rad} = \frac{1-\varepsilon_{HFM}}{\varepsilon_{HFM}\pi D_{HFM}} + \frac{1}{\pi D_{HFM} F_{HFM-shield}} + 2\left[\frac{1-\varepsilon_{shield}}{\varepsilon_{shield}\pi D_{shield}}\right] + \frac{1}{\pi D_{shield} F_{shield-jar}} + \frac{1-\varepsilon_{jar}}{\varepsilon_{jar}\pi D_{jar}} \quad (8.5)$$

where ε and D are the emissivity and diameter, respectively, of each the heat flux meters, radiation shield, and bell jar. $F_{HFM\text{-}shield}$ is the view factor from the heat flux meters to the radiation shield and $F_{shield\text{-}jar}$ is the view factor from the radiation shield to the bell jar. Temperature-dependent values for all intrinsic material properties are considered in the model. A multivariate regression algorithm based on the Levenberg-Marquardt method fits the model to the data with the heat flux, ambient temperatures, and temperatures at the boundaries of the heat flux meters as fitting parameters. Typical temperature profiles at interface temperatures of 150 and 510°C that highlight the radiative effects are shown below in Figures 8.2 (a) and (b), respectively.

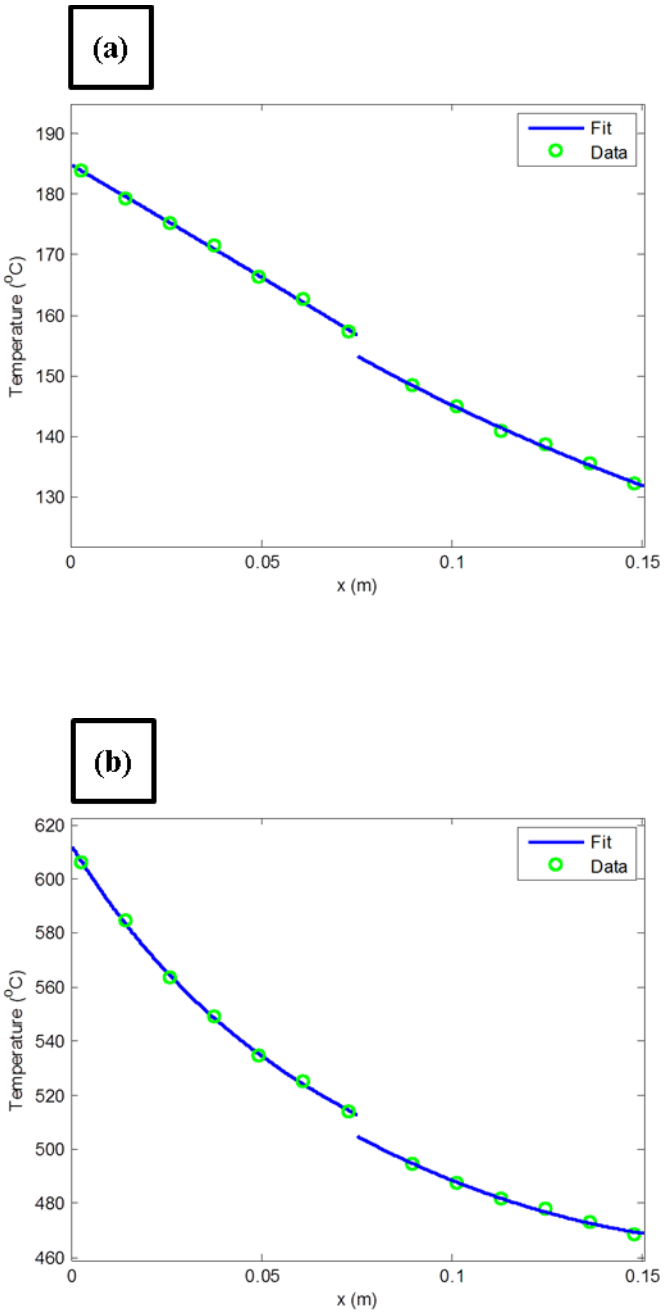

Figure 8.2. Typical temperature profiles at (a) 150°C and (b) 510°C.

8.3 Results and Discussion

8.3.1 Bare Interfaces

A stainless steel 304 (SS304) heat flux meter was interfaced with each with SS304, aluminum 6061 (Al 6061) and copper 10100 (Cu 10100) heat flux meters. The thermal contact resistance between the heat flux meters was measured in the temperature range of 150 – 550°C for the SS304-SS304 and SS304-Cu10100 combinations and 150 – 450°C for the SS304-Al6061 combination. The temperature range for the latter was reduced to remain under the melting temperature of Al6061. For all combinations, the interface pressure was approximately 1.50 – 4.25 MPa. Figures 8.3 (a)-(c) show how thermal contact resistance responds to a change in interface pressure at each surface combination. Further, Figure 8.3 (d) shows how thermal contact resistance responds to a change in temperature at constant interface pressure for each surface combination. The dashed lines represent the interface resistance during the cool-down phase.

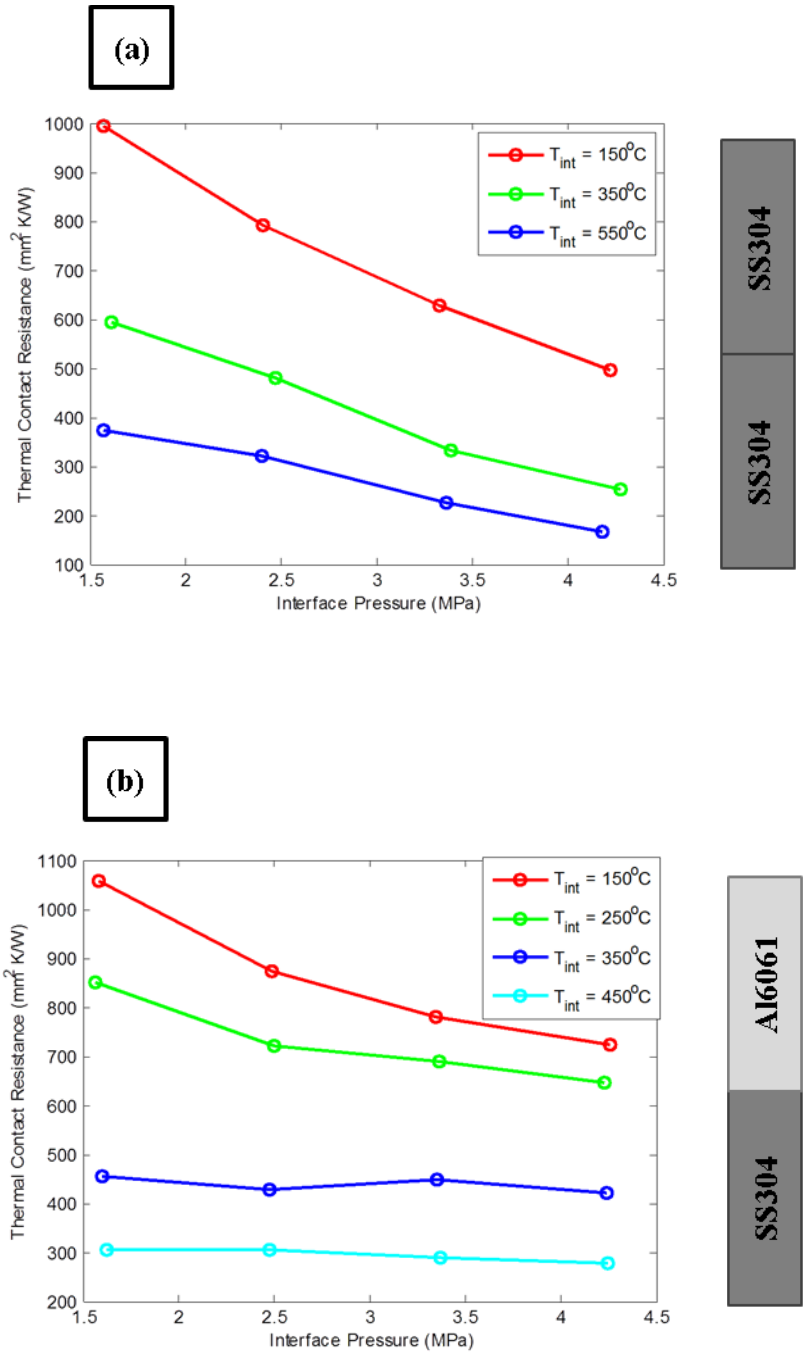

Figure 8.3. Thermal contact resistance as a function of interface pressure for (a) SS304-SS304, (b) SS304-Al6061, and (c) SS304-Cu10100. Thermal contact resistance as a function of interface temperature for all three combinations in (d) at an interface pressure of 1.5 MPa. The dashed lines in (d) represent the ramp down in temperature [124].

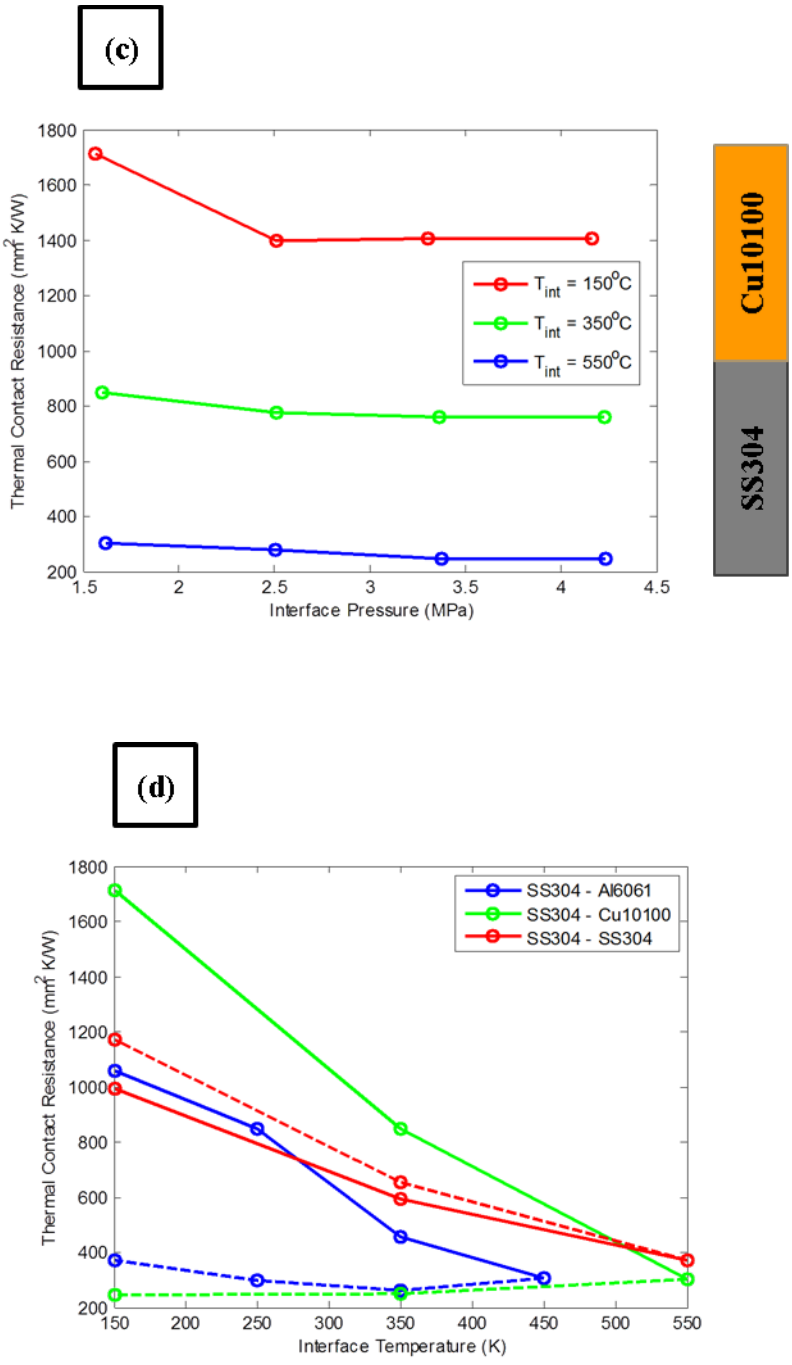

Figure 8.3. Continued.

For all three material combinations in Figures 8.3 (a)-(c), the thermal resistance monotonically decreases with increasing pressure as the materials conform and engage. The rate of change of the thermal resistance with interface pressure is driven by the

microhardness and the initial surface profile of the material, the former of which is dependent on temperature. The rate of change of thermal resistance with interface pressure is noticeably less dramatic as the interface temperature is increased. This is likely due to the pressure and temperature dependence of the microhardness of each material as well as the measurement sequence. The interface pressure was first loaded from 1.50 to 4.25 MPa at one temperature, then unloaded to 1.50 MPa and subsequently heated to the next temperature. As a result, the material surfaces repeatedly conformed to each other, and this effect becomes more influential in creating additional contact as the material softens at higher temperatures. In Figure 8.3 (d), the Al6061-SS304 and Cu10100-SS304 combinations possess a significant hysteresis in the temperature cycle, indicating that the surface of the softer material (Al6061 or Cu10100) plastically conforms to the harder material (SS304). The resulting bonded interface was observed post-test, but was not quantified in this case.

8.3.2 CNT and CNT/Petal TIMs

The intention of this study was to assess the efficacy of carbon-based materials as TIMs at elevated temperatures (150 to 450°C) and moderate interface pressures (120 to 640 kPa). Additionally, the results stemming from this study were intended to serve as an extension of the findings in Chapter 7, particurily at higher interface pressures and temperatures. In Chapter 7, the effective thermal conductivity and thermal contact resistance as functions of pressure were estimated from the measured thermal resistance values and bond line thickness estimates. The same methodology in Chapter 7 was employed in this work using the 1D reference bar technique rather than the PA technique. However, alignment of the

sample stack (i.e., heat flux meter/TIM/heat flux meter) proved to be a difficult endeavor, given the manner in which the measurement system was initially constructed as well as the nature in which the measurements were conducted.

Prior to conducting measurements on the CNT and CNT/petal sample set, a series of measurements were performed on a bare interface (i.e., heat flux meter/heat flux meter) to determine the repeatability of the sample loading procedure. Figure 8.4 below shows the measured thermal resistance values for four independent alignments in which the heat flux meters were guided into contact, the thermal resistance was measured, the flux meters were guided out of contact, and finally guided back into contact for another measurement. These measurements were conducted at relativley low interface pressures and temperatures (120 kPa and 150°C) in order to minimize irreversible changes to the heat flux meter surfaces.

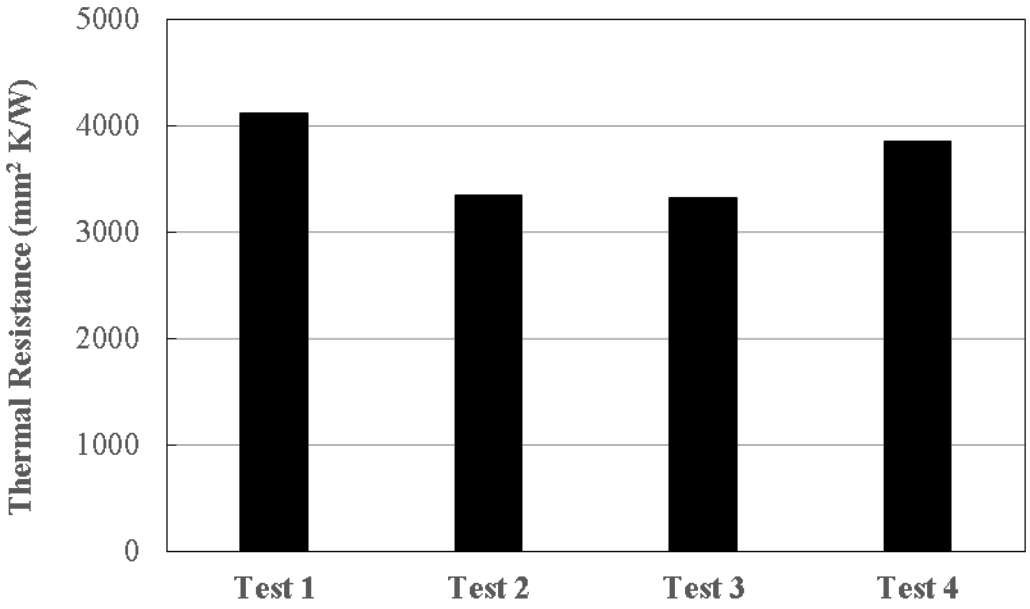

Figure 8.4. Measured thermal resistance values for bare interfaces in which the heat flux meters were guided into contact using the alignment procedure.

In Figure 8.4., the average thermal resistance is approximately 3668 mm^2 K/W with a standard deviation of approximately of approximately 392 mm^2 K/W. The maximum and minimum values are approximately 4130 and 3326 mm^2 K/W, respectively.

The thermal resistances of CNT and CNT/petal TIMs were measured in pressure and temperature ranges of 120 – 640 kPa and 150 - 450°C. The pressure was held constant at 120 kPa at each 150°C, 300°C, and 400°C. At 450°C, the TIMs were subjected to mechanical cycling between the minimum and maximum pressures, 120 and 640 kPa, respectively. The TIMs comprised of 100 μm-thick Cu foils with CNTs or CNT/petals on one side. The TIM heights ranged from approximately 3 – 50 μm, which were chosen to match the CNT TIMs measured in Chapter 7.

Figures 8.5 and 8.6 below show the measured thermal resistance as a function of pressure and temperature for a CNT TIM with approximately 40 μm tall CNTs and a CNT/petal TIM of similar height. The other CNT TIMs measured in this study possess similar behavior with the thermal resistances of all the CNT and CNT/petal TIMs residing in the range of 200 – 700 mm^2 K/W at an interface temperature of 450°C. Due to the uncertainty in the alignment procedure (see Figure 8.4 and the range of thermal resistances measured for the CNT and CNT/petal TIMs, comparisons between TIMs of varying CNT or CNT/petal heights were not explored. Nonetheless, each of the CNT and CNT/petal TIMs outperformed a bare Cu foil, which possessed thermal resistances in the range of 900 – 1200 mm^2 K/W across the entire pressure and temperature ranges.

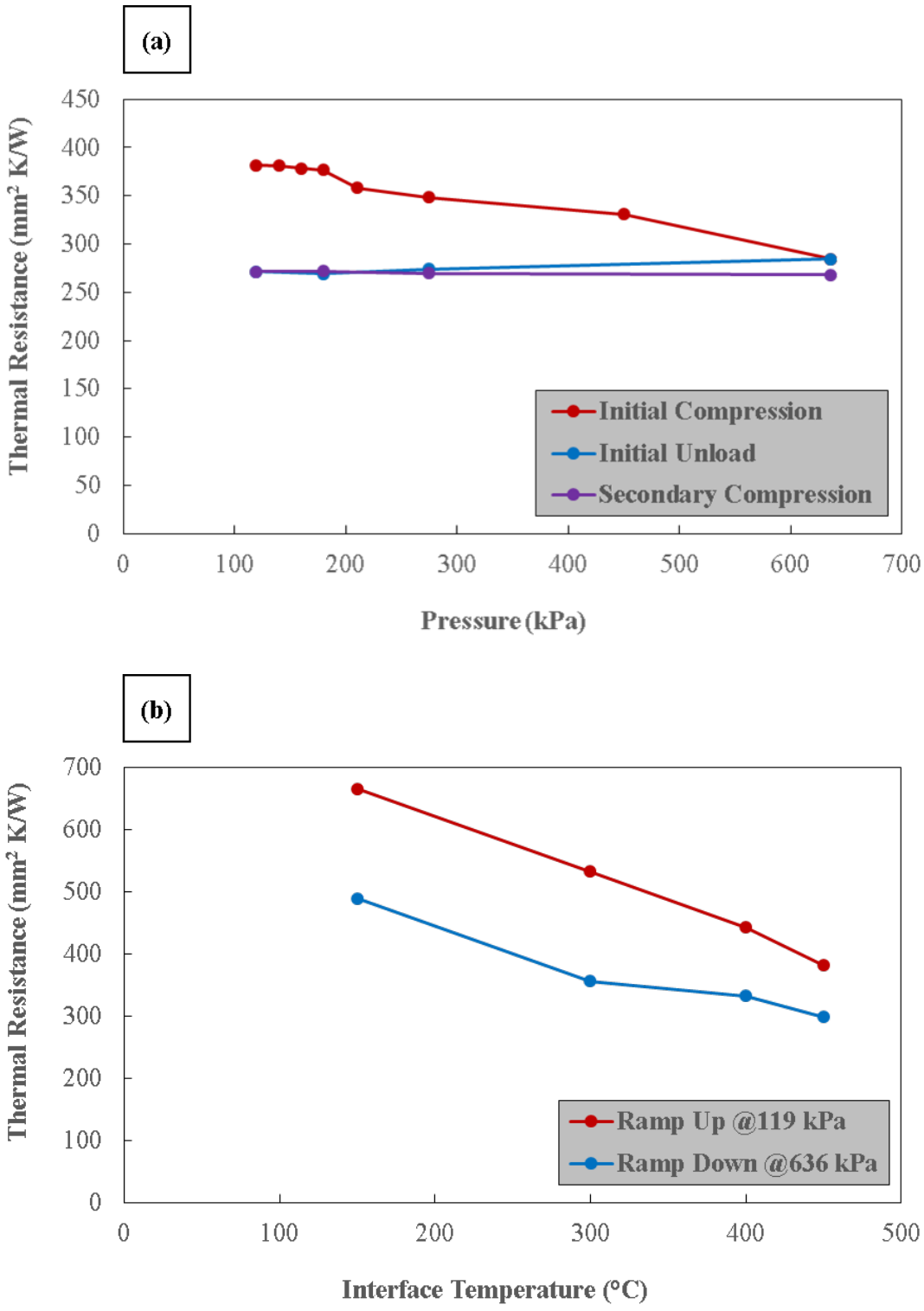

Figure 8.5. (a) Measured thermal resistance as a function of pressure for CNT TIM at an interface temperature of 450°C and (b) measured thermal resistance as a function of interface temperature for CNT TIM.

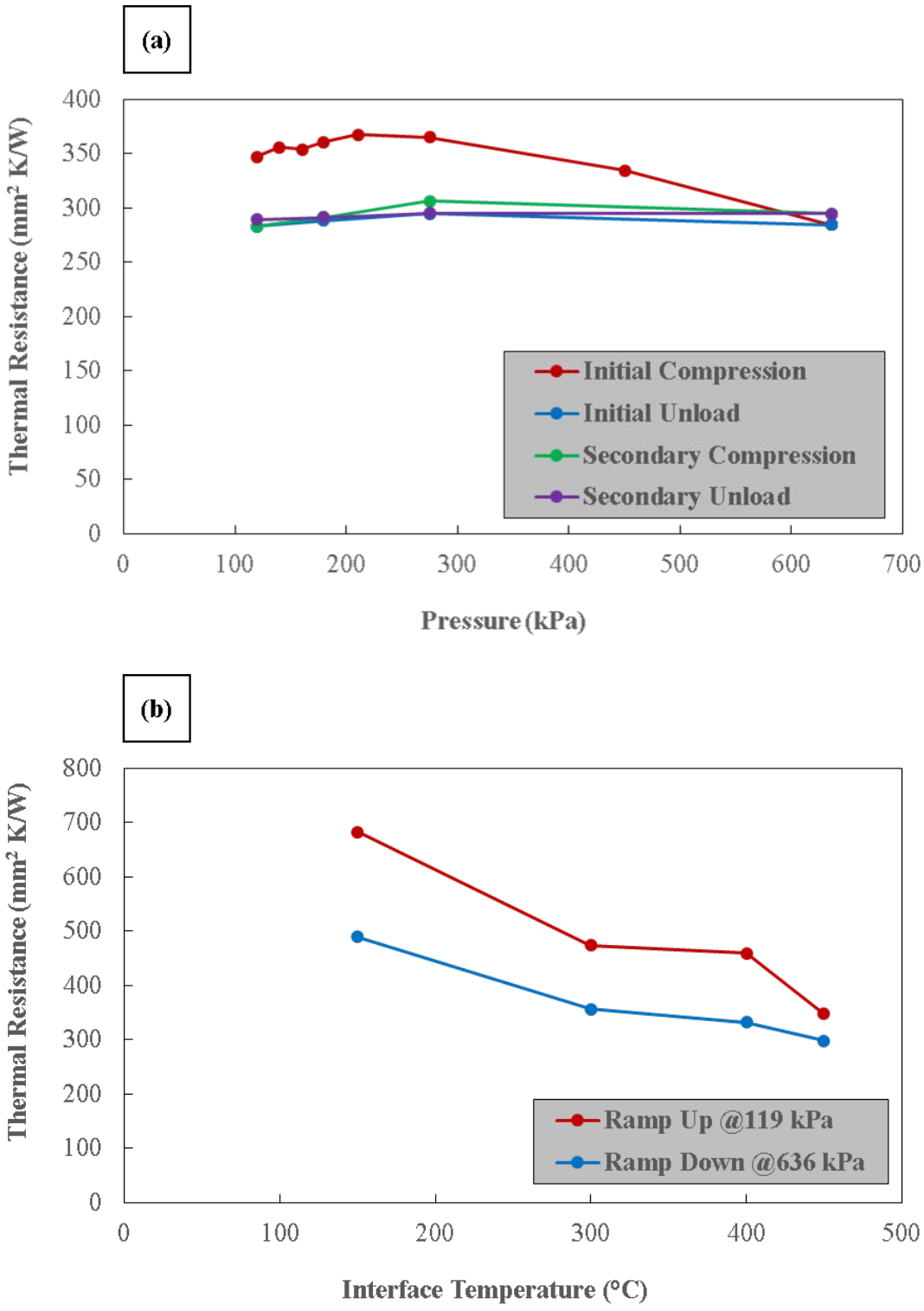

Figure 8.6. (a) Measured thermal resistance as a function of pressure for CNT/petal TIM at an interface temperature of 450°C and (b) measured thermal resistance as a function of interface temperature for CNT/petal TIM.

During the initial compression, the CNT and CNT/petal TIMs exhibit different thermal behavior. The thermal resistance of the CNT TIM remains relatively constant between 120 and 180 kPa. At 180 kPa, a slight decrease in thermal resistance of approximately 20 mm^2 K/W occurs, which is in the vicinity of the pressure at which buckling of the CNT array that is expected to occur (see Figure 7.4 (d) in Chapter 7). As the CNT TIM is compressed to 640 kPa, the thermal resistance decreases at a relatively constant rate. The thermal resistance of the CNT/petal TIM slightly increases by 20 mm^2 K/W as the pressure is increased to 210 kPa. After 210 kPa, the thermal resistance decreases in a moderately aggressive manner to 640 kPa. This behavior is likely due to the morphology of the CNT/petal surface that initially comes into contact with the heat flux meter. Typical CNT/petal growth is more aggressive along the edges of the substrate (Cu foil), which results in a 'bowl-like' morphology. As a result, the CNT/petal TIM must be compressed to sufficiently high pressures in order to fully engage the heat flux meter. Additionally, above 275 kPa, the rate of change of the thermal resistance for the CNT/petal TIM appears to be more dramatic than the CNT TIM, suggesting that the CNT/petal TIM may outperform the CNT TIM at higher pressures.

During the subsequent compression cycles, both the CNT and CNT/petal TIMs exhibit a hysteresis relative to the initial compression. For the CNT TIM, the CNT array plastically deforms and likely only recovers a few microns of its original height. During the compression cycles, the contact area and bond line thickness (i.e., CNT array height) likely remain relatively constant. This compaction and plastic deformation of the CNT TIM can be observed in the post-mortem SEM images in Figures 8.7 (b) and (c) below. CNTs decorated with petals are considerably stiffer than undecorated CNTs. Therefore, the

aggregate microstructure of the CNT/petal array should remain relatively unchanged within the pressure range of 120 – 640 kPa as shown below in Figure 8.8 (c). The hysteresis in Figure 8.7 (a) is likely due to plastic deformation of the graphitic petals at the surface of the CNT/petal TIM that engages with the heat flux meter, which can be observed in the post-mortem SEM images in Figures 8.8 (b) and (d). A minimal hysteresis in the thermal resistance is observed during the subsequent secondary compression cycles, indicating that the CNT and CNT/petal TIMs possess adequate mechanical cyclic stability.

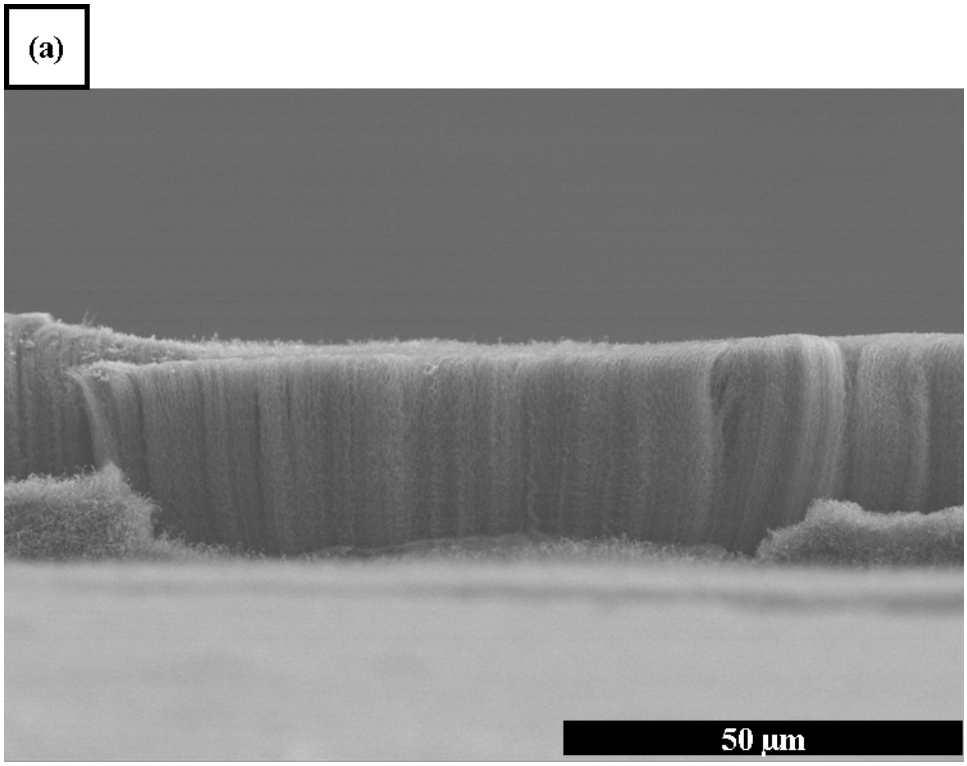

Figure 8.7. (a) As-grown SEM image of a CNT TIM and (b)-(c) post-mortem SEM images of a CNT TIM.

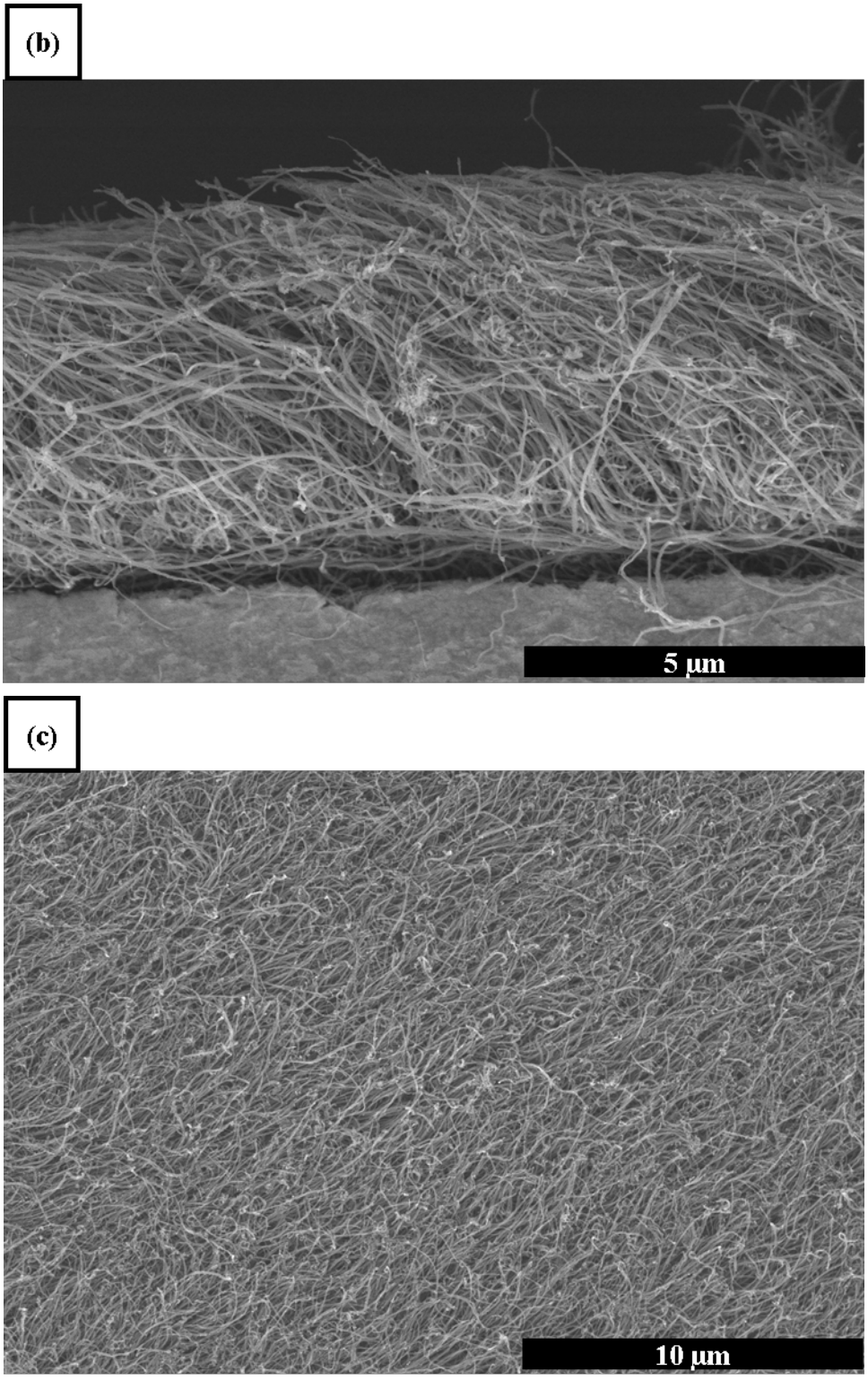

Figure 8.7. Continued.

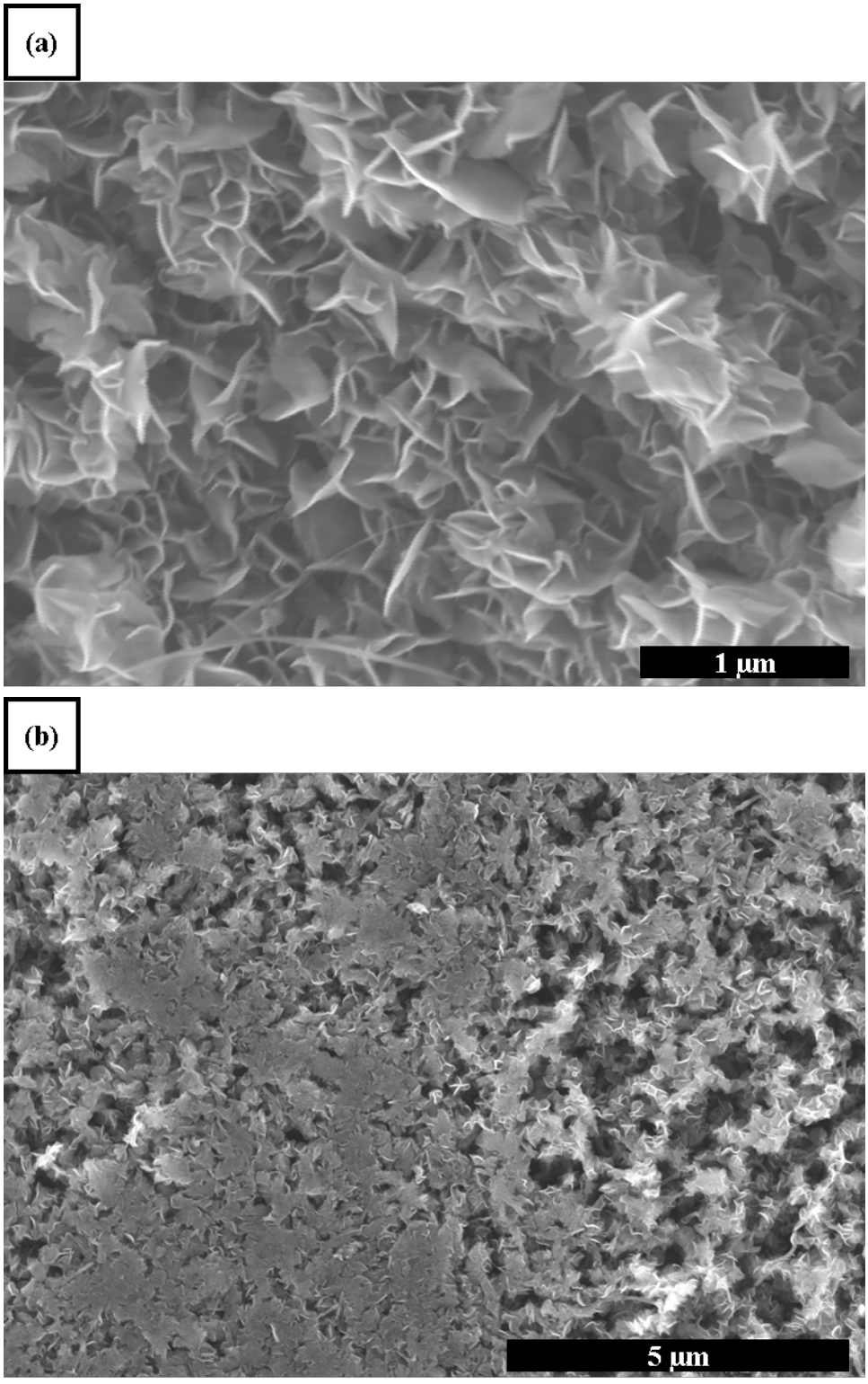

Figure 8.8. (a) As-grown SEM image of a CNT/petal TIM and (b)-(d) post-mortem SEM images of a CNT/petal TIM.

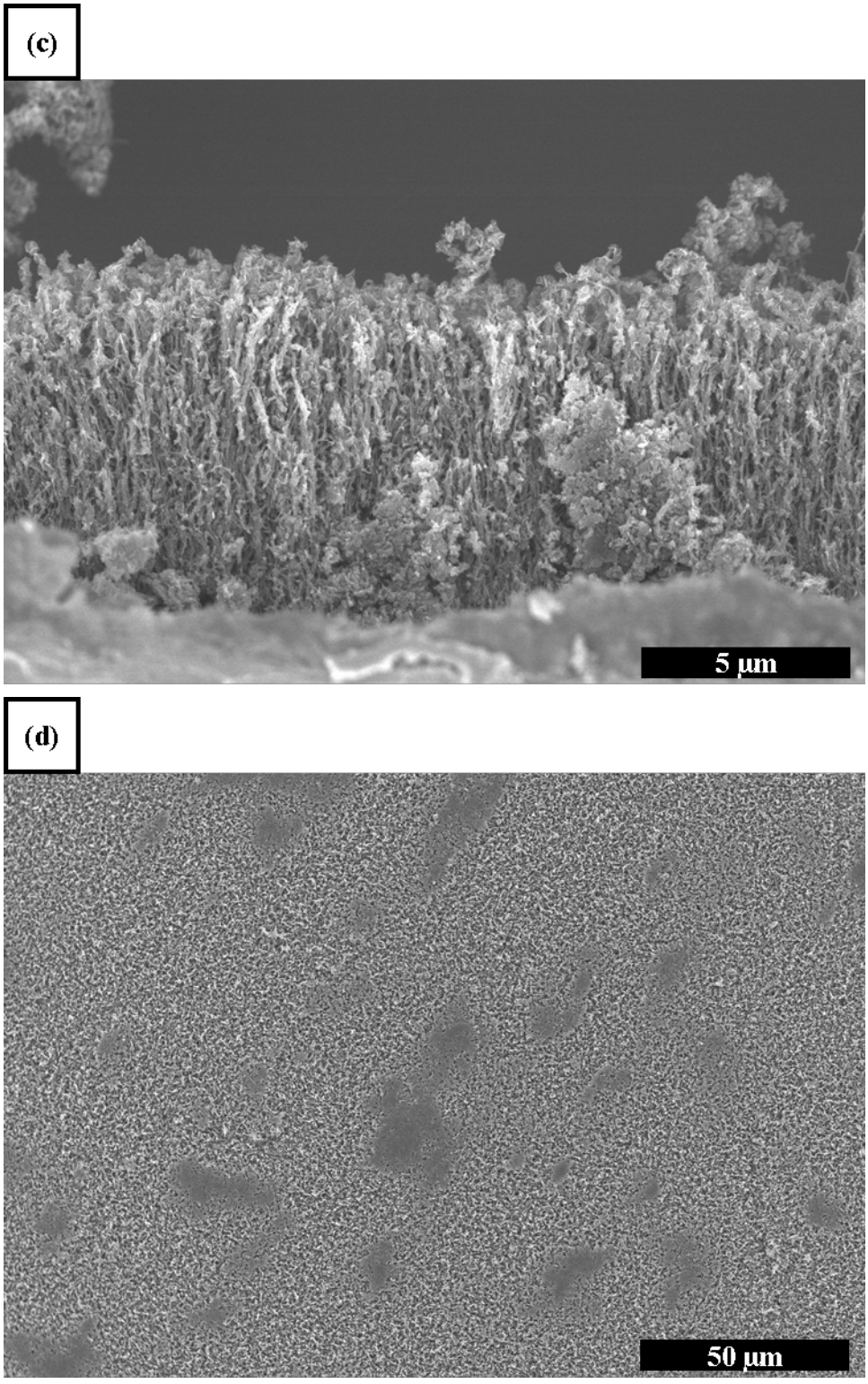

Figure 8.8. Continued.

The flattened petal regions of the CNT/petal TIM provide sufficient contrast in the SEM image and enables a basic image analysis to define the regions of contact with the heat flux meter. These regions are defined by contour lines in Figure 8.9 and ultimately yield an estimation of the contact area. The contact area fraction (i.e., real to nominal) was estimated by determining the number of image pixels enclosed in the contours relative to the nominal area (i.e., total number of pixels in the image). By performing this image analysis on Figure 8.8, the fraction of contact that the CNT/petal TIM makes with the heat flux meter is estimated to be approximately 0.1. In comparison, Cola et al. [41] and Sadasivam et al. [102] reported contact area fractions on the order of $O(0.001)$ at a pressure of approximately 150 kPa. The significant increase in contact area achieved by flattening the graphitic tips of the CNT/petal TIM should yield a comparable reduction in the thermal resistance relative to the CNT TIM. However, the large uncertainty associated with the alignment procedure renders a comparison between the CNT/petal and CNT TIMs unresolvable.

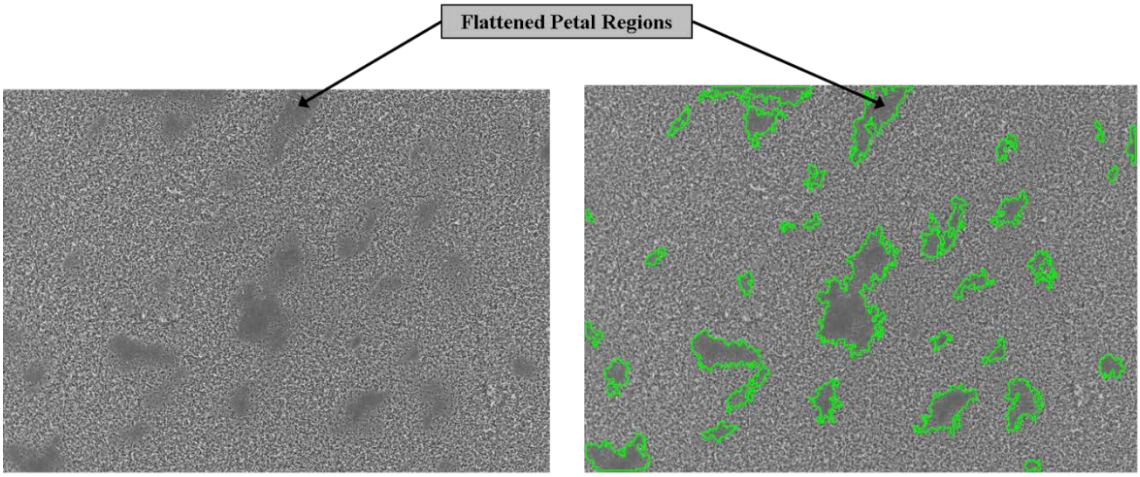

Figure 8.9. Post-mortem image analysis and processing of flattened petal regions.

As the interface temperature was increased from 150 to 450°C, the thermal resistances of the CNT and CNT/petal TIMs monotonically decreased by approximately 40 and 50% of the initial thermal resistance at 150°C, respectively. Conversely, the thermal resistance for both TIMs monotonically increased as the interface was cooled from 450 to 150°C, and the entire temperature cycle exhibited a hysteresis. Similar trends for similar CNT TIMs and instrumentation have been reported in the experiments conducted by Hao et al. [125], in which the thermal resistance decreased by 48% as the interface temperature was increased from 100 to 700°C, with a slight hysteresis forming after the initial temperature cycle. In their work, subsequent secondary and tertiary temperature cycles exhibited similar monotonic changes in the thermal resistance without significant hysteresis. Using molecular dynamics on a CNT/Cu interface, Wang et al. [126] reported a monotonic decrease in thermal resistance by 17% as temperature increased from room temperature to approximately 477°C. This behavior is likely due to activation of additional vibrational modes that contribute to thermal transport across the interface, which dominates over any additional scattering mechanisms that would decrease the thermal conductivity of the CNT or CNT/petal array [125].

8.4 Conclusions

In this work, the thermal performance of bare-interface configurations (stainless steel/stainless steel, stainless steel/aluminum, and stainless steel/copper) as well as CNT and CNT/petal TIMs were investigated in abnormal temperature environments using a customized 1D reference bar system. For bare interfaces, the thermal resistance decreased

with increasing pressure as the materials engaged and conformed. This effect was less dramatic as the interface temperature was increased, implying that the interface softened and forms a bond between the mismatched materials. The bonding induced by elevated pressures and temperatures resulted in a hysteresis in the thermal resistance during the temperature cycle for the stainless steel/aluminum and stainless steel/copper configurations.

The CNT and CNT/petal TIMs outperform a bare interface as well as a bare Cu foil, exhibiting adequate mechanically cyclic stability at 450°C and a hysteresis in thermal resistance during the temperature cycle. Post-mortem SEM images revealed that the CNT TIMs were significantly compacted and plastically deformed while the aggregate structure of the CNT/petal TIMs remained relatively unchanged. For the latter, post-mortem SEM images revealed that the petals on the surface of the TIM flattened, indicating that under sufficient pressure and temperature conditions, the surface of the CNT/petal TIM began to conform to the stainless steel heat flux meter. This observation suggests that sufficient pressure and temperature conditions are necessary for CNT/petal TIMs to significantly outperform CNT TIMs.

Acknowledgements

Sandia National Laboratories is a multi-program laboratory managed and operated by Sandia Corporation, a wholly owned subsidiary of Lockheed Martin Corporation, for the U.S. Department of Energy's National Nuclear Security Administration under contract DE-AC04-94AL85000.

9. THERMAL CHARACTERIZATION OF THERMAL

9.1 Introduction

The overall performance of molten salt batteries is dictated by complex multiphysics consisting of electrochemical processes, mechanical responses, and thermal transport mechanisms. The molten electrolyte and separator [LiCl/KCl, MgO] serve as the battery's hub by providing an ionically conductive path between the anode [Li(Si)] and cathode [$CaCrO_4$ or FeS_2]. Depending on the application, the desired lifetimes can vary between a few seconds and one hour [127], which is partially dictated by the cooling rate of the molten electrolyte. To mitigate cooling, molten salt batteries are packaged with insulation materials such as Fiberfrax board and Min-K thermal insulation. The latter is often employed in molten salt batteries that require long lifetimes [128]. These insulations are included at the top and bottom of the battery stack and are compressed under force before the battery can is sealed. Other Fiberfrax insulation is wrapped around the stack under tension.

Predictive models for molten salt battery activation can be improved with high fidelity measurements of thermal properties such as heat capacity and thermal conductivity. Specifically, non-molten separator thermal conductivity is necessary for predicting rise time whereas insulation thermal conductivity has been found to be a great source of uncertainty in predicting the lifetime of the battery [129]. Currently, the

insulation thermal conductivity is not implemented as a function of strain in the Sandia multiphysics model for battery activation (TABS v 3.0).

Various techniques, either steady state or transient, can be employed to measure thermal conductivities of materials and each has advantages and disadvantages. Transient techniques such as laser flash, thermoreflectance, and photoacoustic provide quick determination of thermal conductivities relative to steady state techniques, but generally require prior knowledge of the density and heat capacity of the material. Steady state techniques such as reference bar and infrared thermography do not require knowledge of the density and heat capacity, but are not suitable for rapid characterization of large quantities of samples. In this work, a steady state technique [122] was used to measure the thermal conductivities of the separator pellets as well as annealed Fiberfrax board and Min-K insulation materials in different ambient environments and compressive stresses which are congruent with common molten salt battery packaging protocols.

9.2 Experimental Setup

The separator material was formed by mixing, melting, and grinding LiCl/KCl electrolyte salt with MgO to form a powder. The mixture was then hydraulically pressed to form LiCl/MgO/KCl pellets of varying thicknesses. Pellets were all 1.75 g/cm^3 in density.

The Fiberfrax board and Min-K insulation materials were purchased in a variety of thicknesses from Unifrax and Morgan Thermal Ceramics, respectively. The insulation materials were then annealed in dry air at 600°C for 4 hours to remove moisture and stored

in a dry environment until tested. SEM images showing the cross-section of the insulation materials are shown below in Figures 9.1 (a) and (b).

The steady state reference bar technique is based on the ASTM D470-06 standard for measuring thermal conductivity and contact resistance and is used to measure the thermal conductivity of the different materials as well as the contact resistance with stainless steel 304 (SS304).

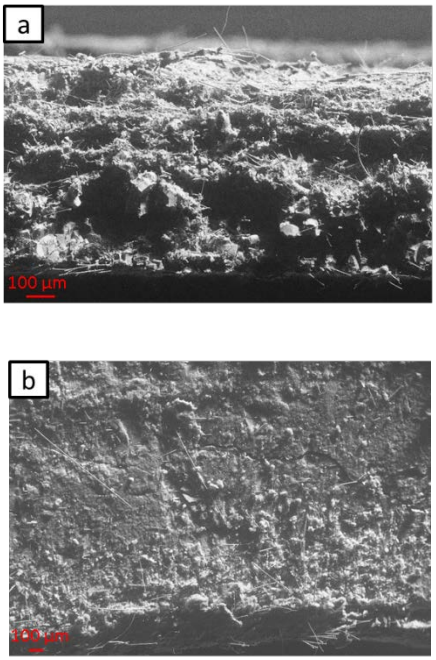

Figure 9.1. Cross-sectional SEM images of (a) annealed Fiberfrax board and (b) annealed Min-K.

and Macor heat flux meters. The system, shown in Figure 9.2 uses thermocouples to measure the temperature gradient in the heat flux meters while a mechanical translator compresses the interface to a load which is measured by a load cell. The mechanical translators are terminated with flat plates which are also cooled and heated to constant temperatures. The system has the capability to measure thermal properties in Ar, He, N_2,

air, and vacuum, which can simulate the hermitically sealed environment of the battery and gases released during chemical reactions. Note that thermal conductivity values measured by this technique are solely in the cross-plane direction.

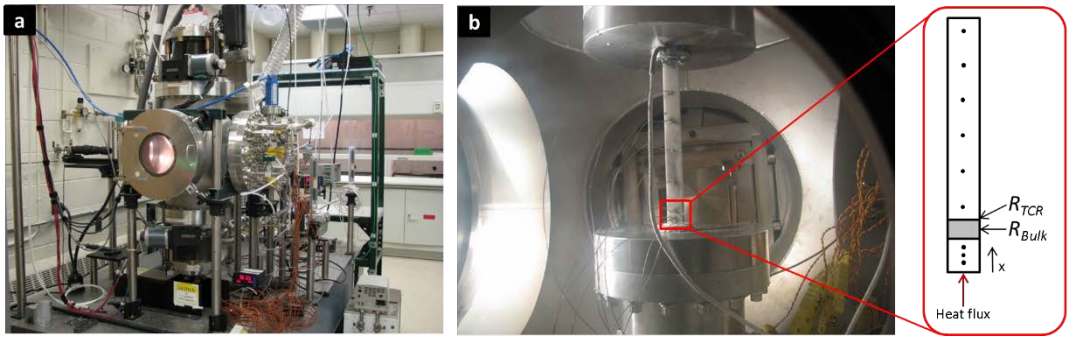

Figure 9.2. Thermal conductivity measurement system utilizing a 1D reference bar technique. Photographs of (a) the vacuum chamber and (b) the heat flux meters (HFMs) instrumented with thermocouples.

When compressed to a constant strain, Fiberfrax and Min-K insulations are known to undergo stress relaxation for extended periods of time. Therefore, both load and strain were measured simultaneously during measurements. Strain was recorded using a camera image of the sample.

The thermal model that accompanies the measurement technique is based on the one dimensional heat conduction equation and depending on the ambient environment (vacuum or gas), includes radiative and convective losses to the surroundings. The temperature throughout the stack is determined by solving Equation (9.1)

$$\frac{d}{dx}\left(k_{HFM}\frac{dT}{dx}\right)-\varepsilon\sigma\left(T^4-T_{surr}^4\right)-h\left(T-T_\infty\right)=0 \tag{9.1}$$

where T is the temperature in the stack along the direction x, k_{HFM} is the thermal conductivity of the heat flux meter, ε is the emissivity of the heat flux meter, σ is the Stefan-

Boltzmann constant, T_{surr} is the temperature of the surroundings that exchange thermal radiation with the heat flux meters, h is the convective heat transfer coefficient and T_{∞} is the average temperature of the ambient gas. The total thermal resistance between the top and bottom heat flux meters is determined by fitting Equation (9.1) to the temperature profiles in the heat flux meters using COMSOL. For the separator pellets, SS304 heat flux meters were chosen while Macor heat flux meters were chosen for the insulation materials. Note that the thermal conductivity of the Macor heat flux meters was determined by testing the material against SS304 bars of known thermal conductivity. The temperature profile and the thermal conductivity of the heat flux meters are used to determine the heat flux, temperature drop, and ultimately the thermal resistance across the interface. In Equation (9.2) below, the total thermal resistance between the heat flux meters (R_{total}) comprises of two contact resistances (R_{TCR}) that are in series with the bulk (intrinsic) resistance (R_{bulk}) of the material of interest:

$$R_{total} = R_{bulk} + R_{TCR} = \frac{t}{k} + R_{TCR} \tag{9.2}$$

where t and k are the thickness and thermal conductivity of the material of interest, respectively. The thermal conductivity can be determined by measuring the total thermal resistance between the heat flux meters for different thicknesses of the material of interest. This produces a linear relationship between thermal resistance and material thickness in which the inverse slope of the linear relationship is the thermal conductivity and the y-intercept is the contact resistance. The uncertainties associated with this measurement technique include thermocouple error, uncertainty in estimating the thickness, regression uncertainty, and sample to sample uncertainty.

9.3 Results and Discussion

Thermal conductivity measurements on the separator pellets (LiCl/MgO/KCl) were conducted within the pressure range of 400 and 2250 kPa and an average interface temperature (material temperature) of approximately 45°C. Due to the fact that the molten salt battery materials are moisture sensitive, the system was purged with dry air (5-10% humidity) during thermal testing. Tests were conducted on mixtures of three distinct thicknesses of 0.5, 1, and 2 mm. The thermal conductivity of the mixture and contact resistance with the heat flux meters were estimated by a linear fit to the measured thermal resistance and mixture thicknesses for interface pressures of 400, 1700, and 2250 kPa.

The variation in the measured thermal resistance for samples of the same thickness is greatest at lower interface pressures and smallest at the highest interface pressure. This indicates that the sample to sample uncertainty decreases with increasing pressure and that the misalignment between the separator pellet and heat flux meters is mitigated as the pressure increases. The thermal conductivity and contact resistance as functions of interface pressure are shown below in Figure 9.3 (a) and (b), respectively. The error bars include the sample to sample, linear fit, and thermocouple uncertainty.

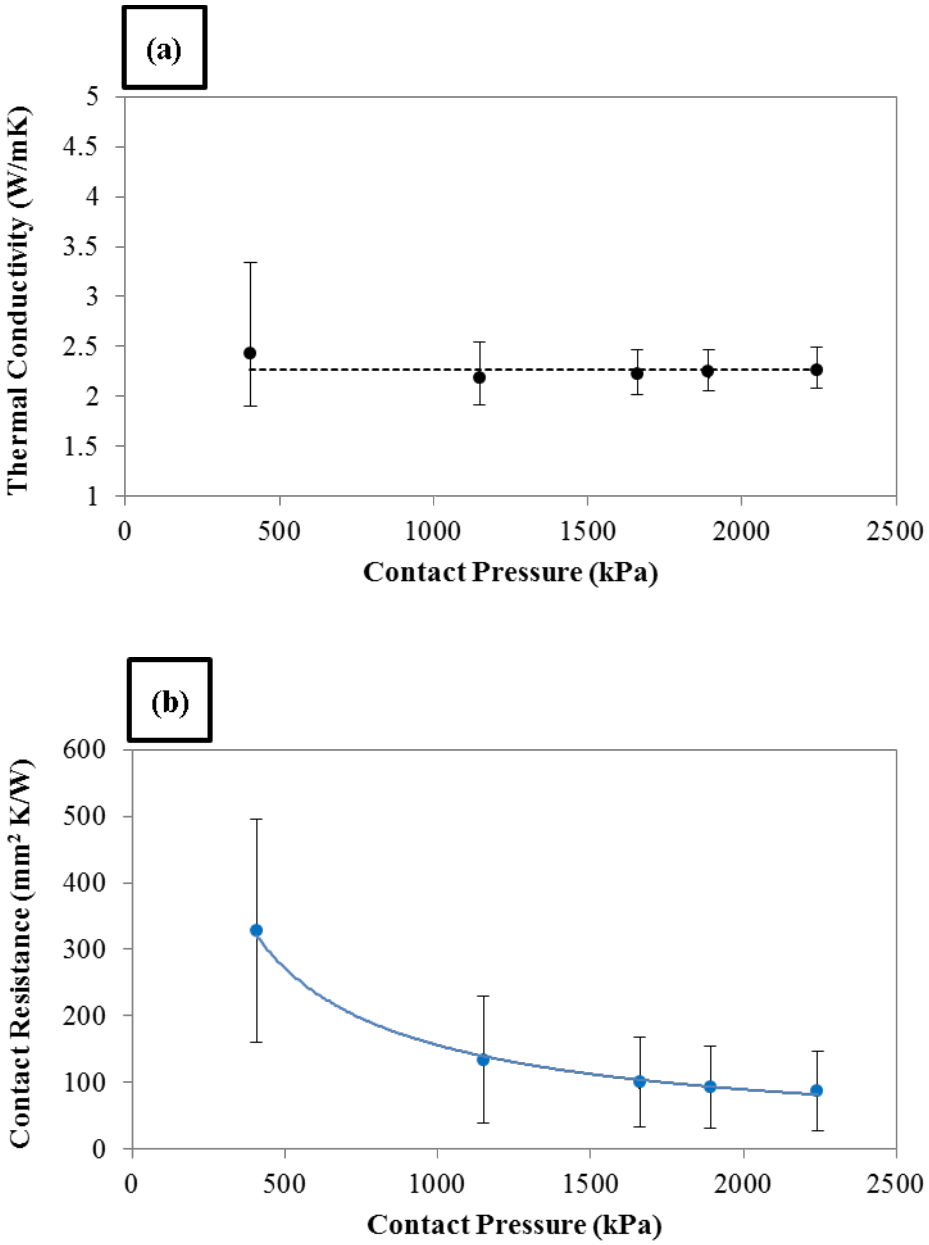

Figure 9.3. (a) Separator thermal conductivity and (b) Separator-heat flux meter contact resistance as a function of contact pressure. Inset: Contact resistance vs. pressure on a log-log scale.

The thermal conductivity of the separator pellets remains constant with interface pressure with a mean value of 2.30 W/mK with a lower and upper bound of 2.08 and 2.49 W/mK, respectively, at an interface pressure of 2250 kPa. As expected, the contact

resistance of the separator pellets with the heat flux meters monotonically decreases with interface. Therefore, the separator pellets are not being affected by the compressive stress that is applied during the measurement, except that the contact with the instrument bars improves.

Thermal conductivity measurements on the Min-K and Fiberfrax board insulation materials were conducted at compressive stresses of 350 and 500 psi with an average material temperature of approximately 55°C. To assess the thermal transport mechanisms across the insulation materials, the samples were tested in both air and vacuum ambient environments. The test sequence was as follows: (i) air at 350 psi, (ii) vacuum at 350 psi, (iii) vacuum at 500 psi, and (iv) air at 500 psi. Figures 9.4 (a)-(d) below shows the linear fits to the measured thermal resistances in air and insulation thicknesses for the aforementioned test sequence. Vacuum data was also obtained but is not shown. The error bars include uncertainties due to thermocouple readings, thermocouple locations, heat flux meter thermal conductivity, tolerances associated with machining the heat flux meters, and estimation in material thickness. With coefficients of determination ranging between 0.86 and 0.99 for the experimental data presented in Figure 9.4, a linear fit properly describes the change in thermal resistance with material thickness. As such, the thermal conductivity of each material can be determined by the inverse slope of the linear fit. The thermal conductivity values for both insulation materials are summarized in Table 9.1 below and are in good agreement with the work of Guidotti et al. [128]. The aforementioned uncertainties were propagated through the linear regression analysis using a boot strapping method to determine the 95% confidence intervals specified in Table 9.1. The distributions

of the estimated thermal conductivity are shown in Figure 9.5 and serve as a visual aid for Table 9.1.

The changes in thermal conductivity with respect to the ambient environment are consistent between the Min-K and Fiberfrax board insulations. When the test chamber is evacuated, the thermal conductivities decrease by 10% and 31%, respectively. However, minimal changes in thermal conductivity occur when the materials are compressed to 500 psi. When air is subsequently introduced into the test chamber to atmospheric pressure, the thermal conductivities increase by 50% and 88%.

The changes in thermal conductivity of the insulation materials suggest that the ambient environment serves a significant role in thermal transport throughout the insulation materials. Depending on the porosity of the insulation materials, thermal transport through the air medium can serve as a parallel pathway for heat transfer. In this sense, the thermal conductivity of the insulation materials is an effective thermal conductivity that comprises of thermal transport through the alumino-silicate (Fiberfrax board) or fumed silica-titania (Min-K) as well as the air medium. In the absence of the latter, thermal transport is relegated only through the solid medium.

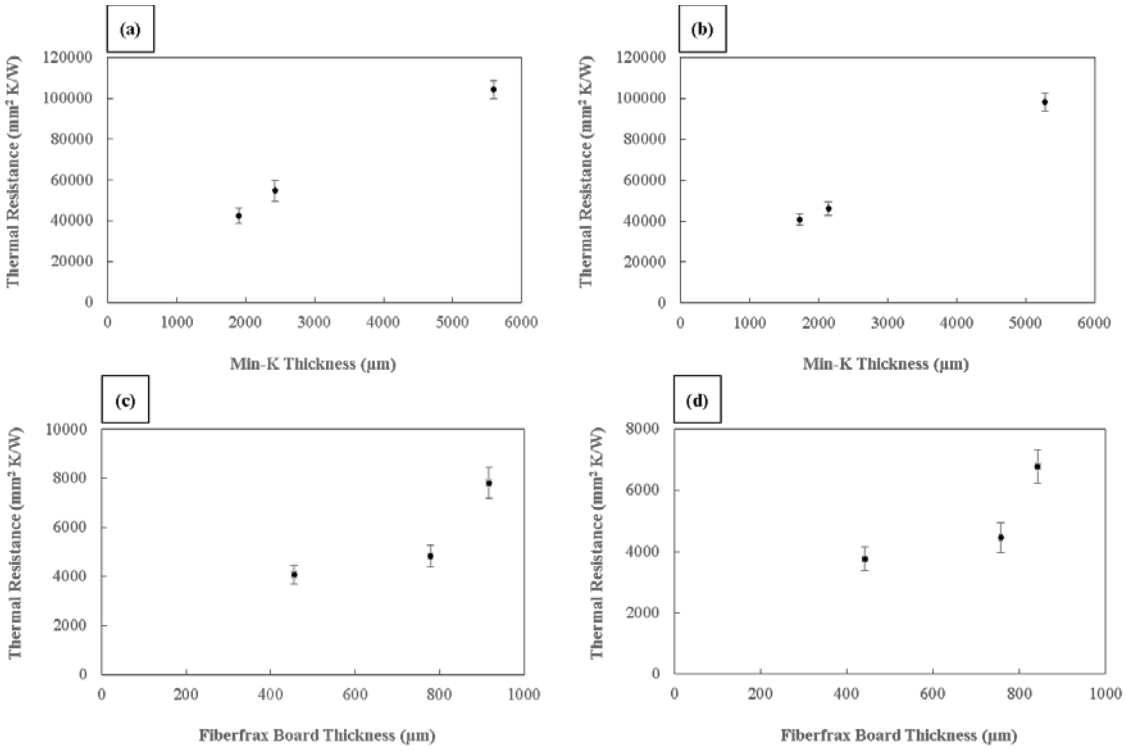

Figure 9.4. Thermal resistance in air as a function of insulation thickness for (a) Min-K at 350 psi, (b) Min-K at 500 psi (c) Fiberfrax board at 350 psi and (d) Fiberfrax board at 500 psi.

Table 9.1. Thermal conductivity (W/mK) of Fiberfrax board and Min-K insulations under different conditions.

k (W/mK)	Min-K		Fiberfrax	
Compressive stress (psi)	**Air**	**Vacuum**	**Air**	**Vacuum**
350	0.061 (0.056, 0.068)	0.043 (0.042, 0.044)	0.141 (0.117, 0.179)	0.097 (0.093, 0.101)
500	0.061 (0.056, 0.067)	0.041 (0.040, 0.042	0.165 (0.132, 0.218)	0.088 (0.085, 0.091)

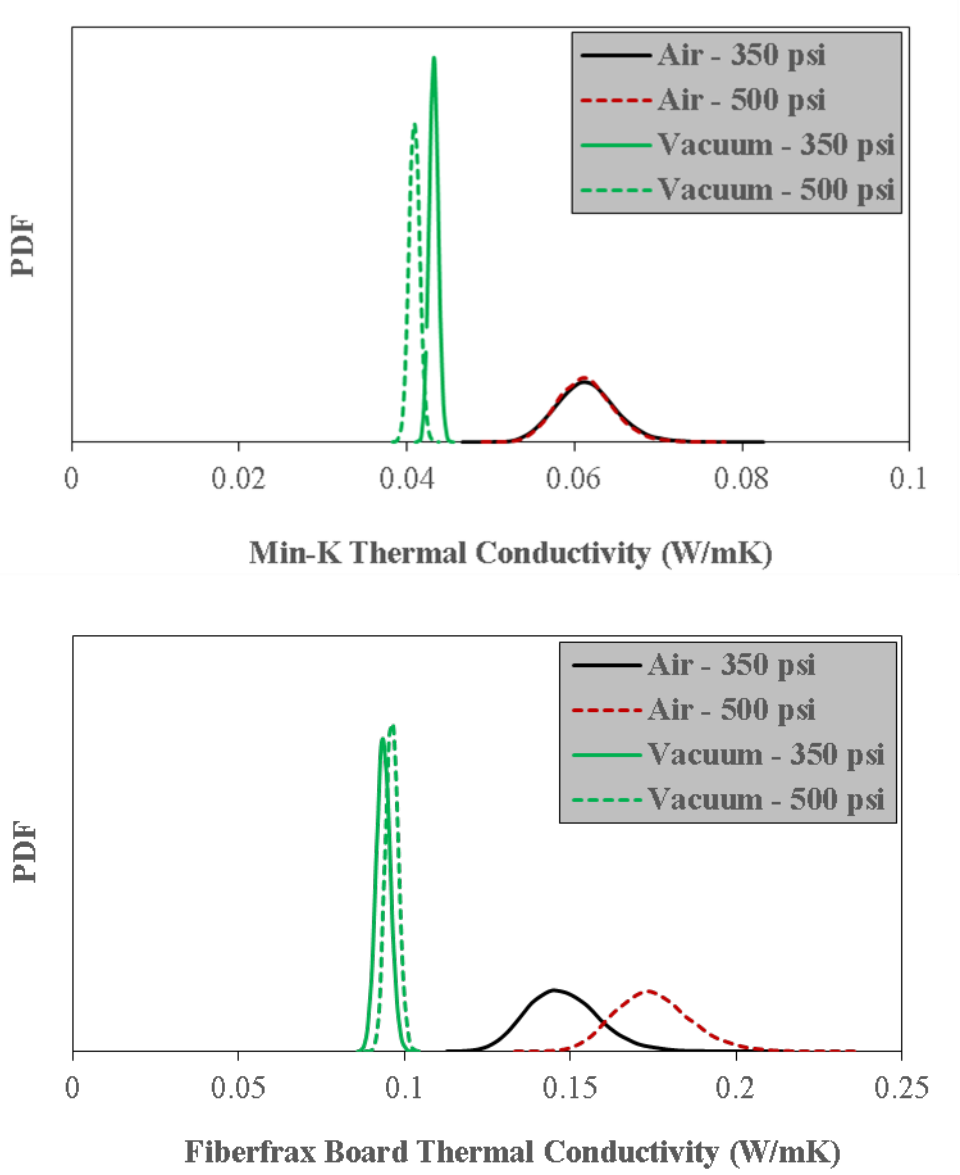

Figure 9.5. Distributions of the estimated thermal conductivity of the Min-K and Fiberfrax insulation materials.

9.4 Conclusions

A steady state reference bar technique was employed to measure the thermal conductivities of the separator pellets (LiCl/MgO/KCl) and thermally insulating materials (Fiberfrax board and Min-K). The separator thermal conductivity was measured to be

approximately 2.30 W/mK and constant within the pressure range of 400 and 2250 kPa. The effective thermal conductivity of the Fiberfrax board and Min-K insulation materials were measured to be on the order of O(0.1) W/mK and O(0.01) W/mK, respectively, at 350 and 500 psi. The thermal conductivities exhibited strong dependence on the ambient environment rather than the compressive stress.

Acknowledgements

Sandia National Laboratories is a multi-program laboratory managed and operated by Sandia Corporation, a wholly owned subsidiary of Lockheed Martin Corporation, for the U.S. Department of Energy's National Nuclear Security Administration under contract DE-AC04-94AL85000.

10. SUMMARY

The overarching theme of this thesis entailed a comprehensive investigation of the viability of CNT TIMs to efficiently conduct heat across two contacting materials. The development of TIMs is necessitated by the temperature drop across the materials arising from macro and microscopic irregularities of their surfaces that constricts heat through small contact regions as well as mismatches in their thermal properties. Similar to other types of TIMs, CNT TIMs alleviate the thermal resistance across the interface by thermally bridging two materials together with cylindrical, high-aspect ratio, and nominally vertical conducting elements. Within the community of TIM engineers, the vision driving the development of CNT TIMs spawned from measurements that revealed impressively high thermal conductivities of individual CNTs. This vision was then projected to efforts focused on packing many individual CNTs on a single substrate that efficiently conduct heat in parallel and ultimately through many contact regions at CNT-to-substrate contacts. The final paragraphs of this dissertation highlight the major contributions of my efforts to improve CNT TIMs, reveal my perspective on their viability, and provide insight to avenues that can potentially pave new pathways for further development.

Similar to other CNT TIM engineers, the efforts in thesis were initially devoted to engaging CNT TIMs with an opposing substrate using various bonding techniques. An innovative bonding technique using Pd thiolate as bonding agent was

developed to not only increase in the contact area between a CNT TIM and opposing substrate but also to assess the performance of CNT TIMs at temperatures up to 250°C. Upon thermolysis, a strong weld between the CNT TIMs and opposing substrate with thermalized Pd thiolate as a medium was created and a significant reduction in the thermal resistance was observed. The reduction in thermal resistance is likely due to a transition from a van der Waals type bond between the CNT TIM and opposing substrate to a more covelant-like bond resulting from the welded joint. The bonded structure also exhibited thermal stability up to 250°C.

Alternatively, the engagement of a CNT TIM with an opposing substrate can also be improved by inserting a solder foil between the CNT TIM and opposing substrate and subsequently raising the temperature of the interface above the eutectic point of the solder foil. This bonding technique creates a strong weld that not only reduces the thermal resistance significantly but also minimizes the change in thermal resistance with an applied compressive load. The latter is an indication that the contact area between the CNT TIM and opposing substrate is maximized. With the contact area maximized, the thermal resistance can be further reduced by infiltrating the CNT TIM with paraffin wax, which serves as an alternate pathway for heat conduction across the interface that ultimately reduces the bulk resistance of the CNT TIM. Thus, infiltrating CNT TIMs with another material provides an avenue for modulating their effective thermal conductivity.

Within the CNT TIM height range of 1 to 50 μm, the bulk resistance of CNT TIMs scales linearly with height and can alternatively be modulated by adjusting the as-grown height. The linear relationship between thermal resistance and CNT TIM height provides

a simple and efficient methodology to estimate the contact resistance and effective thermal conductivity of CNT TIMs grown in our deposition system. In this thesis, the contact resistance and effective thermal conductivity were estimated using two measurement techniques: (i) one-dimensional, steady-state reference bar and (ii) photoacoustic technique. The contact resistance of CNT TIMs estimated using the reference bar rig were greater than the contact resistance of CNT TIM estimated using the photoacoustic technique by approximately a factor of three. This discrepancy is due to poor engagement between the rigid and macroscopically irregular surface of the heat flux meters used in the reference bar rig relative to the flexible and smoother surface of the Ag foil used in the photoacoustic technique. Using both measurement techniques, the effective thermal conductivity was estimated to be on the order of O(1 W/mK). Additionally, the effective thermal conductivity decreased as the CNT TIMs were compressed, which indicates that heat conduction within CNT TIMs is dependent upon the nature in which they mechanically deform (i.e., stiffening due to CNT-to-CNT contacts and localized strain due to buckling).

Currently, the major limitations of CNT TIMs are the quality and mass density at which they can be synthesized and further development will rely on our ability to increase both of these quantities to improve their conductive attributes. The quality of CNTs can be improved by developing catalyst layers that not only control the diffusion of carbon into the catalyst particle and growth rate but also form uniformly-shaped, hemispherical catalyst particles that dictate the morphology of CNTs. Furthermore, by investigating the balance between the surface energies of catalyst particles and underlying surfaces, we can develop catalyst layers that increase the number of nucleation sites for CNT growth on a given

substrate and increase the quantity of CNTs that participate in thermal transport. An alternative method to increase the mass density of CNT TIMs is to decorate the array with graphitic petals that not only repair individual CNTs but also strongly connects adjacent CNTs covalently rather than by weak van der Waals interactions. However, the development of methods to flatten the stiff graphitic petals protruding through the top of the array is imperative to properly engage the CNT-petal TIM to the opposing substrate.

LIST OF REFERENCES

LIST OF REFERENCES

[1] C. V. Madhusudana, 1995, Thermal Contact Conductance, Springer-Verlag, New York, NY.

[2] Berquist, Technical Data Sheet for Thermal Pads, www.bergquistcompany.com.

[3] W. Haller et al., 2007, Adhesives, Ullmann's Encyclopedia of Industrial Chemistry 7th Edition, Wiley, New York, NY.

[4] Indium Corporation, Thermal K Values List, http://www.indium.com/thermal-management/thermal-k-list/.

[5] H. Cui, O. Zhou, and B. R. Stoner, 2000, "Deposition of Aligned Bamboo-Like Carbon Nanotubes via Microwave Plasma Enhanced Chemical Vapor Deposition," *Journal of Applied Physics*, **88**(10), pp. 6072 - 6074.

[6] L. C. Qin, D. Zhou, A. R. Krauss, and D. M. Gruen, 1998, "Growing Carbon Nanotubes by Microwave Plasma-Enhanced Chemical Vapor Deposition," *Applied Physics Letters*, **72**(26), pp. 3437 - 3439.

[7] C. Bower, O. Zhou, W. Zhu, D. J. Werder, and S. H. Jin, 2000, "Nucleation and Growth of Carbon Nanotubes by Microwave Plasma Chemical Vapor Deposition," *Applied Physics Letters*, **77**(17), pp. 2767 - 2769.

[8] M. M. J. Treacy, T. W. Ebbesen, and J. M. Gibson, 1996, "Exceptionally High Young's Modulus Observed for Individual Carbon Nanotubes," *Nature*, **381**(20), pp. 678 – 680.

[9] P. Poncharal, Z. L. Wang, D. Ugarte, and W. A. de Heer, 1999, "Electrostatic Deflections and Electromechanical Resonances of Carbon Nanotubes," *Science*, **283**(5407), pp. 1513 – 1516.

[10] P. Kim, L. Shi, A. Majumdar, and P. L. McEuen, 2001, "Thermal Transport Measurements of Individual Multiwalled Nanotube," *Physical Review Letters*, **87**(21), pp. 215502-1 – 215502-4.

[11] S. Berber, Y.-K. Kwan, and D. Tomanek, 2000, "Unusually High Thermal Conductivity of Carbon Nanotubes," *Physical Review Letters*, **84**(20), pp. 4613 - 4616.

[12] A. A. Zbib, S. Dj. Mesarovic, E. T. Lilleodden, D. McClain, J. Jiao, and D. F. Bahr, 2008, "The Coordinated Buckling of Carbon Nanotube Turfs under Uniform Compression," *Nanotechnology*, **19**(17), pp. 175704-1 – 175704-7.

[13] S. Dj. Mesarovic, C. M. McCarter, D. F. Bahr, H. Radhakrishnan, R. F. Richards, C. D. Richards, D. McClain, and J. Jiao, 2006, "Mechanical Behavior of a Carbon Nanotube Turf," *Scripta Materialia*, **56**(2), pp. 157 – 160.

[14] M. R. Maschmann, 2015, "Integrated Simulation of Active Carbon Nanotube Forest Growth and Mechanical Compression," *Carbon*, **86**, pp. 26 – 37.

[15] X. Q. He, S. Kitipornchai, and K. M. Liew, 2005, "Buckling Analysis of Multi-Walled Carbon Nanotubes: A Continuum Model Accounting for van der Waals Interaction," *Journal of Mechanics and Physics of Solids*, **53**(2), pp. 303 – 326.

[16] T. Fukuda, F. Arai, and L. Dong, 2003, "Assembly of Nanodevices with Carbon Nanotubes Through Nanorobotic Manipulations," *Proceedings of the IEEE*, **91**(11), pp. 1803 – 1818.

[17] C. Bower, R. Rosen, L. Jin, J. Han, and O. Zhou, 1999, "Deformation of Carbon Nanotubes in Nanotube-Polymer Composites," *Applied Physics Letters*, **74**(22), pp. 3317 – 3319.

[18] A. Pantano, M. C. Boyce, and D. M. Parks, 2003, "Nonlinear Structural Mechanics Based Modeling of Carbon Nanotube Deformation," *Physical Review Letters*, **91**(14), pp. 145504-1 – 145504-4.

[19] M. R. Maschmann, G. J. Ehlert, S. J. Park, D. Mollenhauer, B. Maruyama, A. J. Hart, and J. W. Baur, 2012, "Visualizing Strain Evolution and Coordinated Buckling within CNT Arrays by *in situ* Digital Image Correlation," *Advanced Functional Materials*, **22**, pp. 4686 – 4695.

[20] M. R. Maschmann, Q. Zhang, R. Wheeler, F. Du, L. Dai, and J. Baur, 2011, "*In Situ* SEM Observation of Column-like and Foam-like CNT Nanoindentation," ACS *Applied Materials and Interfaces*, **3**(3), pp. 648 - 653.

[21] M. R. Maschmann, Q. Zhang, F. Du, L. Dai, and J. Baur, 2011, "Length Dependent Foam-like Mechanical Response of Axially Indented Vertically Oriented Carbon Nanotube Arrays," *Carbon*, **49**(2), pp. 386 - 397.

[22] S. B. Hutchens, L. J. Hall, and J. R. Greer, 2010, "*In situ* Mechanical Testing Reveals Periodic Buckle Nucleation and Propagation in Carbon Nanotube Bundles," *Advanced Functional Materials*, **20**, pp. 2338 – 2346.

[23] P. P. S. S. Abadi, M. R. Maschmann, S. M. Mortuza, S. Banerjee, J. W. Baur, S. Graham, and B. A. Cola, 2014, "Reversible Tailoring of Mechanical Properties of Carbon Nanotube Forests by Immersing in Solvents," *Carbon,* **69**, pp. 178 – 187.

[24] P. P. S. S. Abadi, S. B. Hutchens, J.R. Greer, B. A. Cola, and S. Graham, 2012, "Effects of Morphology on the Micro-Compression Response of Carbon Nanotube Forests," *Nanoscale*, **4**(11), pp. 3373 - 3380.

[25] P. P. S. S. Ababi, S. B. Hutchens, J. R. Greer, B. A. Cola, and S. Graham, 2013, "Buckling-Driven Delamination of Carbon Nanotube Forests," *Applied Physics Letters*, **102**(22), pp. 223103-1 – 223103-5.

[26] M. J. Biercuk, M. C. Llanguno, M. Radosavljevic, J. K. Hyun, A. T. Johnson, and J. E. Fischer, 2002, "Carbon Nanotube Composites for Thermal Management," *Applied Physics Letters*, **80**(15), pp. 2767 - 2769.

[27] M. A. Panzer, G. Zhang, D. Mann, X. Hu, E. Pop, H. Dai, and K. E. Goodson, 2008, "Thermal Properties of Metal-Coated Vertically Aligned Single-Wall Nanotube Arrays," ASME *Journal of Heat Transfer*, **130**, pp. 052401-1 – 052401-9.

[28] J. Xu and T. S. Fisher, 2006, "Enhanced Thermal Contact Conductance using Carbon Nanotube Array Interfaces," *IEEE Transactions on Components Packaging Technologies*, **29**(2), pp 261 - 267.

[29] J. Xu and T. S. Fisher, 2006, "Enhancement of Thermal Interface Materials with Carbon Nanotube Arrays," *International Journal of Heat and Mass Transfer*, **49**, pp 1658 - 1666.

[30] T. Tong, Y. Zhao, L. Delzeit, A. Kashani, M. Meyyappan, and A. Majumdar, 2007, "Dense Vertically Aligned Multiwalled Carbon Nanotube Arrays as Thermal Interface Materials," *IEEE Transactions on Components Packaging Technologies*, **30**(1), pp. 92 - 99.

[31] X. Hu, L. S. Pan, G. Gu, and K. E. Goodson, 2009, "Superior Thermal Interfaces Made by Metallically Anchored Carbon Nanotube Arrays," *Proceedings of ASME Summer Heat Transfer Conference, San Francisco, CA*, InterPACK2009-89375.

[32] B. A. Cola, J. Xu, C. Cheng, H. Hu, X. Xu, and T. S. Fisher, 2007, "Photoacoustic Characterization of Carbon Nanotube Array Interfaces," *Journal of Applied Physics*, **101**(5), pp. 054313-1 – 054313-9.

[33] B. A. Cola, X. Xu, and T. S. Fisher, 2007, "Increased Real Contact in Thermal Interfaces: A Carbon Nanotube/foil Material," *Applied Physics Letters*, **90**(9), pp. 093513-1 – 093513-3.

[34] T. L. Bougher, C. J. Vasquez, B. A. Cola, 2014, "Thermal Conductivity Measurement of Bare Carbon Nanotube Films Using the Photoacoustic Technique," *Proceedings of the 15th International Heat Transfer Conference, Koyto, Japan*, IHTC15-9607.

[35] B. A. Cola, S. L. Hodson, X. Xu, and T. S. Fisher, 2008, "Carbon Nanotube Array Thermal Interfaces Enhanced with Paraffin Wax," *Proceedings of ASME Summer Heat Transfer Conference, Jacksonville, FL*, HT2008-56483.

[36] B. A. Cola, M. A. Capano, P. B. Amama, X. Xu, and T. S. Fisher, 2008, "Carbon Nanotube Array Thermal Interfaces for High-Temperature Silicon Carbide Devices," *Nanoscale and Microscale Thermophysical Engineering*, **12**, pp. 228 - 236.

[37] B. A. Cola, P. B. Amama, X. Xu, and T. S. Fisher, 2008, "Effects of Growth Temperature on Carbon Nanotube Array Thermal Interfaces," *ASME Journal of Heat Transfer*, **130**, pp. 114503-1 – 114503-4.

[38] S. L. Hodson, T. Bhuvana, B. A. Cola, X. Xu, G. U. Kulkarni, T. S. Fisher, "Palladium Thiolate Bonding of Carbon Nanotube Thermal Interfaces," *Journal of Electronic Packaging*, **133**(2), pp. 020907-1 – 020907-6.

[39] J. H. Taphouse, O. L. Smith, S. R. Marder, and B. A. Cola, 2014, "A Pyrenylpropyl Phosphonic Acid Surface Modifier for Mitigating the Thermal Resistance of Carbon Nanotube Contacts", *Advanced Functional Materials*, **24**, pp. 465 – 471.

[40] A. M. Marconnet, M. A. Panzer, and K. E. Goodson, 2013, “Thermal Conduction Phenomena in Carbon Nanotubes and Related Nanostructured Materials”, *Reviews of Modern Physics*, **85**(3), pp. 1296 - 1327.

[41] B. A. Cola, J. Xu, and T. S. Fisher, 2009, “Contact Mechanics and Thermal Conductance of Carbon Nanotube Array Interfaces,” *International Journal of Heat and Mass Transfer*, **52**, pp. 3490 – 3503.

[42] C. M. van Wyk, 1946, “Note on the Compressibility of Wool,” *Journal of the Textile Institute Transactions,* **37**, pp. 285 – 292.

[43] Y. Son, S. K. Pal, T. Borca-Tascuic, P. M. Ajayan, R. W. Siegel, 2008, “Thermal Resistance of the Native Interface Between Vertically Aligned Multiwalled Carbon Nanotube Arrays and Their SiO_2/Si Substrate,” *Journal of Applied Physics*, **103**(2), pp. 024911-1 – 024911-7.

[44] D.-J. Yang, Q. Zhang, G. Chen, S. F. Yoon, J. Ahn, S. G. Wang, Q. Zhou, Q. Wang, and J. Q. Li, 2002, "Thermal Conductivity of Multiwalled Carbon Nanotubes," *Physical Review B*, **66**(16), pp. 165440-1 – 165440-6.

[45] X. Wang, Z. Zhong, and J. Xu, 2005, "Noncontact Thermal Characterization of Multiwall Carbon Nanotubes," *Journal of Applied Physics*, **97**(6), pp. 064302-1 – 064302-5.

[46] Y. Xu, Y. Zhang, E. Suhir, and X. W. Wang, 2006, “Thermal Properties of Carbon Nanotube Array Used for Integrated Circuit Cooling,” *Journal of Applied Physics*, **100**(12), pp. 074302-1 – 074302-5.

[47] A. Okamoto, I. Gunjishima, T. Inoue, M. Akoshima, H. Miyagawa, T. Nakano, T. Baba, M. Tanemura, and G. Oomi, 2011, "Thermal and Electrical Conduction Properties of Vertically Aligned Carbon Nanotubes Produced by Water-Assisted Chemical Vapor Deposition," *Carbon*, **49**(1), pp. 294 - 298.

[48] I. Ivanov, A. Puretzky, G. Eres, H. Wang, Z. W. Pan, H. T Cui, R. Y. Jin, J. Howe, and D. B. Geohegan, 2006, “Fast and Highly Anisotropic Thermal Transport Through Vertically Aligned Carbon Nanotube Arrays,” *Applied Physics Letters*, **89**(22), pp. 223110-1 – 223110-3.

[49] H. Q. Xie, A. Cai, and X. W. Wang, 2007, “Thermal Diffusivity and Conductivity of Multiwalled Carbon Nanotube Arrays,” *Physics Letters A*, **369**(1-2), pp. 120 – 123.

[50] W. Lin, J. Shang, W. Gu, and C. P. Wong, 2012, "Parametric Study of Intrinsic Thermal Transport in Vertically Aligned Multi-Walled Carbon Nanotubes using a Laser Flash Technique," *Carbon*, **50**(4), pp. 1591 - 1603.

[51] M. Akoshima, K. Hata, D. N. Futaba, K. Mizuno, T. Baba, and M. Yumura, 2009, "Thermal Diffusivity of Single-walled Carbon Nanotube Forest Measured by Laser Flash Method," *Japanese Journal of Applied Physics*, **48**(5), pp. 05EC07-1 - 05EC07-6.

[52] X. J. Hu, A. A. Padilla, J. Xu, T. S Fisher, and K. E. Goodson, 2006, "3-Omega Measurements of Vertically Oriented Carbon Nanotubes on Silicon," *Journal of Heat Transfer*, **128**(11), pp. 1109 - 1113.

[53] T. Borca-Tasciuc, S. Vafaei, D. A. Borca-Tasciuc, B. Q. Wei, R. Vajtai, and P. M. Ajayan, 2005, "Anisotropic Thermal Diffusivity of Aligned Multiwall Carbon Nanotube Arrays," *Journal of Applied Physics*, **98**(5), pp. 054309-1 – 054309-6.

[54] M. B. Jakubinek, M. A. White, G. Li, C. Jayasinghe, W. Cho, M. J. Schulz, and V. Shanov, 2010, "Thermal and Electrical Conductivity of Tall, Vertically Aligned Carbon Nanotube Arrays," *Carbon*, **48**(13), pp. 3947 - 3952.

[55] S. K. Pal, Y. Son, T. Borca-Tasciuc, D. A. Borca-Tasciuc, S. Kar, R. Vajtai, and P. A. Ajayan, 2008, "Thermal and Electrical Transport along MWCNT Arrays Grown on Inconel Substrates," *Journal of Materials Research*, **23**(8), pp. 2099 – 2105.

[56] R. S. Prasher, J. X. Xu, Y. Chalopin, N. Minger, K. Lofgreen, S. Volz, F. Cleri, and P. Keblinski, 2009, "Turning Carbon Nanotubes from Exceptional Heat Conductors into Insulators," Phys Rev Lett, 102(10), pp. 105901.

[57] A. M. Marconnet, N. Yamamoto, M. A. Panzer, B. L. Wardle, and K. E. Goodson, 2011, "Thermal Conduction in Aligned Carbon Nanotube-Polymer Nanocomposites with High Packing Density," ACS Nano, **5**(6), pp. 4818 - 4825.

[58] M. T. Pettes and L. Shi, 2009, "Thermal and Structural Characterizations of Individual Single-, Double-, and Multi-Walled Carbon Nanotubes", *Advanced Functional Materials*, **19**, pp. 3918 – 3925.

[59] H. Hu, X. Wang, and X. Xu, 1999, "Generalized Theory of the Photoacoustic Effect in a Multilayer Material," *Journal of Applied Physics*, **86**(7), pp. 3953 - 3958.

[60] N. C. Fernielius, 1980, “Extension of the Rosencwaig-Gersho Photoacoustic Spectroscopy Theory to Include Effects of a Sample Coating,” *Journal of Applied Physics,* **51**(1), pp. 650 – 654.

[61] Y. Fujii, A. Moritani, and J. Nakai, 1981, “Photoacoustic Spectroscopy Theory for Multi-Layered Samples and Interference Effect,” *Japanese Journal of Applied Physics,* **20**(2), pp. 361 - 367.

[62] A. Lachaine and P. Poulet, 1984, “Photoacoustic Measurement of Thermal Properties of a Thin Polyester Film,” *Applied Physics Letters*., **45**(9), pp. 953 – 954.

[63] S. Sankara Raman, V. P. N. Nampoori, C. P. G. Vallabhan, G. Ambadas, and S. Sugunan, 1995, “Photoacoustic Study of the Effect of Degassing Temperature on Thermal Diffusivity of Hydroxyl Loaded Alumina,” *Applied Physics Letters*, **67**(20), pp. 2939 - 2941.

[64] M. Rohde, 1994, “Photoacoustic Characterization of Thermal Transport Properties in Thin Films and Microstructures,” *Thin Solid Films*, **238**(2), pp. 199 - 206.

[65] X. Wang, H. Hu, and X. Xu, 2008, “Photo-Acoustic Measurement of Thermal Conductivity of Thin Films and Bulk Materials,” *ASME Journal of Heat Transfer*, **123**(1), pp. 138 - 144.

[66] X. Wang, B. A. Cola**,** T. L. Bougher**,** S. L. Hodson, T. S. Fisher, and X. Xu, 2013, “Photoacoustic Technique for Thermal Conductivity and Thermal Interface Measurements,” *Annual Review of Heat Transfer*, **16**, pp. 135 - 157.

[67] J. Wasniewski, D. Altman, S. L. Hodson, T. S. Fisher, A. Bulusu, S. Graham, B. A. Cola, “Characterization of Metallically Bonded Carbon Nanotube-Based Thermal Interface Materials Using a High Accuracy 1D Steady-State Technique,” *Journal of Electronic Packaging*, **134**(2), pp. 020901-1 – 020901-7.

[68] G. Carotenuto, B. Martorana, P. Perlo, and L. Nicolais, 2003, "A Universal Method for the Synthesis of Metal and Metal Sulfide Clusters Embedded in Polymer Matrices," *Journal of Materials Chemistry*, **13**(12), pp. 2927 – 2930.

[69] P. J. Thomas, A. Lavanya, V. Sabareesh and G. U. Kulkarni, 2001, "Self-Assembling Bi-layers of Palladium Thiolates in Organic Media," *Proceedings of the Indian Academy of Sciences-Chemical Sciences,* **113**(5-6), pp. 611 - 619.

[70] T. Bhuvana and G. U. Kulkarni, 2008, "Highly Conducting Patterned Pd Nanowires by Direct-Write Electron Beam Lithography," *ACS Nano,* **2**(3), pp 457 - 462.

[71] J. V. Zoval, P. R. Biernacki, and R. M. Penner, 1996, "Implementation of Electrochemically Synthesized Silver Nanocrystallites for Preferential SERS Enhancement of Defect Modes on Thermally Etched Graphite Surfaces," *Analytical Chemistry*, **68**(9), pp. 1585 - 1592.

[72] Y. Lin, K. A. Watson, M. J. Fallbach, S. Ghose, J. G. Smith, Jr., D. M. Delozier, W. Cao, R. E. Crooks, and J. W. Connell, 2009, "Rapid, Solventless, Bulk Preparation of Metal Nanoparticle-Decorated Carbon Nanotubes," *ACS Nano,* **3**(4), pp. 871 - 884.

[73] S. Frank, P. Poncharal, Z. L. Wang, W. A. de Heer, 1998, "Carbon Nanotube Quantum Resistors," *Science*, **280**(5370), pp. 1744.

[74] Q. Ngo, D. Petranovic, S. Krishnan, A. M. Cassell, Q. Ye, J. Li, M. Meyyappan, and C. Y. Yang, 2004, "Electron Transport Through Metal-Multiwall Carbon Nanotube Interfaces," *IEEE Transactions on Nanotechnology*, **3**(2), pp. 311 - 317.

[75] D. Mann, A. Javey, J. Kong, Q. Wang, and H. Dai, 2003, "Ballistic Transport in Metallic Nanotubes with Reliable Pd Ohmic Contacts," *Nano Letters,* **3**(11), pp. 1541 - 1544.

[76] Y. Matsuda, W. Deng, and W. A. Goddard, 2007, "Contact Resistance Properties Between Nanotubes and Various Metals from Quantum Mechanics," *Journal of Physical Chemistry. C*, **111**(11), pp. 11113 - 11116.

[77] J. C. Claussen, A. D. Franklin, A. Haque, D. M. Porterfield, and T. S. Fisher, 2009, "Electrochemical Biosensor of Nanocube-Augmented Carbon Nanotube Networks," *ACS Nano,* **3**(1), pp. 37 - 44.

[78] V. Georgakilas, D. Gournis, V. Tzitzios, L. Pasquato, D. M. Guldi, and M. Prato, 2007, "Decorating Carbon Nanotubes with Metal or Semiconductor Particles," *Journal of Materials Chemsitry,* **17**, pp. 2679 - 2694.

[79] G. G. Wildgoose, C. E. Banks, and R. G. Compton, 2006, "Metal Nanoparticles and Related Materials Supported on Carbon Nanotubes: Methods and Applications," *Small,* **2**(2), pp. 182 - 193.

[80] R. Voggu, S. Pal, S. K. Pati, and C. N. R. Rao, 2008, "Semiconductor to Metal Transition in SWNTs Caused by Interaction with Gold and Platinum Nanoparticles," *Journal of Physics: Condensed Matter*, **20**(21), pp. 215211-1 – 215211-6.

[81] A. Javey, J. Guo, Q. Wang, M. Lundstrom, and H. Dai, 2003, "Ballistic Carbon Nanotube Field-Effect Transistors," *Nature*, **424**, pp. 654 - 657.

[82] N. Nemec, D. Tomanek, and G. Cuniberti, 2006, "Contact Dependence of Carrier Injection in Carbon Nanotubes: An *Ab Initio* Study," *Physical Review Letters*, **96**(7), pp. 076802-1 – 076802-4.

[83] M. R. Maschmann, P.B. Amama, A. Goyal, Z. Iqbal, and T.S. Fisher, 2006, "Freestanding Vertically Oriented Single-Walled Carbon Nanotubes Synthesized using Microwave Plasma-Enhanced CVD," *Carbon*, **44**, pp. 2758 - 2763.

[84] J. Tersoff, 1999, "Contact Resistance of Carbon Nanotubes," *Applied Physics Lett*ers, **74**(15), pp. 2122 - 2124.

[85] M. P. Anantram, S. Datta, and Y. Xue, 2000, "Coupling of Carbon Nanotubes to Metallic Contacts," *Physical Review B*, **61**(20), pp. 219 - 224.

[86] K. Matthews, B. A. Cruden, B. Chen, M. Meyyappan, and L. Delzeit, 2002, "Plasma-Enhanced Chemical Vapor Deposition of Multiwalled Carbon Nanofibres," *Journal of Nanoscience and Nanotechnology*, **2**(5), pp. 475 - 480.

[87] P. B. Amama, B. A. Cola, T. D. Sands, X. Xu, and T. S. Fisher, 2007, "Dendrimer-Assisted Controlled Growth of Carbon Nanotubes for Enhanced Thermal Interface Conductance," *Nanotechnology*, **18**(38), pp. 385303-1 – 385303-4.

[88] P. Delaney and M. D. Ventra, 1999, "Comment on 'Contact Resistance of Carbon Nanotubes'", *Applied Physics Letters.*, **75**(25), pp. 4028 - 4029.

[89] B. Khare, M. Meyyappan, M. H. Moore, P. Wilhite, H. Imanaka, B. Chen, 2003, "Proton Irradiation of Carbon Nanotubes," *Nano Letters*, **3**(5), pp. 643 – 646.

[90] A. V. Krasheninnikov and K. Nordlund, 2004, "Irradiation Effects in Carbon Nanotubes," *Nuclear Instruments and Methods in Physics Research Section B: Beam Interactions with Materials and Atoms*, **216**, pp. 355 – 366.

[91] A. Kis, G. Csányi, J.-P. Salvetat, T.-N. Lee, E. Couteau, A. J. Kulik, W. Benoit, J. Brugger, and L. Forró, 2004, "Reinforcement of Single-Walled Carbon Nanotube Bundles by Intertube Bridging," *Nature Materials*, **3**(3), pp. 153 – 157.

[92] V. Skákalová, M. Hulman, P. Fedorko, P. Lukác, and S. Roth, 2003, "Effect Of Gamma-Irradiation on Single-Wall Carbon Nanotube Paper," *AIP Conference Proceedings, Kirchberg, Tirol*, pp. 143 – 147.

[93] J. Guo, Y. Li, S. Wu, and W. Li, 2005, “The Effects of Gamma-Irradiation Dose on Chemical Modification of Multi-Walled Carbon Nanotubes.,” *Nanotechnology*, **16**(10), pp. 2385 – 2388.

[94] Z. Xu, L. Chen, L. Liu, X. Wu, and L. Chen, 2011, “Structural Changes in Multi-Walled Carbon Nanotubes Caused by γ-ray Irradiation,” *Carbon*, **49**(1), pp. 350 – 351.

[95] M. Miao, S. C. Hawkins, J. Y. Cai, T. R. Gengenbach, R. Knott, and C. P. Huynh, 2011, “Effect of Gamma-Irradiation on the Mechanical Properties of Carbon Nanotube Yarns,” *Carbon*, **49**(14), pp. 4940 – 4947.

[96] S. D. M. Brown, A. Jorio, P. Corio, M. S. Dresselhaus, G. Dresselhaus, R. Saito, and K. Kneipp, 2001, "Origin of the Breit-Wigner-Fano Lineshape of the Tangential G-Band Feature of Metallic Carbon Nanotubes," *Physical Review B*, **63**(15), pp. 155414-1 – 155414-8.

[97] H. M. Heise, R. Kuckuk, A. K. Ojha, A. Srivastava, V. Srivastava, B. P. Asthana, 2009, “Characterisation of Carbonaceous Materials Using Raman Spectroscopy: A Comparison of Carbon Nanotube Filters, Single- and Multi-Walled Nanotubes, Graphitised Porous Carbon and Graphite,” *Journal of Raman Spectroscopy*, **40**(3), pp. 344 – 353.

[98] B. Efron, 1992, Bootstrap Methods: Another Look at the Jackknife, Breakthroughs in Statistics, pp. 569 – 593.

[99] B. Efron and R. Tibshirani, “Statistical Data Analysis in the Computer Age,” *Science*, **253**(5018), pp. 390 – 395.

[100] N. Urkainczyk, S. Kurajica, J. Sipusic, 2010, “Thermophysical Comparison of Five Paraffin Waxes as Latent Heat Storage Materials,” *Chemical and Biochemical Engineering Quarterly*, **24**(2), pp. 129 – 137.

[101] R. A. Sayer, S. L. Hodson, T. Koehler, R. Cordova, T. Marinone, J. Serrano, and T. S. Fisher, 2014, “Characterization of Gamma-Irradiated Carbon Nanotube and Metallic Thermal Interface Materials for Space Systems,” *International Journal of Micro-Nano Scale Transport*, **5**(2), pp. 81 - 93.

[102] S. Sadasivam, S. L. Hodson, M. R. Maschmann, 2015, “Combined Microstructure and Heat Transfer Modeling of Carbon Nanotube Thermal Interface Materials,” *Journal of Heat Transfer*, **138**(4), pp. 042402-1 – 042402-12.

[103] Intel Corporation, 2009, Intel Core 2 Extreme Quad-Core Processor and Intel Core 2 Quad Processor, Thermal and Mechanical Design Guidelines.

[104] A. Y. Cao, P. L. Dickrell, W. G. Sawyer, M. N. Ghasemi-Nejhad, P. M. Ajayan, 2005, "Super-Compressible Foamlike Carbon Nanotube Films," *Science*, **310**(5752), pp. 1307 - 1310.

[105] L. Gong, S. Kyriakides, W. Y. Jang, 2005, "Compressive Response of Open-Cell Foams. Part I: Morphology and Elastic Properties," *International Journal of Solids and Structures*, **42**(5-6), pp. 1355 - 1379.

[106] M. Hodes, R. Zhang, L. S. Lam, R. Wilcoxon, and N. Lower, 2014, "On the Potential of Galinstan-Based Minichannel and Minigap Cooling," *IEEE Transactions on Components, Packaging, and Manufacturing Technology*, **4**(1), pp. 46 – 56.

[107] J. H. Taphouse, T. L. Bougher, V. Singh, P.P.S. Abadi, S. Graham, and B. A. Cola, 2013, "Carbon Nanotube Thermal Interfaces Enhanced with Spray on Nanoscale Polymer Coatings," *Nanotechnology*, **24**(10), pp. 105401-1 – 105401-8.

[108] Z. Huang, T. S. Fisher, and J. Murthy, 2011, "An Atomistic Study of the Thermal Conductance Across a Metal-Graphene Nanoribbon Interface," *Journal of Applied Physics*, **109**(7), pp. 074305-1 – 074304-10.

[109] C.-W. Nan, G. Liu, Y. Lin, and M. Li, 2004, "Interface Effect on Thermal Conductivity of Carbon Nanotube Composites," *Applied Physics Letters*, **85**(16), pp. 3549 – 3551.

[110] N. Na, K. Hasegawa, X. Zhou, M. Nihei, and S. Noda, 2015, "Denser and Taller Carbon Nanotube Arrays on Cu Foils Usable as Thermal Interface Materials," *Japanese Journal of Applied Physics*, **54**(9), pp. 095102-1 – 095102-7.

[111] A. N. Volkov, T. Shiga, D. Nicholson, J. Shiomi, L. V. Zhigilei, 2012, "Effect of Bending Buckling of Carbon Nanotubes on Thermal Conductivity of Carbon Nanotube Materials," *Journal of Applied Physics*, **111**(5), pp. 053501-1 – 053501-11.

[112] A. E. Aliev, M. H. Lima, E. M. Silverman, and R. H. Baughman, 2010, "Thermal Conductivity of Multi-Walled Carbon Nanotube Sheets: Radiation Losses and Quenching of Phonon Modes," *Nanotechnology*, **21**(3), pp. 035709-1 – 035709-11.

[113] S. V. Garimella et al., 2008, Thermal Challenges in Next-Generation Electronic Systems, *IEEE Transactions on Components and Technologies*, **31**(4), pp. 801 – 815.

[114] T. Favaloro, A. Ziabari, J. H. Bahk, P. Burke, H. Lu, J. Bowers, A. Gossard, Z. Bian, and A. Shakouri, 2014, "High Temperature Thermoreflectance Imaging and Transient Harman Characterization of Thermoelectric Energy Conversion Devices," *Journal of Applied Physics*, **16**(3), pp. 034501-1 – 034501-9.

[115] Arctic Silver, Arctic Silver 5, http://www.arcticsilver.com/as5.htm.

[116] Indium Corporation, Gold Solders Technical Document, http://www.indium.com/solders/gold/#whitepapers.

[117] D. Bom, R. Andrews, D. Jacques, J. Anthony, B. Chen, M. S. Miller, and J. P Selegue, 2002, "Thermogravimetric Analysis of the Oxidation of MultiWalled Carbon Nanotubes: Evidence for the Role of Defect Sites in Carbon Nanotube Chemistry," *Nanoletters*, **2**(6), pp. 615 – 619.

[118] J. Zhao, Y. Zhang, Y. Su, X. Huang, L. Wei, E. S-W. Kong, and Y. Zhang, 2012, "Structural Improvement of CVD Multi-Walled Carbon Nanotubes by a Rapid Annealing Process," *Diamond & Related Materials*, **25**, pp. 24 – 28.

[119] L. Vozar and W. Hohenauer, 2003/2004, "Flash Method of Measuring Thermal Diffusivity – A Review," *High Temperature and High Pressures*, **35/36**(3), pp. 253 - 264.

[120] S. F. Corbin and D. M. Turriff, 2012, Thermal Diffusivity by the Laser Flash Technique, Characterization of Materials, Wiley, New York, NY.

[121] Q. A. Acton, 2012, Advances in Nanotechnology Research and Application, Scholarly Editions, Atlanta, GA.

[122] ASTM Committee D09, Standard Test Method for Thermal Transmission Properties of Thermally Conductive Electrical Insulation Material, Annual B ASTM Standard, pp. D5470–06, 2011.

[123] S. L. Hodson, R. A. Sayer, and T. W. Grasser, 2014, "Thermal Contact Resistance Measurements at Elevated Temperatures," *HI TEMP Conference, Santa Fe, NM*, Poster.

[124] S. L. Hodson, Q. E. Sneed, T. S. Fisher, T. W. Grasser, and R. A. Sayer, 2015, "Thermal Contact Resistance Measurements at Elevated Temperatures," *ASME 2015 International Mechanical Engineering Congress & Exposition, Houston, TX*, Poster.

[125] M. Hao, Z. Huang, K. R. Saviers, G. Xiong, S. L. Hodson, and T. S. Fisher, "Characterization of Vertically Oriented Carbon Nanotube Arrays as High-Temperature Thermal Interface Materials," *International Journal of Heat and Mass Transfer*, in press.

[126] Y. Wang, X. Ruan, and A. K. Roy, 2012, "Two-Temperature Nonequilibrium Molecular Dynamics Simulation of Thermal Transport Across Metal-Nonmetal Interfaces," *Physical Review B*, **85**(20), pp. 205311-1 – 205311-9.

[127] R. A. Guidotti, F. W. Reinhardt, and T. Kaun, 2002, "Characterization of Small Vacuum Multifoil Containers for a One-Hour Thermal Battery," *Proceedings of the 40th Power Sources Conference, Cherry Hill, NJ*, pp. 299 - 303.

[128] R. A. Guidotti and P. Masset, 2006, "Thermally Activated ("Thermal") Battery Technology Part I: An Overview," *Journal of Power Sources*, **161**(2), pp. 1443 - 1449.

[129] B. L. Trembacki, S. R. Harris, E. S. Piekos, and S. A. Roberts, 2016, "Uncertainty Quantification, Verification, and Validation of a Thermal Simulation Tool for Molten Salt Batteries," *Proceedings of the 47th Power Sources Conference, Orlando, FL.*

VITA

VITA

Stephen Lallana Hodson was born in Los Alamos, New Mexico. Stephen obtained his Bachelor's of Science in Mechanical Engineering from the University of California, Berkeley and Master's of Science in Mechanical Engineering from Purdue University. In December 2016, he is expected to receive his PhD in Mechanical Engineering from Purdue University.

LIST OF PUBLICATIONS

LIST OF PUBLICATIONS

Refereed Journal Papers:

- C. V. Manzano, B. Abad, M. M. Rojo, Y. R. Koh, **S. L. Hodson**, A. M. Lopez Martinez, X. Xu, A. Shakouri, T. D. Sands, T. Borca-Tasciuc, and M. Martin-Gonzalez, "Anisotropic effects on the thermoelectric properties of highly oriented elecrodeposited Bi2Te3 films," Scientific Reports, 6, 19129, 2016.
- S. Sadasivam, **S. L. Hodson**, M. R. Maschmann, and T. S. Fisher, "Combined microsctructure and heat transfer modeling of carbon nanotube thermal interface materials," Journal of Heat Transfer, (in review).
- B. Abad, M. Rull-Bravo, **S. L. Hodson**, X. Xu, and M. Martin-Gonzalez, "Thermoelectric properties of electrodeposited tellurium films and the sodium lignosulfonate effect," Electrochimica Acta, 169, pp. 37-45, 2015.
- A. Kumar, M. R. Maschmann, **S. L. Hodson**, J. Baur, and T. S. Fisher, "Carbon nanotube arrays decorated with multi-layer graphene-nanopetals enhance mechanical strength and durability," Carbon, 84, pp. 236-245, 2015.
- R. A. Sayer, **S. L. Hodson**, T. Koehler, R. Cordova, T. Marinone, J. Serrano, and T. S. Fisher, "Characterization of gamma-irradiated carbon nanotube and metallic thermal interface materials for space systems," *International Journal of Micro-Nano Scale Transport*, 5(2), 2014.
- P. T. McCarthy, K. R. Saviers, **S. L. Hodson**, and T. S. Fisher, "Thermally driven squeezed-film cooling with carbon nanotube-coated gadolinium shuttles," International J. of Heat and Mass Transfer, 78, pp. 1199-1207, 2014.
- K. R. Saviers, **S. L. Hodson**, J. R. Salvador, L. S. Kasten, and T. S. Fisher, "Carbon nanotube arrays for enhanced thermal interfaces to thermoelectric devices," J. Thermophys. Heat Tr., 27(3), pp. 474-481, 2013.
- P. Jha, T. D. Sands, P. Jackson, C. Bomberger, T. Favaloro, **S. L. Hodson**, J. Zide, X. Xu, and A. Shakouri, "Cross-plane thermoelectric transport in p-type $La_{0.67}Sr_{0.33}MnO_3/LaMnO_3$ oxide metal/semiconductor superlattices," J. of Applied Physics, 113(19), 2013.
- J. L. Wasniewski, D. H. Altman, **S. L. Hodson**, T. S. Fisher, A. Bulusu, S. Graham, and B. A. Cola, "Characterization of metallically bonded carbon nanotube-based thermal interface materials using a high accuracy 1D steady-state technique," J. of Electronic Packaging, 134(2), 2012.

- L. Guo, **S. L. Hodson**, T. S. Fisher, and X. Xu, "Heat transfer across metal-dielectric interfaces during ultrafast-laser heating," J. of Heat Transfer, 134(4), 2012.
- A. Snyder, Z. Y. Bo, **S. L. Hodson**, T. S. Fisher, and L. A. Stanciu, "The effect of heating rate and composition on the properties of spark plasma sintered zirconium diboride based composites," Materials Sci. and Eng. A – Structural Mat. Prop. Microstrucure and Processing, 538, pp. 98-102, 2012.
- **S. L. Hodson**, T. Bhuvana, B. A. Cola, X. Xu, G.U. Kulkarni, and T. S. Fisher, "Palladium thiolate bonding of carbon nanotube thermal interfaces," J. of Electronic Packaging, 133(2), 2011.
- A. Snyder, D. Quach, J. R. Groza, T. S. Fisher, **S. L. Hodson**, and L. A. Stanciu, "Spark plasma sintering of ZrB_2-SiC-ZrC ultra-high temperature ceramics at 1800°C," Materials Sci. and Eng. A – Structural Mat. Prop. Microstrucure and Processing, 528(18), pp. 6079-6082, 2011.
- R. A. Sayer, **S. L. Hodson**, T. S. Fisher, "Improved efficiency of dye-sensitized solar cells using a vertically aligned carbon nanotube counter electrode," J. of Solar Energy Engineering, 132(2), 2010.

Book Chapters:

- X. Wang, B. A. Cola, T. L. Bougher, **S. L. Hodson**, T. S. Fisher, and X. Xu. Photoacoustic Technique for Thermal Conductivity and Thermal Interface Measurements. Chapter in *Annual Review of Heat Transfer*, Issue 16:135-157, 2013.

Conference Proceedings:

- 47th Power Sources Conference – Orlando, FL, 2016
  - *Paper and Presentation*: **S. L. Hodson**, E.S. Piekos, R. A. Sayer, S. A. Roberts, C. C. Roberts, "Thermal characterization of molten salt battery materials"
- HI TEMP Conference – Santa Fe, NM 2014
  - *Presentation*: **S. L. Hodson**, R. A. Sayer, and T. W. Grasser, "Thermal contact resistance measurements at elevated temperatures"
- ASME International Mechanical Engineering Congress and Exposition – San Diego, CA 2013
  - *Paper and Presentation:* **S. L. Hodson**, R. A. Sayer, T. P. Koehler, J. R. Serrano, S. M. Dalton, and T. S. Fisher, "Effect of gamma-ray irradiation on the thermal contact of carbon nanotube thermal interface materials"
- 10th International Energy Conversion Engineering Conference – Atlanta, GA 2012
  - *Paper and Presentation:* K. R. Saviers, **S. L. Hodson**, J. R. Salvador, L. S. Kasten, and T. S. Fisher, "Carbon nanotube arrays for enhanced thermal interfaces to thermoelectric devices"

- Symposium on Nanomaterials for Energy – West Lafayette, IN 2012
  - *Poster Display:* K. R. Saviers, R. Paul, **S. L. Hodson**, J. R. Salvador, and T. S. Fisher, "Enhanced thermal interfaces to thermoelectric elements for high temperature applications"
- Materials Research Society – San Francisco, CA 2011
  - *Poster Display:* **S. L. Hodson**, C. Rout, K.P.S.S. Hembram, and T. S. Fisher, "Chemical and plasma treatment of carbon nanotube interface materials for improved metal contact"
- ASME Pacific Rim Technical Conference and Exposition on Packaging and Integration of Electronic and 2011
  Photonics, MEMS, and NEMS - InterPACK – Portland, OR
  - *Paper and Presentation:* J. L. Wasniewski, D. H. Altman, **S. L. Hodson**, T. S. Fisher, A. Bulusu, S. Graham, and B. A. Cola, "Characterization of metallically bonded carbon nanotube-based thermal interface materials using a high accuracy 1D steady-state technique"
- ASME International Heat Transfer Conference – Washington, DC 2010
  - *Paper and Presentation:* P. T. McCarthy, **S. L. Hodson**, T. D. Sands, and T. S. Fisher, "Carbon nanotube interfaces for magneto thermoelectric actuation"
- ASME InterPACK Conference – San Francisco, CA 2009
  - *Paper and Presentation:* **S. L. Hodson**, T. Bhuvana, B. A. Cola, X. Xu, G. U. Kulkarni, and T. S. Fisher, "Palladium thiolate bonding of carbon nanotube thermal interfaces for high-temperature electronics" 2009
- ASME 3rd International Conference on Energy Sustainability – San Francisco, CA
  - *Paper and Presentation:* R. A. Sayer, **S. L. Hodson**, and T. S. Fisher, "Improved efficiency of dye sensitized solar cells using aligned carbon nanotubes"
- ASME Summer Heat Transfer Conference – Jacksonville, FL 2008
  - *Paper and Presentation:* B.A. Cola, **S. L. Hodson**, X. Xu, and T.S. Fisher, 2008, "Carbon nanotube array thermal interfaces enhanced with paraffin.